Title
Development and Characterization of Green Ultra-High Performance Fiber-Reinforced Concrete (G-UHP-FRC) for Structural and Non-Structural Applications

Author
Aghdasi, Parham

Publication Date
2019

Peer reviewed|Thesis/dissertation

Development and Characterization of Green Ultra-High Performance Fiber-Reinforced Concrete (G-UHP-FRC) for Structural and Non-Structural Applications

By

Parham Aghdasi

A dissertation submitted in partial satisfaction of the

requirements for the degree of

Doctor of Philosophy

in

Engineering – Civil and Environmental Engineering

in the

Graduate Division

of the

University of California, Berkeley

Committee in charge:

Professor Claudia P. Ostertag, Chair
Professor Paulo J. Monteiro
Professor Robert O. Ritchie

Spring 2019

Development and Characterization of Green Ultra-High Performance Fiber-Reinforced Concrete (G-UHP-FRC) for Structural and Non-structural Applications

by

Parham Aghdasi

Abstract

Development and Characterization of Green Ultra-High Performance Fiber-Reinforced Concrete (G-UHP-FRC) for Structural and Non-Structural Applications

by

Parham Aghdasi

Doctor of Philosophy in Engineering – Civil and Environmental Engineering

University of California, Berkeley

Professor Claudia P. Ostertag, Chair

This research first focused on developing a green ultra-high performance fiber-reinforced concrete (G-UHP-FRC) to reduce its cement content, and thus its carbon footprint and environmental impact. In this study, 50% of Portland cement by weight was replaced by 25% fly ash (FA) class F and 25% ground granulated blast-furnace slag (GGBFS). A comprehensive study was undertaken to achieve high workability while ensuring a minimum compressive strength of 125 MPa after 28 days of moist curing. The best performing G-UHP-FRC mixtures were selected for flexural as well as large-scale tensile testing. Ductility enhancement was achieved by optimizing a hybrid mechanism through combining three different types of micro and macro fibers.

Ideal lightweight structures, such as façade and flooring systems provide strength as well as thermal and acoustic insulation while keeping weight to a minimum. Highly porous concrete can be lightweight and have excellent insulating properties; however, increasing porosity, if geometrically disordered, results in rapid strength loss, with strength generally scaling as the cube of the solid volume fraction. Furthermore, recent advances in the development of Ultra-High Performance Fiber-Reinforced Concrete (UHP-FRC) with very high compressive strength (120 to 210 MPa) inspired the development of a lightweight structure by engineering the void spaces in the material, thus taking advantage of porous concrete's thermal insulating properties while maintaining strength and stiffness. This engineered material is here referred to as Octet-Truss Engineered Concrete (OTEC). To make OTEC structures, UHP-FRC and G-UHP-FRC mixtures were developed and used. 50.8-mm side-length OTEC unit cell specimens with various element diameters as well as 5×1×1-cell OTEC flexural specimens with 8 mm-diameter elements were cast and tested under uniaxial compression and four-point bending, respectively. The compressive strength of the OTEC unit cell specimens with various element diameters (8, 10, and 11 mm resulting in 66.4, 53.6, and 47.5% porosity, respectively) is mainly stretching-dominated, and hence considerably surpasses that of the control foam Green Ultra-High Performance Concrete (G-UHPC [no fibers]) specimens with random pore orientations (by about 180, 290, and 400%, respectively). Furthermore, the flexural performance of polylactic acid (PLA) octet-lattice reinforced Ultra-High Performance Concrete (UHPC) with three different UHPC volume fractions (37.5, 75, and 100%) was briefly investigated. All these results indicate a promising application of UHP-FRC and G-UHP-FRC OTECs as well as PLA octet-lattice reinforced UHPC for lightweight structures, such as façade, flooring, and membrane systems.

UHPC composites, with compressive strengths exceeding 125 MPa, carry tension to much higher levels compared to conventional concrete or High-Performance Fiber-Reinforced Cement-Based Composites (HP-FRCC). This improved strength of UHPC composites, however, leads to a brittle behavior under both tension and compression. Therefore, through addition of fibers in UHP-FRC composites, ductility and strain-hardening is achieved for such materials. During the last few years, however, while many researchers have focused on developing UHP-FRC composites with higher tensile strain values than 0.2–0.4% (strain value of steel rebar at its yielding point), the interaction and synergy between the composite and steel reinforcing bar to large deformations up to fracture remains unknown. In this research, eleven G-UHP-FRC as well as one Hybrid Fiber-Reinforced Concrete (HyFRC) dogbone-shaped specimens reinforced with a single deformed steel rebar in the middle were tested under uniaxial tension up to fracture of the steel reinforcing bar. After the yielding of the steel rebar, a dominant crack is formed at the location of which early strain-hardening and ultimately, fracture of the rebar can lead to an overall brittle failure at much lower strain values than the bare rebar for under-reinforced specimens. Therefore, a minimum longitudinal reinforcing ratio of ~4.0% (A706 Grade 60 mild steel) is recommended for UHP-FRC and G-UHP-FRC composites to ensure multiple macro cracking, uniform bar yielding throughout the specimen, and an overall ductile behavior. For all specimens, Digital Image Correlation (DIC) techniques were utilized based on which different crack formations were recorded, and concrete, rebar, and bond stresses were calculated. Such information then provides for the estimation of flexural strength of reinforced G-UHP-FRC components, which could be later verified through flexural experiments.

In memory of exemplary women in my life,

Bibijan Ghorbani-Aghdasi (بی بی جان قربانی),

Azam Aghdasi-Bagheri (اعظم اقدسی-باقری),

Sorayya Aghdasi-Amiri (ثریا اقدسی-امیری),

Rezvan Aghdasi-Ahmadi (رضوان اقدسی-احمدی)

Tuba Emadi-Rouhani (طوبا عمادی-روحانی), and

Tallie Dickerson

Table of Contents

List of Figures

List of Tables

Acknowledgements

"In the Name of God, the Most High! Lauded and glorified art Thou, Lord, God Omnipotent! Thou before Whose wisdom the wise falleth short and faileth, before Whose knowledge the learned confesseth his ignorance, before Whose might the strong waxeth weak, before Whose wealth the rich testifieth to his poverty, before Whose light the enlightened is lost in darkness, toward the shrine of Whose knowledge turneth the essence of all understanding and around the sanctuary of Whose presence circle the souls of all mankind.

How then can I sing and tell of Thine Essence, which the wisdom of the wise and the learning of the learned have failed to comprehend, inasmuch as no man can sing that which he understandeth not, nor recount that unto which he cannot attain, whilst Thou hast been from everlasting the Inaccessible, the Unsearchable. Powerless though I be to rise to the heavens of Thy glory and soar in the realms of Thy knowledge, I can but recount Thy tokens that tell of Thy glorious handiwork.

By Thy Glory! O Beloved of all hearts, Thou that alone canst still the pangs of yearning for Thee! Though all the dwellers of heaven and earth unite to glorify the least of Thy signs, wherein and whereby Thou hast revealed Thyself, yet would they fail, how much more to praise Thy holy Word, the creator of all Thy tokens.

All praise and glory be to Thee, Thou of Whom all things have testified that Thou art one and there is none other God but Thee, Who hast been from everlasting exalted above all peer or likeness and to everlasting shalt remain the same. All kings are but Thy servants and all beings, visible and invisible, as naught before Thee. There is none other God but Thee, the Gracious, the Powerful, the Most High."

–Bahá'u'lláh, the Founder of the Bahá'í Faith, 1817-1892

I am forever grateful to the Universal House of Justice, the Supreme Body of the Bahá'í Faith, whose unerring guidance has continuously illuminated and given shape, character, and purpose to my whole life.

I am very grateful to my doctoral advisor, Professor Claudia P. Ostertag, for giving me the opportunity to pursue my doctoral degree at the University of California, Berkeley, for believing in me, and for advising me throughout the last five years. I am also very grateful to my former advisor, Professor Shih-Ho (Simon) Chao, who advised and mentored me while pursuing my Masters' degree at the University of Texas at Arlington and has been a great supporter throughout the last eight years. I am also grateful to Professor Hayden K. Taylor for his advice and mentorship on a number of research projects throughout my studies at the University of California, Berkeley.

I am also very thankful to my dissertation committee members, Professor Paulo J. Monteiro and Professor Robert O. Ritchie for their insightful and constructive advice.

To my parents, Mr. Foroutan Aghdasi and Mrs. Parvin Ruhani; my brother, Mr. Payam Aghdasi; and my sister, Mrs. Parisa Aghdasi, who have trained, encouraged, supported, and reinforced me every step of the way, I can hear the lamentation of my words in attempting to adequately express my appreciation and admiration for your selfless and loving sacrifices. To my brother-in-law, Mr. Soleyman Aghdasi and my sister-in-law, Mrs. Sahba Mazidi, I am very thankful for your

encouragement and support. To my uncles Mr. Adib and Mahmoud Aghdasi and their families, I am also very grateful for their loving kindness during my stay in Tehran while attending the Bahá'í Institute for Higher Education (BIHE). To my dear friends Matthew Parks, Adib Haei Najafabadi, Houtan Rahmanian, and Amin Ghorbanpour and to my dear cousins, Shahin Bagheri and Faramarz Ghorbani, and also to Mrs. Charese Wagner and Mrs. Tallie Dickerson, I am very thankful for their love and support. I am also very grateful to the Bahá'ís of Arlington and nearby cities in Texas, for embracing me with love as their new family member during a very emotional period.

To my spiritual brothers and sisters Milly Farid, Kalan Rutstein, Shiva Tan, James Tan, Soroush Badie, Mayra Garcia, Bashir Parvane, Benjamin Blum, Tala Ram, Vida Amanat, Nedda Khorshidi, Lindsay Smith, Justin Smith, Yasamin Mohammadi, Seaon Shin, and Saman, Bijan, and Sheedvash Farid who have, through their deeds and actions, illustrated what true and selfless service to humanity means, I would like to thank you for your priceless friendship, love, and support. May the Blessed Beauty continue to shower upon you His confirmations and blessings.

To the junior youth and youth in Richmond and San Pablo, CA, you give me hope for a better tomorrow and true joy and long-lasting energy to keep learning, and for that, I am truly grateful. To the amazing UC Berkeley Bahá'í Club, you are the epitome of perseverance in the path of understanding and excellence. You provided me and many more with a safe space to find our true selves, to be real, to laugh and learn together, and to experience true friendship.

To Dr. Alexander Lin, Dr. Wilson Nguyen, Dr. Rotana Hay, Dr. Jacob Duncan, Dr. Ian Williams, and Mr. Brian Salazar, and all my other fellow colleagues at the University of California, Berkeley, I am very grateful for their advice, insightful conversations and discussions, and more importantly their friendship.

I would also like to gratefully acknowledge the assistance of the Department of Civil and Environmental Engineering laboratory staff in Davis Hall at the University of California, Berkeley, especially Phillip Wong, Cruz Carlos, Matt Cataleta, and Llyr Griffith for assisting in performing the experiments. Also, special thanks go to Dr. Clement Barthes for providing a free license for OpteCAL, the Digital Image Correlation software, and assisting in using this technique in the first few experiments.

Last but not least, I am forever appreciative of my professors and advisors at BIHE who went above and beyond, endured ineffable hardship, sacrificed so much, and even endured imprisonment to provide me and thousands more with the opportunity to pursue higher education while we were banned from seeking an advanced degree because of being Bahá'ís in our own home country, Iran that I love so dearly. May the light of Justice illumine the whole world.

To myself, as you can obviously attest, God and many people have really worked hard to get you here; do not screw it up!

This research is partially funded by the Republic of Singapore's National Research Foundation through a grant to the Berkeley Education Alliance for Research in Singapore (BEARS) for the Singapore-Berkeley Building Efficiency and Sustainability in the Tropics (SinBerBEST) Program. BEARS has been established by the University of California, Berkeley, as a center for intellectual excellence in research and education in Singapore. Some results and discussions included in Chapters 2, 3, and 4 of this manuscript have been published in [1,2]. The author is appreciative of

Prof. Claudia P. Ostertag for co-authorship in [1] and Dr. Ian D. Williams, Mr. Brian Salazar, Ms. Nicole Panditi, Prof. Hayden K. Taylor, and Prof. Claudia P. Ostertag for co-authorship in [2].

I would like to end this section with a quote by Bahá'u'lláh, the Founder of the Bahá'í Faith, Whose Writings, along with the Writings of His successors, 'Abdu'l-Bahá and Shoghi Effendi, have been a true source of solace, inspiration, and guidance throughout my life:

"Every age hath its own problem, and every soul its particular aspiration. The remedy the world needeth in its present-day afflictions can never be the same as that which a subsequent age may require. Be anxiously concerned with the needs of the age ye live in, and center your deliberations on its exigencies and requirements."

Chapter 1
Introduction

Low strength, reduced durability, and relatively short longevity as well as the brittle nature of conventional concrete have led to major concerns, especially throughout the last few decades since its widespread application as the number one construction material and as the second most used substance in the world after water. Therefore, great research interests have been generated in the development of cementitious concrete composites having ultra-high compressive strength, ductility, and durability, especially during the past two decades. Such composites were first recognized as reactive powder concrete (RPC) and more recently have been referred to as ultra-high performance concrete (UHPC) with no fibers and ultra-high performance fiber-reinforced concrete (UHP-FRC) including fibers. Early development schemes achieved ultra-high performance mainly through the application of special materials or specific treatments, such as vacuum mixing, high pressure, and high temperature techniques, all of which were used to increase the compressive strength of concrete.

For instance, In 1972, Yudenfreund et al. [3,4] achieved a compressive strength of 230 MPa by using fine ground cement and vacuum mixing to reduce the porosity of cementitious composites. A compressive strength of 510 MPa was, also in 1972, obtained [5] by using high pressures and temperatures. Later in 1994, a compressive strength of 236 MPa was achieved by De Larrard and Sedran [6] by using a low water-to-binder ratio of 0.14 and improving the packing density of the mixture. In 1995, Richard and Cheyrezy [7] through heat-treatment of concrete at temperatures between 20 to 90 ^{o}C, developed an RPC with compressive strengths of up to 170 and 230 MPa. By using 10% short steel fibers by volume of concrete (V_f), high temperatures of 250 to 400 ^{o}C, and high pressure of 50 MPa, they [7] also achieved compressive strengths of 490 to 680 MPa and 650 to 810 MPa by addition of quartz sand and steel aggregates, respectively, a remarkable achievement still unheard-of to this day.

It should, however, be mentioned that implementing special treatments, such as vacuum mixing, as well as high temperature and high pressure curing techniques and furthermore, using specific materials, such as steel aggregates, fine ground cement, and quartz sand, are not currently used in practice, especially for large-scale applications, due to the complexity and labor intensity of such processes. Therefore, a few attempts were later made to develop UHPC and UHP-FRC composites without using any special treatments or materials. It is well known that the strength of concrete is considerably affected by defects, such as air cavities in concrete. Even micron size empty spaces left between hydrated cement particles are considered defects that lower the strength of concrete.

In 2010, Naaman and Wille [8] suggested a method to improve the particle packing by optimizing the types and proportions of different constituent materials and a gradation of different particle sizes to fill the voids between larger particles, such as Sand 1 (median diameter of 460 μm) and cement (median diameter of 15 μm), by smaller particles, like Sand 2 (median diameter of 120 μm), silica fume (median diameter of 0.3–0.5 μm), and glass powder (99% crystalline silica sand with median diameter of 1.8 μm) to enhance the compressive strength. However, they [8] also confirmed that particle interlocking can hinder the ease of flow when particles are perfectly fitted together. Therefore, they [8] recommended that a Sand 2 with a slightly larger size than what is needed to perfectly fill the void between Sand 1 particles be chosen in order to create instability between the two sand particles to achieve better flowability without significantly compromising the strength. Shortly after in 2011, Wille et al. [9,10], for example, reported compressive strengths beyond 150 MPa for UHPC composites using cement, water, two types of sand, silica fume, glass powder (fine 99.3% crystalline silica sand), and high-range water reducer (HRWR or superplasticizer), following the recommendations in [8]. Later in 2016, Aghdasi et al. [11], took the suggestions in [8–10] and developed a highly flowable UHP-FRC composite for large-scale applications with compressive strengths ranging from 150 to 210 MPa. High flowability was achieved through an extensive study of replacing cement or sand (angular particles) by fly ash (spherical particles). Therefore, high flowability, ultra-high compressive strength, and high compressive and tensile ductility were achieved while no special curing or mixing techniques were used. The effects of various types of mix components, water-to-binder ratios, fiber volume fractions, and sand ratios were investigated to this end.

Same Sand 1 and Sand 2 types as in [11] were used in this research, following the suggestion in [8] where interlocking between particles were alleviated by intentionally creating instability between the two sand particles. However, because of the angular shape of the sand particles currently available in the U.S. market, creating such an instability did not prove to be sufficient to achieve the desirable flowability for large-scale casting. Therefore, fly ash (FA, with spherical particles) was introduced in UHP-FRC mixes in [11], and its effects on the liquefaction time, flow diameter, density, and compressive strength were extensively investigated. According to [11], a Sand 1: Sand 2 ratio of 0.63:0.37 is recommended according to uncompacted void content tests based on ASTM C1252-06 [12] and flowability and compressive strength tests according to ASTM C1437-07 [13] and ASTM C109/C109M-11a [14], respectively. They observed that by increasing the Sand 2 content, the liquefaction time increased, the flowability and density decreased while the compressive strength increased for mixes with no fibers and water-to-cementitious materials ratio (W/CM = Water[W]/(C[cement]+SF[silica fume]+FA[fly ash])) of 0.2. In this research, however, as mentioned later, a Sand 1:Sand 2 ratio of 0.7:0.3 was found to be more desirable to achieve a better flowability, which is still close to that of predicted by the model suggested in [8,15].

A C:SF:GP ratio of 1:0.25:0.25 recommended in [9] and confirmed in [11] was used, where C, SF, and GP stand for cement, silica fume, and glass powder, respectively. HRWR with a fixed amount of 1.1% of cement by weight recommended in [11] had to be increased to 2.0% in this research to achieve the required flowability. To this end, a few different polycarboxylate-based HRWRs were examined, and the most effective one, leading to the largest flow diameter, was chosen. Based on [11], short micro straight smooth-surfaced round steel fibers (d = 0.175 mm; L = 12.5 mm; Tensile Strength ≈ 2,200 MPa) up to 3.0% by volume of concrete were recommended to achieve sufficient flowability, avoidance of fiber clumping, ultra-high compressive strength more than 150 MPa, and

high ductility. In this research, however, fiber hybridization (a combination of up to four different types of fibers with a total amount of 2–3% by volume of concrete) was extensively investigated to achieve better crack resistance, strain-hardening, post-peak load-carrying capacity, and overall ductility and toughness. A maximum fiber factor of $X_f = 2.5$ ($X_f = V_f \times L_f/d_f$) recommended by Markovic [16] was considered, where V_f, L_f, and d_f stand for the volume fraction, length, and diameter of fibers, respectively.

According to [11], for mixes without fly ash replacement, a 0.192 to 0.208 W/CM was recommended. A W/CM ratio of 0.184 to 0.2 was further recommended while replacing 10–30% (by weight of cement) of Sand 1 by fly ash to obtain ultra-high strength and sufficient flowability for large-scale casting. Fly ash, which has spherical particles, provided an additional mechanism to enhance the ease of flow of the mixture by reducing the friction between the angular particles, such as sand and cement, and allowing them to move around more easily [17]. In addition, when Portland cement is partially replaced by fly ash, a higher volume of paste is achieved due to the lower density of fly ash compared to Portland cement. This enhances the cohesiveness and flowability of concrete [18]. The slower rate of hydration reaction of fly ash also reduces internal thermal cracking of concrete [19], which is especially critical in UHP-FRC with higher volumes of Portland cement, often twice as much as conventional concrete. Therefore, in this research Portland cement was also partially replaced by fly ash, and the W/CM ratio was accordingly adjusted. In [11], while partial replacement of Sand 1 by fly ash led to better flowability, higher compressive strengths were achieved when Portland cement was partially replaced by fly ash. In this research, it was decided to partially replace Portland cement by fly ash to reduce the embodied carbon footprint.

According to [20], slightly higher compressive strength values are recorded for smaller specimens compared to larger specimens, known as the size-effect. This is because the larger the specimen, the higher the possibility of containing more and larger defects or elements with low strength within the specimen. The compressive strength of UHP-FRC is often measured based on 50.8-mm cube specimens because of the limitations of the compression machines in most laboratories. In addition, the compound used for capping the ends of cylinder specimens is not strong enough for UHP-FRC cylinder to achieve a uniform stress distribution. In a few trial compression tests of UHP-FRC cylinders in this research, it was realized that the early failure of the capping compound leads to uneven stress distributions, stress concentrations, and premature failure of the samples. Graybeal and Davis [20] showed that a factor of 0.96 should be applied to the compressive strengths measured based on 50.8-mm cube specimens to obtain the equivalent compressive strength of a 101.6 mm-diameter cylinder. It should, however, be noted that this factor has not been applied to the compressive strength values reported in this research.

Aghdasi et al. [11] suggested using cement, two types of sand (with 460 and 120 μm median diameters, introduced as Sand 1 and Sand 2, respectively), fly ash class F, glass powder, silica fume, and superplasticizer. They also recommended using short micro straight smooth-surfaced round steel fibers ($d_f = 0.175$ mm; $L_f = 12.5$ mm; Tensile Strength ≈ 2,200 MPa) to reduce clumping during mixing and casting and for better flowability while using up to 3.0% fibers by volume of concrete. Aghdasi et al. [11] also investigated the mechanical properties of UHP-FRC based on larger-scale compression and tension material specimens to more realistically understand the behavior of UHP-FRC composites when used in structural members. Through these tests, an appreciable size-effect on the mechanical properties and behavior of UHP-FRC was further

noticed and emphasized in [11]. They [11] tested 70.6-mm cube UHP-FRC specimens, using a W/CM ratio of 0.184, 3% by volume of short micro steel fibers, and 10% replacement (by weight of cement) of Sand 1 by fly ash. This UHP-FRC mix achieved an average flow diameter of 180 mm and compressive strengths of 171.7, 202.7, and 208.2 MPa based on 50.8-mm cube specimens and 150.3, 191.7, and 191.7 MPa based on 70.6-mm cubes after 7, 28, and 56 days, respectively. They [11] also studied the effects of the number of fibers, using short micro (with a volume fraction of 3.0%) and short twisted steel fibers (with volume fractions of 3.0 and 5.0%; d_f = 0.5 mm; L_f = 14.0 mm), on the flowability, compressive strength, and ductility of UHP-FRC. This experiment was carried out to determine whether using a lesser amount of fibers could be compensated via the additional mechanical bond of twisted fibers. It was observed that as the number of fibers in UHP-FRC increases, the flow diameter decreases and the compressive strength as well as ductility under compression increases, and therefore, the number of fibers present in a sample, instead of the fiber volume fraction, directly affects such properties [11]. For example, the mixture with 3.0% volume fraction of short micro steel fibers (with about 253,715 fibers in a 70.6 mm cube specimen) achieved higher compressive strength and ductility (~6–8%) compared with the mixture with 5.0% volume fraction of short twisted steel fibers (with about 46,040 fibers in a 70.6 mm cube specimen). This was attributed to the fact that microcracks are quickly and more effectively controlled when more fibers are distributed in the mixture, leading to better redistribution of internal stresses and delaying localized cracks.

Aghdasi et al. [11] further studied the effects of UHP-FRC mixes (W/CM of 0.184, Sand 1: Sand 2 ratio of 0.7:0.3) with different percentages of fly ash while also changing the volume fraction of short micro straight steel fibers from 2.0 to 3.5% on the compressive strength based on 70.6-mm cube specimens. Based on their results [11], 3.0% fiber volume fraction and 20% replacement (by weight of cement) of Sand 1 by fly ash was found to lead to the highest compressive strengths of 166.8, 178.6, and 188.2 MPa after 7, 28, and 56 days, respectively. They [11] also measured the deformation of 70.6-mm cube specimens under compression after 28 days, for which the mixture with W/CM ratio of 0.184, 3.0% volume fraction of short micro steel fibers, and 10% replacement (by weight of cement) of Sand 1 by fly ash was used. Based on these results compressive stress-strain curves were plotted and reported. This UHP-FRC achieved very high compressive ductility with strain at peak compressive strength of 0.84 to 1.22% and maintained 90.5% and 61.7% of its maximum compressive stress at 1.5% and 3.0% of compressive strains, respectively [11]. While UHP-FRC developed so far does not use any special treatments or materials, it does use high volumes of Portland cement (about twice as much as conventional concrete). Using high volumes of Portland cement in UHP-FRC composites leads to high carbon dioxide emissions and possibly thermal cracking due to high heat of hydration. Therefore, in this research a highly flowable green UHP-FRC (G-UHP-FRC) with a minimum compressive strength of 125 MPa after 28 days of moist curing was developed. In G-UHP-FRC mixes, 50% of Portland cement is replaced by 25% fly ash class F and 25% ground granulated blast-furnace slag (GGBFS) to reduce its environmental impact.

When UHP-FRC is tested under tension, cracks initiate when the applied stress reaches the tensile strength of the matrix. These cracks are then immediately bridged and controlled by the existing fibers at the location of the cracks. If there are sufficient fibers in the matrix, the tension specimen will be able to take higher tensile forces after first-cracking, followed by multiple cracking, up to its peak tensile strength. This phenomenon, usually known as strain-hardening, is reportedly recorded for UHP-FRC composites by different researchers. However, the tensile properties of

UHP-FRC, including its tensile strength and ductility, are mainly reported based on small-scale specimens. A tensile strength of 20 MPa corresponding to a strain at peak tensile strength of 0.6% was reported by Wille et al. [21] based on tension specimens with a cross sectional area of 1,290 mm^2 made of UHP-FRC with 3.0% volume fraction of straight steel fibers. Using 2.0% volume fraction of ultra-high-molecular-weight polyethylene fibers, tensile strength and strain at peak tensile stress of 14.5 MPa and 3.4%, respectively, were reported by Ranade et al. [22] based on tension specimens with a cross sectional area of 381 mm^2. Aghdasi et al. [11] were among the first to examine the tensile properties of UHP-FRC according to larger-scale tension specimens with a cross sectional area of 10,323 mm^2, 8 and 27 times larger than those tested by Wille et al. [21] and Ranade et al. [22], respectively. They [11] also tested UHP-FRC tension specimens with smaller cross sectional area of 1,290 mm^2 for comparison purposes. Based on these results, 30 to 60% increase in tensile strength and more than 40% increase in tensile ductility (based on strain at peak tensile stress) were reported for smaller-scale compared to larger-scale tension specimens [11], using 3.0% volume fraction of short micro straight steel fibers. Therefore, tensile properties of UHP-FRC based on small-scale specimens should be carefully interpreted concerning design applications in structural members. Some researchers, including Kwon et al. [23] and Park et al. [24], investigated the effects of fiber hybridization and were able to improve the tensile properties of UHP-FRC by combining different types of micro and macro fibers. In this research, the effects of fiber hybridization were investigated first based on G-UHP-FRC flexural tests, and later, the tensile performance of larger-scale G-UHP-FRC tension specimens (with cross sectional area of 10,323 mm^2) with a hybrid combination of different types of fibers (with a total fiber volume fraction of 2.5%) was investigated.

To the best of the author's knowledge, large-scale casting of nonproprietary UHP-FRC composites in America has, very rarely if at all, been reported so far. One exception is the experiment by Aghdasi et al. [11], where 0.62 cubic meter of UHP-FRC was produced and cast in the plastic hinge region of a full-scale moment frame column with congested steel reinforcement. This moment frame was later tested under strong cyclic earthquake forces [25]. Large-scale casting of UHP-FRC could be very challenging due to its high viscosity and often very low W/CM ratios. Though often not reported by researchers in this field, even mixing, pouring, placement, and compacting small batches of UHP-FRC composites in the laboratory are quite challenging if the UHP-FRC composite is not well-designed to have sufficient flowability. Aghdasi et al. [11] were able to achieve sufficient flowability (flow diameter more than 200 mm according to ASTM C1437-07 [13]) by introducing 10–30% fly ash (by weight of cement) into the mixture, due to its spherical particles, that made the large-scale casting possible without any internal or external vibrations. For their large-scale casting experiment [11], a high shear mixer was manufactured by a local company in Texas, which was able to effectively mix UHP-FRC with a low W/CM ratio of 0.2, 3.0% volume fraction of short micro straight steel fibers, produced by the same local company, and 10% replacement (by weight of cement) of Sand 1 by fly ash. High flowability (flow diameter of 203 mm based on [13]), ultra-high compressive strengths of 172.4 and 195.1 MPa after 28 days and 6 months, respectively, very high compressive strain of 1.22% at peak compressive strength based on 70.6-mm cube specimens, average tensile strength of 7.7 MPa, and strain at peak tensile strength of 0.15% based on large-scale dogbone-shaped tension specimens (101.6 mm × 101.6 mm × 177.8 mm) were recorded for the UHP-FRC produced during their large-scale casting experiment [11]. A high surface temperature of 64 ^oC was measured one day after casting on the UHP-FRC column, which infers even higher temperatures inside the column [11]. Although no major visible issues (no thermal cracking) were observed due to such high temperatures, probably

because of fiber-reinforcement, high heat of hydration could be detrimental when UHP-FRC is used for mass construction [11]. Therefore, in this research, 50% of Portland cement was replaced by industrial by products to reduce its heat of hydration and in addition, to improve upon its flowability in regard to large-scale applications.

Superior mechanical properties of UHPC and UHP-FRC composites as summarized so far, can potentially lead to a variety of both non-structural and structural applications. For example, very high compressive strength of UHP-FRC composites (120–210 MPa), as described later, inspired the development and design of lightweight concrete metamaterials in this research, mainly for non-structural applications, such as in building façade and flooring systems. This was accomplished by engineering the void structure in the material to reduce density while maintaining strength and stiffness, using lattice structures. Furthermore, UHPC and UHP-FRC composites can potentially be used for structural applications, such as in foundations, moment frame girders, columns, and joints. However, wide-spread adoption of such composites for structural applications in practice has not yet been made possible, mainly due to our limited knowledge of the synergy between such composites and steel reinforcement. Therefore, in this research, multiple large-scale dogbone-shaped G-UHP-FRC tension specimens reinforced with different types and reinforcing ratios of steel rebars were tested to more comprehensively investigate the performance of reinforced G-UHP-FRC under tension and to provide design recommendations for structural application of UHP-FRC and G-UHP-FRC composites.

Lattices are used in nature to great effect. With structures tailored to suit the material, excellent mechanical properties are achieved using a minimal amount of material. Advancements in additive manufacturing in recent years have enabled the creation of three dimensional lattices optimized for the base material. This yields excellent mechanical and thermal properties, and simultaneously reduces the amount of material used [26]. An ideal lattice for concrete is one that places the material primarily under compression, thus minimizing the influence of concrete's poor tensile strength. One such cell structure that is shown to have this characteristic is the octet-truss lattice. Previous studies have shown that the octet lattice approaches linear relation between strength and density for metal and polymer base materials [27]. Concrete is the most prolific building material in the world today due to its versatility and widespread availability, yet it is far from an ideal material; it is heavy, weak in tension, and a poor insulator. Beyond the material properties, concrete has a significant environmental impact due to its high carbon footprint and demand for raw materials. As human population increases, and more people trend toward living in urban areas, the need for fully optimized materials and structures becomes increasingly important to improve the performance of buildings and reduce their environmental impact. Octet-truss lattices seem to be ideal for concrete as well, especially if the concrete exhibits ultra-high compressive strength.

Highly porous concrete can be lightweight; however, increasing porosity, if geometrically disordered, results in rapid strength loss, with strength generally scaling as the cube of the solid volume fraction. In this research, Octet-Truss Engineered Concrete (OTEC) was invented using UHP-FRC and G-UHP-FRC mixtures. The G-UHP-FRC mixture substitutes up to 50% of the cement content with industrial byproducts. 50.8-mm OTEC unit cells with different element diameter sizes (8, 10, and 11 mm resulting in 66.4, 53.6, and 47.5% porosity, respectively) were fabricated and tested under uniaxial compression. These OTEC structures, being mainly stretching-dominated, were able to significantly exceed the compressive strength of the bending-dominated control foam Green Ultra-High Performance Concrete specimens (45.3% porosity). In

addition, the performance of 5×1×1-cell OTEC flexural specimens with 8 mm-diameter elements are also presented. These flexural specimens consisted of two solid top and bottom flanges, each with a thickness of 8 mm extending the full length of the samples, connected to each other with five interconnected OTEC cells. The design of these flexural specimens was intended to better represent the application of OTECs in building systems, such as façade and flooring systems. In addition, a set of similar flexural specimens with double skins (two, top and bottom, flanges), but this time, reinforced and connected with 3D-printed polylactic acid (PLA) octet lattices were also fabricated for comparison purposes with OTECs and as another alternative for design of façade and flooring systems. The results mark the emergence of promising concrete metamaterials that could be used for lightweight structures, such as in building façade and flooring systems.

Although many researchers have, more specifically during the last few years, developed UHP-FRC composites with very high strain capacity under tension, however, the advantages of such cementitious composites in the presence of steel reinforcement remains unclear. Chao et al. [28] showed that the cracking distribution and tensile ductility of fiber-reinforced concrete (FRC) are enhanced due to the presence of reinforcing bars or prestressing strands. Aghdasi et al. [11] tested a 101.6 mm × 101.6 mm × 177.8 mm dogbone-shaped UHP-FRC tension specimen reinforced with a single deformed No. 3 A706 Grade 60 mild steel rebar (reinforcing ratio of 0.69%) to investigate the effect of tension-stiffening and the tensile properties of UHP-FRC when reinforced with reinforcing bars. For this tensile testing, a UHP-FRC mixture with a W/CM ratio of 0.184, 10% replacement (by weight of cement) of Sand 1 by fly ash, and 3.0% volume fraction of short micro straight steel fibers were used. A tensile strength and corresponding strain value of 8.3 MPa and 0.17%, respectively, was earlier reported for this mix design. The load carried by the rebar was calculated based on the strain values measured by three strain gauges installed on the rebar along the gauge length and then subtracted from the total load to obtain the net tensile force carried by UHP-FRC and thus its net stress-strain curve [11]. According to the results of this test [11], the presence of rebar significantly improved the tensile ductility (measured by tensile strain at peak tensile strength) of UHP-FRC, from 0.17% (with no rebar) to 1.30% (more than seven times) while the peak tensile stress, 7.7 MPa, did not change much compared to the tensile strength of 8.3 MPa for the tension specimen with no rebar.

This tension specimen [11] was tested all the way to the fracture of the steel rebar, which occurred at a strain value of 5.8%, about three times less than that of the bare steel rebar. This early fracture of rebar in high-performance fiber-reinforced concrete composites (HP-FRCC) and UHP-FRC has also been reported by other researchers. Moreno et al. [29] reported average tensile strains of 3.5%, 7.4%, and 6.8% at fracture of steel reinforcing bars for Engineered Cementitious Composite (ECC), Hybrid Fiber-Reinforced Concrete (HyFRC), and Self-Consolidating HyFRC (SC-HyFRC), respectively, compared to that of 10.3% for conventional reinforced concrete (with no fibers) with the same 1.2% steel rebar longitudinal reinforcing ratio. Kang et al. [30] also reported low ultimate strain values of 2.6% and 3.5% for ECC with longitudinal steel reinforcement ratios of 1.64% and 1.40%, respectively, which were attributed to localized cracks and prevention of longitudinal splitting crack formations due to superior confinement of ECC compared to conventional concrete. Using a 0.92% longitudinal steel reinforcement ratio, Hollmann [31] reported ultimate strain values of 0.4–2.6% and 1.4–4.7% for UHP-FRC composites reinforced with A1035 and A615 steel rebars, respectively, and observed that specimens with lower fiber volume fractions lead to higher ultimate strain values due to easier formation of multiple macro cracks. Jungwirth and Muttoni [32] also tested UHP-FRC tension specimens reinforced with 1.0%,

2.5%, and 4.5% longitudinal steel reinforcing ratios, using four rebars. Although they [32] did not report the ultimate strain values, a similar behavior as observed by other researchers (early fracture of rebars due to localization) is inferred based on their stress-strain graphs. Redaelli [33] tested UHP-FRC tension specimens with 3.14% and 6.28% longitudinal reinforcing ratios, using 4 or 8 No. 5 (16 mm in diameter) steel rebars. According to load-elongation graphs reported in [33], ultimate strain values less than 2.0% were measured for all tension specimens due to early strain localization, which lead to an overall brittle behavior. It was further concluded that this behavior remains the same regardless of the type and reinforcement ratio of steel rebars [33] used in their experiments. As mentioned earlier, this research, engages in a more comprehensive study of the performance of reinforced G-UHP-FRC under tension in order to better understand the mechanics of the problem and to further make design recommendations for application of UHP-FRC and G-UHP-FRC composites in structural elements.

This manuscript is organized in five chapters. The first chapter gives an historical overview of the methods and techniques used by different researcher throughout the last two decades in development of UHPC and UHP-FRC composites and their potential applications in structures and buildings. The second chapter focuses on the development of G-UHP-FRC to reduce the volume of Portland cement in such composites for sustainability purposes while achieving ultra-high compressive and tensile strength and ductility. The third chapter explores the design of an Octet-Truss Engineered Concrete (OTEC) mainly for non-structural applications, such as in building façade and flooring systems, with the purpose of reducing weights by engineering the void structure in the material, using lattice structures. The forth chapter investigates the effect of steel reinforcement on the tension-stiffening behavior of G-UHP-FRC with the purpose of better understanding the composite behavior of G-UHP-FRC and steel reinforcing rebar when used in structural elements. Lastly, the fifth chapter summarizes the results of this research and ends this manuscript with a few remarks and suggestions in regard to future research in the field.

Chapter 2

Development of Green Ultra-High Performance Fiber-Reinforced Concrete (G-UHP-FRC)

2.1 Introduction

Major advances in the development of Ultra-High Performance Fiber-Reinforced Concrete (UHP-FRC) with compressive strength exceeding 120 MPa and high ductility has set in motion widespread and ever-increasing application of UHP-FRC in the field of civil engineering [11,34–36], especially during the last few years. While the current state-of-the-art [11,37,38] does not use any special materials or treatments to achieve ultra-high strength, the UHP-FRC mixtures, however, use high Portland cement contents (about twice as much as is normally used in conventional concrete). Using high volumes of Portland cement in UHP-FRC composites leads to high heat of hydration [11] as well as high carbon dioxide emissions, both of which are of major concern. Therefore, employing development approaches and techniques that use less Portland cement in UHP-FRC mixtures is absolutely essential and is the focus of this chapter.

The first part of this chapter focuses on developing a green UHP-FRC (G-UHP-FRC) of high workability while ensuring a minimum compressive strength of 125 MPa after 28 days of moist curing. All the constituent materials, except for some of the fibers, are commercially available in the United States. In the G-UHP-FRC mixtures, Portland cement is being partially replaced by industrial by-products such as fly ash (FA) class F and ground granulated blast-furnace slag (GGBFS). A combination of different types and amounts of fibers (a total amount of 2 to 3% by volume of concrete) is investigated for optimum crack resistance and overall ductility, first through four-point flexural tests and later through direct uniaxial tension tests. Tensile properties of G-UHP-FRC are measured, using large-scale (101.6 mm×101.6 mm×355.6 mm) dog-bone shaped tension specimens, to obtain a more realistic tensile response of G-UHP-FRC.

2.2 Materials and methods

2.2.1 Materials

UHP-FRC and G-UHP-FRC were developed in this research, using similar procedures in [1,11,37,38]. A summary of the materials characteristics is provided in Table 1, and material

particle gradations and median particle sizes as well as the fibers used in this research are illustrated in Figure 1a and Figure 1b, respectively. All the materials (except for some of the fibers) used in this research are currently available in the U.S. market.

Table 1 - Materials used in the experimental program.

Coarse Aggregate (CA)	Madison Pea Gravel	9.5 mm
Fine Aggregate (FA)	Vulcan sand	-
Silica Sand 1 (S1)	460 Mesh	460 μm*
Silica Sand 2 (S2)	120 Mesh	120 μm*
	90 Mesh	90 μm*
	80 Mesh	80 μm*
Fibers	SF-1 Hooked-End Steel	D = 0.75 mm L = 60 mm Tensile Strength ≈ 1,050 MPa
	SF-2 Hooked-End Steel	D = 0.55 mm L = 30 mm Tensile Strength ≈ 1,100 MPa
	SF-3 Short Micro Steel	D = 0.15 mm L = 12 mm Tensile Strength ≈ 2,200 MPa
	SF-4 Long Micro Steel	D = 0.15 mm L = 19 mm Tensile Strength ≈ 2,200 MPa
	SF-5 Hooked-End Steel	D = 0.55 mm L = 30 mm Tensile Strength ≈ 3,070 MPa
	SF-6 Short Micro Steel	D = 0.20 mm L = 13 mm Tensile Strength ≈ 1,965 MPa
	PVA†	D = 0.04 mm L = 8 mm Tensile Strength ≈ 1,600 MPa
Cement (C)	Type II/V	15 μm*
	White Cement	15 μm*
Fly ash (FA)	Class F	10 μm*
GGBFS‡	-	15 μm*
Glass Powder (GP)	White Silica	1.8 μm*
Silica Fume (SF)	Black Undensified	0.3 μm*
	White Undensified	0.5 μm*
HRWR′	Polycarboxylate-based	-

* Median particle size
† Polyvinyl alcohol
‡ Ground Granulated Blast Furnace Slag
′ High-range water reducer

To enhance the sustainability of UHP-FRC, 50% of Portland cement was replaced by FA and GGBFS in G-UHP-FRC mixtures. Flowability of the mixtures was examined according to ASTM C1437-07 [13], which is different from the standard test method for slump flow. All specimens were cured in the fog room (with more than 95% relative humidity at room temperature) until a day before testing.

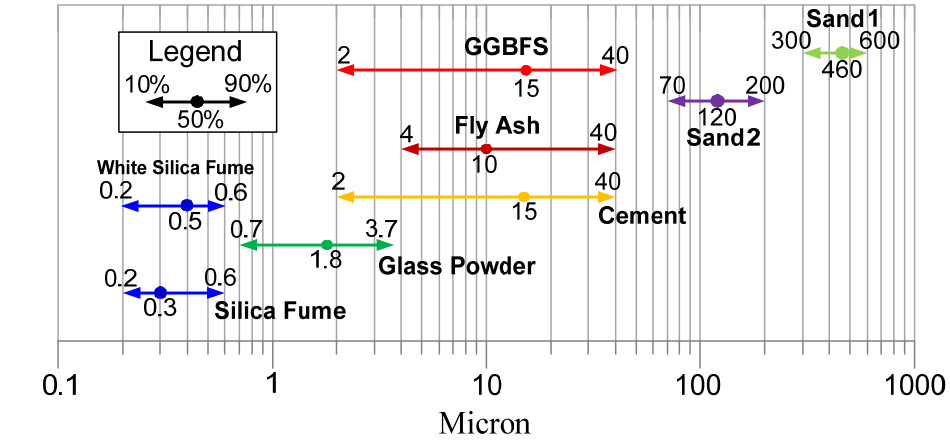

(a)

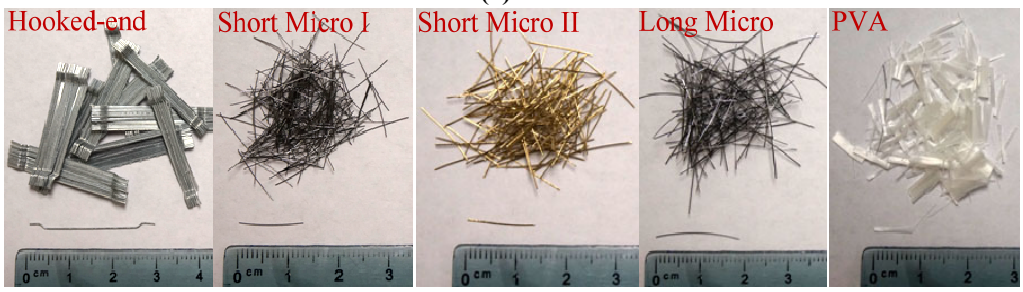

(b)

Figure 1 - (a) Particle gradation and median diameter of the materials and (b) different types of fibers used for development of G-UHP-FRC.

2.2.2 Mechanical properties measurements

The compressive strengths of the various mixtures were determined by testing 50.8-mm solid cubes in accordance with ASTM C109/109M-11a [14]. Flexural properties of the mixtures were investigated by subjecting 76.2 mm×76.2 mm×279.4 mm prisms to four-point bending according to ASTM C78 [39].

Large-scale tension specimens with a cross section of 101.6 mm×101.6 mm and a gauge length of 355.6 mm were utilized to allow for the formation of multiple cracks as a result of a better stress distribution. These specimens were tested under uniaxial tension using a hydraulic displacement-controlled machine with a constant displacement rate of 0.508 mm/min. The tension test setup and relevant dimensions are shown in Figure 2.

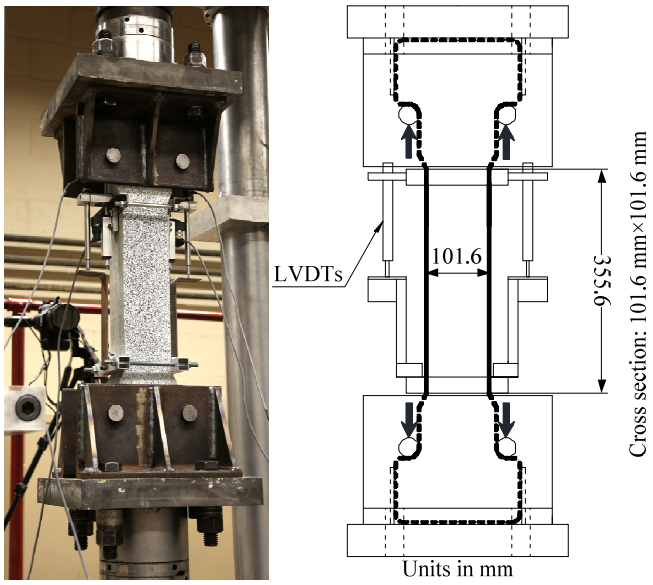

Figure 2 - (a) Actual and (b) schematic design of the tension test setup.

Longer dogbone-shaped tension specimens with cross section of 101.6 mm×101.6 mm and a gauge length of 355.6 mm (twice as long as prior research [11]) were considered for the tension experiments in this research in order to achieve a more realistic tensile behavior of G-UHP-FRC.

2.2.3 Development of Green Ultra-High Performance Fiber-Reinforced Concrete (G-UHP-FRC)

In prior research [11] during a large-scale cast-in-place experiment, 0.62 cubic meter of UHP-FRC was used in the plastic hinge region of a full-scale moment frame column. A high temperature of 64^{o}C was measured on the surface of the full-scale UHP-FRC column, indicating even much higher internal temperatures due to high volumes of Portland cement required to produce UHP-FRC. Although no early-age cracking due to this thermal gradient was observed, it is imperative to reduce its heat of hydration as well as its carbon footprint particularly when UHP-FRC is used for special large-scale applications. High volumes of cement can also lead to autogenous shrinkage [40]. Therefore, this research first focused on the possibility of achieving a more sustainable UHP-FRC by partially replacing cement with FA and GGBFS without compromising its fresh and later-age hardened properties.

G-UHP-FRC is referred to in this document as mixtures where 50% of Portland cement is replaced by 25% FA and 25% GGBFS. The water-to-cementitious materials ratio (W/CM = Water[W]/(C+FA+GGBFS+SF)) 0.184 to 0.2 recommended in [11] to obtain ultra-high strength along with sufficient flowability had to be initially increased to 0.25 since the high-range water reducer (HRWR) used in prior research with the same effectiveness was no longer available for purchase. A fixed HRWR corresponding to 2% of cementitious materials (C+FA+GGBFS) by weight was utilized for all experiments while flowability was enhanced by other means.

A Sand 1:Sand 2 ratio of 0.7:0.3 proved to result in better flowability in G-UHP-FRC without compromising strength compared to that of 0.63:0.37 suggested in prior research [11]. Furthermore, Sand 2 with a median particle size of 120 μm, also recommended in [11], was used since it resulted in higher flowability and compressive strength compared to that of 80 μm. In these

G-UHP-FRC mixtures the (Cement [C]+FA+GGBFS):Silica Fume (SF):Glass Powder (GP) ratio was kept at 1:0.25:0.25, similar to the C:SF:GP ratio for mixtures with 100% cement, according to [9,11]. The particle size gradation was investigated before by Naaman and Wille [8] in order to increase the flowability of the mixture by creating instability between sand particles to avoid particle interlocking in the mixing and casting phase. Sand 1 and Sand 2 with median particle sizes of 460 μm and 120 μm, respectively, used in this research, are hence in accordance with [8]. Aghdasi et al. [11] found, however, that the recommended particle size gradation [8] could not effectively increase the flowability; therefore, in prior research [11], 10–30% FA, which consists of spherical particles, was introduced as a supplemental cementitious/pozzolanic material, replacing Sand 1, to reduce the interfriction between particles and thus further improve the flowability of the mixture. In this research, FA was utilized for a twofold purpose, namely improved sustainability through cement replacement and enhanced flowability.

The preliminary material development phase included achieving a G-UHP-FRC mixture with high flowability and compressive strength greater than 125 MPa while up to 50% of cement is replaced by industrial byproducts. To achieve these goals various methods were used to first increase flowability, which then allowed to achieve higher compressive strengths at lower W/CM ratios. To this end, some mixtures use white Portland cement instead of ordinary Portland cement for better flowability. In addition, black undensified silica fume (median particle size of 0.3 μm) was replaced by white undensified silica fume of lower carbon content (median particle size of 0.5 μm). It was observed that a slightly larger median particle size of white silica fume, resulting in a smaller surface area, allowed for a reduction in water demand. Selected mix weight ratios used in this research are summarized in Table 2. The results regarding fresh and harden properties are presented in Section 2.3.1.

Table 2 - Primary mixture weight ratios.

Mix #	C	FA	GGBFS	S1*	S2	SF	W/CM Ratio	HRWR	GP	Fiber, V_f (%)
Trial	1.0	0.2	0.0	0.5	0.3†	0.25	0.25	0.015	0.25	3.0¶
	1.0	0.1	0.0	0.6	0.3£	0.25	0.25	0.02	0.25	3.0‡
	1.0	0.1	0.0	0.6	0.3″	0.25	0.25	0.02	0.25	3.0¶
	1.0′	0.2	0.0	0.5	0.3″	0.25‴	0.20	0.02	0.25	2.5‡
	0.8	0.2	0.0	0.7	0.3†	0.25	0.25	0.015	0.25	3.0¶
	0.7	0.3	0.0	0.7	0.3†	0.25	0.25	0.025	0.25	3.0¶
1	0.7	0.3	0.0	0.7	0.3†	0.25	0.22	0.03	0.25	3.0‡
2	0.7	0.3	0.0	0.7	0.3†	0.25	0.25	0.02	0.25	3.0‡
3	0.5	0.25	0.25	0.7	0.3″	0.25	0.25	0.02	0.25	2.5‡
4	0.5	0.25	0.25	0.7	0.3″	0.25	0.24	0.02	0.25	2.5‡
5	0.5	0.25	0.25	0.7	0.3″	0.25‴	0.25	0.02	0.25	2.5‡
6	0.5	0.25	0.25	0.7	0.3″	0.25‴	0.24	0.02	0.25	2.5‡
7	0.5	0.25	0.25	0.7	0.3″	0.25‴	0.22	0.02	0.25	2.5‡
8	0.5′	0.25	0.25	0.7	0.3″	0.25‴	0.22	0.02	0.25	2.5‡
9	0.5′	0.25	0.25	0.7	0.3″	0.25‴	0.20	0.02	0.25	2.5‡
10	0.5′	0.25	0.25	0.7	0.3″	0.25‴	0.184	0.02	0.25	2.5‡
11	0.5′	0.25	0.25	0.7	0.3″	0.25‴	0.176	0.02	0.00	2.5‡
12	0.5′	0.15	0.35	0.7	0.3″	0.25‴	0.20	0.02	0.25	2.5‡
13	0.5′	0.25	0.25	0.7	0.3″	0.25‴	0.20	0.02	0.25	3.0╪
14	0.5′	0.25	0.25	0.7	0.3″	0.25‴	0.20	0.02	0.25	3.0‖
15	0.5′	0.25	0.25	0.7	0.3″	0.25‴	0.20	0.02	0.25	0.0
16£	0.5′	0.25	0.25	0.7	0.3″	0.25‴	0.22	0.02	0.25	varies╫
17§	0.5	0.25	0.25	0.7	0.3″	0.25‴	0.25	0.02	0.25	varies╫
18	0.5	0.25	0.25	0.7	0.3″	0.25‴	0.23	0.02	0.25	varies╫
19	0.5	0.25	0.25	0.7	0.3″	0.25‴	0.22	0.02	0.25	varies╫

* Median particle size of 460 μm
† Median particle size of 80 μm
£ Median particle size of 90 μm
¶ SF-6 Short micro steel fibers, % by volume of concrete
‡ SF-3 Short micro steel fibers, % by volume of concrete
′ White Portland cement
″ Median particle size of 120 μm
‴ White undensified silica fume
╪ 1.5% SF-5 hooked-end; 0.75% SF-4 long micro; and 0.75% SF-3 short micro steel fibers by volume of concrete
‖ 2.0% SF-5 hooked-end and 1.0% SF-3 short micro steel fibers by volume of concrete
╫ For details, refer to Section 2.3.2, Table 4
£ Same as mix #8 except for the types and volume fraction of fibers
§ Same as mix #5 except for the types and volume fraction of fibers

2.2.4 Effect of fibers and fiber hybridization on flexural and tensile performance of G-UHP-FRC

The effect of various fibers and fiber hybridization on the ductility of G-UHP-FRC was investigated through four-point bending tests. Fiber hybridization, achieved by combining macro (hooked-end steel) and micro fibers, has been shown to enhance the performance of fiber reinforced composites [41] by controlling the cracks on multiple scales from the micro to the macro scale. Therefore, nine batches and a total of 18 prisms (2 prisms from each batch) were made with 4 types of fibers (SF-5 hooked-end steel, SF-3 short micro steel, SF-4 long micro steel, and PVA fibers) as shown in Figure 1. In all these samples 50% of cement was replaced by 25% FA and 25% GGBFS. The first six batches were mixed using white Portland cement while the last three,

were made with ordinary Portland cement. Mixes #16 to #19 (Table 2) were used for these experiments. The results will be discussed in Section 2.3.2.

2.2.5 Tensile testing of large-scale G-UHP-FRC without embedded rebar

The performance of larger size UHP-FRC specimens in tension is of special interest and import if such materials are intended to be used in large-scale structural applications. Therefore, two large-scale G-UHP-FRC tension specimens were made using mixes #18 and #19 (Table 2). The mixture contains 1.5% 30 mm SF-5 hooked-end steel macro fibers, 0.5% SF-4 long steel micro fibers, and 0.5% SF-3 short steel micro fibers. The two tension specimens slightly differed in regard to their W/CM ratio (0.22 versus 0.23). For comparison purposes, a Hybrid Fiber-Reinforced Concrete (HyFRC; 0.8% 60 mm SF-1 hooked-end steel fibers, 0.5% 30 mm SF-2 hooked-end steel fibers, and 0.2% PVA fibers; W/CM = 0.54) tension specimen was also cast and tested under uniaxial tension. HyFRC composites exhibit multiple cracking and strain-hardening after first cracking, which are achieved mainly by using a hybrid combination of both PVA microfibers and steel macrofibers with different lengths and aspect ratios to control cracking at microscale and macroscale, respectively. Details on the development and mechanical properties of HyFRC are provided in [41].

2.3 Results and discussion

2.3.1 Flowability and uniaxial compression tests

As mentioned earlier, the main objective of the G-UHP-FRC development phase was to achieve high flowability and compressive strength greater than 125 MPa after 28 days while up to 50% of Portland cement being replaced by industrial byproducts. Flowability and compression test results are all summarized in Table 3. First, a few trial mixes were performed based on recommendations suggested in [11], replacing Sand 1 by 10 to 20% of FA as well as cement by 20% FA. As summarized in Table 3, ultra-high compressive strength in excess of 138 MPa was achieved for these mixes after 28 days. Three types of Sand 2 with three different median particle sizes (80, 90, and 120 μm) were used to investigate which one is more effective in leading to a denser micro structure and better flowability. Sand 2 with a median particle size of 120 μm was observed to result in a higher compressive strength and flowability as also recommended and confirmed by Aghdasi et al. [11]. It was further observed that a higher FA content (20% versus 10%) leads to higher flowability, as expected, without compromising the compressive strength. Also, using white Portland cement and white silica fume made it possible to reduce the W/CM ratio from 0.25 to 0.20 while flowability (245 mm) was increased considerably and compressive strengths of 144.8 MPa and 153.1 MPa were achieved after 28 and 56 days, respectively.

In addition, it was observed that although replacement of cement by FA compared to that of Sand 1 by FA results in a slightly lower flowability, a higher compressive strength (156.5 MPa) is achieved for the mix with 30% replacement of cement by FA at 56-day, which is about 19% higher than its compressive strength at 28-day. This enhancement in compressive strength is believed to be due to the pozzolanic reaction of FA, which was later further investigated. It was further noticed that a flow diameter in excess of 200 mm seems to be necessary to achieve ultra-high strength, as also indicated in [11]. The lower the flowability, the more difficult it becomes for the entrapped

air bubbles to be evacuated from the matrix, thus creating more air voids in concrete and as a consequence, resulting in lower strength.

Table 3 - Flowability and compression test results.

Mix #	Flow Diameter (mm)	Bulk Density, kg/m^3	Compressive Strength*, MPa		
			7-day	28-day	56-day
Trial	226	2,385	101.4	142.7	139.3
	191	2,424	103.4	137.9	135.1
	186	2,473	115.1	155.8	171.7
	245	2,465	118.6	144.8	153.1
	197	2,408	102.7	141.3	144.1
	210	2,404	100.0	131.7	156.5
1	132	2,409	82.0	111.0	126.2
2	191	2,393	92.4	123.4	140.0
3	222	2,424	95.1	134.4	150.3
4	197	2,406	95.1	132.4	148.2
5	**> 254**	**2,427**	**90.3**	**131.0**	**147.5**
6	> 254	2,428	89.6	128.9	144.8
7	210	2,441	91.7	128.9	140.7
8	**> 254**	**2,432**	**99.3**	**133.8**	**146.9**
9	232	2,467	105.5	133.1	141.3
10	198	2,518	104.8	134.4	143.4
11	226	2,478	105.5	117.9	138.6
12	221	2,500	107.6	133.8	137.2
13	208	2,521	98.6	126.9	141.3
14	214	2,504	94.4	124.1	126.9
15	> 254	2,297	97.2	107.6	127.6

* Average compressive strength based on two 50.8-mm solid cube specimens

Mixes #1 and #2 were performed, replacing 30% of cement with FA and using W/CM ratios of 0.22 and 0.25 and HRWR contents of 3% and 2% by weight of cementitious materials (C+FA), respectively. By comparing mix #1 with mix #2, it is observed that in an attempt to increase the compressive strength, if W/CM ratio is reduced (from 0.25 to 0.22) even when higher HRWR contents are used (3% versus 2%), flowability will drop dramatically. The lower the flowability, the more difficult it becomes for the entrapped air bubbles to be evacuated from the matrix, thus creating more air voids in concrete and as a consequence, resulting in lower strength. After performing several other trial batches using different types and amounts of HRWRs (not reported here for the sake of brevity), a fixed amount of HRWR corresponding to 2% of cementitious materials (C+FA+GGBFS) by weight was found to be an optimum content and thus, was kept constant throughout the rest of the experiments.

For mixes #3 to #15 (except mix #12), 50% of cement was replaced by 25% FA and 25% GGBFS. It should be noted here that for these mixes, Sand 2 with a median particle size of 120 μm was used since it was noticed that it leads to a higher compressive strength and flowability as also recommended and confirmed by Aghdasi et al. [11]. An attempt was made to increase the compressive strength by slightly reducing the W/CM ratio from 0.25 to 0.24 (mix #3 compared to mix #4). However, it was noticed that almost no noticeable change occurs in the compressive strength despite a considerable reduction in the flow diameter from 222 mm to 197 mm.

By comparing mix #3 with mix #5, considerable enhancement in flowability (222 mm versus > 254 mm) was achieved for mix #5 by replacing black undensified silica fume (median particle size of 0.3 μm) with white undensified silica fume of lower carbon content (median particle size of 0.5 μm) without adversely affecting the compressive strength. This proved achievable because the slightly larger median particle size of white undensified silica fume, resulting in a smaller surface area, allowed for a reduction in water demand. Very high compressive strengths of 90.3, 131.0, and 147.5 MPa were recorded for mix #5 after 7, 28, and 56 days, respectively.

After achieving a higher flowability by using white undensified silica fume, W/CM ratio was reduced from 0.25 to 0.24 and 0.22 for mixes #6 and #7, respectively in order to explore the possibility of further increasing the compressive strength. Although no major differences in compressive strengths were observed for these two mixes, a W/CM ratio of 0.22 (mix #7) did reduce the flowability to 210 mm.

For mix #8, using white Portland cement led to a highly flowable matrix with a flow diameter of more than 254 mm while still achieving very high compressive strengths of 99.3, 133.8, and 146.9 MPa after 7, 28 and 56 days, respectively. For mixes #9 and #10, lower W/CM ratios of 0.2 and 0.184, compared to mix #8, were used to explore the possibility of increasing the compressive strength. Similar to the case of mixes #6 and #7, for mixes #9 and #10, no major differences in compressive strengths were recorded. However, using lower W/CM ratios did result in considerable reduction in flowability.

Since glass powder (fine crystalline silica, and hence non-reactive) acts only as a filler between cement particles, mix #11 was performed by completely removing glass powder from the mix design, which allowed for further reduction of the W/CM ratio to 0.176, compared to mix #10, in order to investigate its effects on the flowability and compressive strength. While, by comparing mix #11 with #10, removing glass powder did increase the flowability, the compressive strength seems to have slightly decreased though no strong conclusion could be drawn without a more comprehensive investigation. In mix #12, 50% of cement was replaced with 15% FA and 35% GGBFS in order to study whether using a higher GGBFS content improves the compressive strength. However, by comparing mix #12 with mix #9, both having the same W/CM ratio, it was noted that this change results in no significant difference in compressive strength while it does reduce the flowability.

Mixes #1 to #12 contain either 2.5% or 3.0% of micro steel fibers by volume of concrete. The effect of fiber hybridization on flowability and compressive strength was also investigated. Therefore, two mixes were tested, one with 1.5% SF-5 hooked-end, 0.75% SF-4 long micro, and 0.75% SF-3 short micro steel fibers (mix #13) and the other with 2% SF-5 hooked-end and 1% SF-3 short micro steel fibers by volume of concrete (mix #14). For comparison, mix #15 with no fibers was also tested to explore the effects of fiber addition on flowability and strength. All three mixes (#13, #14, and #15) had a W/CM ratio of 0.20. By comparing mixes #13 to #15, it is observed that addition of fibers (especially SF-5 hooked-end fibers) reduces the flowability as expected, however, it results in a higher compressive strength since fibers allow for redistribution of forces after first cracking and thus, a higher load-carrying capacity. Mix #13 using three different sizes of fibers, resulting in fiber hybridization with a better gradation, appears to lead to higher compressive strengths, possibly due to a more efficient redistribution of forces. The effects of fiber hybridization are investigated in more detail in Section 2.3.2.

Therefore, mix #5, using white Portland cement and a W/CM ratio of 0.25, and mix #8, using ordinary Portland cement and a W/CM ratio of 0.22 over-performed the other mixes in regard to both flowability and compressive strength and therefore, were chosen to investigate the flexural performance of G-UHP-FRC.

2.3.2 Flexural performance of G-UHP-FRC specimens

The flexural performance of mixtures with and without fiber hybridization and fiber volume fractions ranging from 2 to 3% were investigated, the results of which are summarized in Table 4. For this purpose, mixes #16 and #17 (Table 2) were used first, which are essentially the same as mixes #8 and #5 (Table 2), respectively, recommended based on the results of Section 3.1, except for the type and volume fraction of fibers. Mixes #18 and #19 (Table 2) used slightly lower W/CM ratios of 0.23 and 0.22, compared to mix #17 since a similar flowability was achieved at lower W/CM ratios after eliminating PVA fibers from the matrix. For the first 7 batches, 1 prism was tested at 7-day and the other at 56-day for each of which load-deflection curves are illustrated in Figure 3a and Figure 3b, respectively. As expected, the load-deflection curves at 56-day surpass that of the 7-day except for batch #3 where its 7-day prism was tested along the direction of casting, with a more favorable fiber distribution and orientation. For batches #8 and #9, for which mixes #18 and #19 (Table 2) were used, respectively, with ordinary Portland cement, both prisms were tested at 56-day and the load-deflection curves were compared with that of batch #6 (mix #16 – modified mix #8 [Table 2]) (which used white cement instead of ordinary Portland cement), all of which are shown in Figure 3c.

Table 4 - Summary of four-point bending test results of G-UHP-FRC flexural material specimens.

Batch #	W/CM	V_f* (%)	SF-5 Hooked-end* (%)	SF-4 Long Micro* (%)	SF-3 Short Micro* (%)	PVA* (%)	X_f†	7-day			56-day		
								Peak Load (kN)	Deflection at Peak (mm)	σ_r‡ (MPa)	Peak Load (kN)	Deflection at Peak (mm)	σ_r‡ (MPa)
1′	0.22	3.0	1.5	0.75	0.75	0.0	2.37	56.5	0.5410	24.3	71.6	0.7849	30.8
2′	0.22	3.0	2.0	0.0	1.0	0.0	1.89	48.0	0.4445	20.7	67.6	0.8687	29.1
3′	0.22	2.0	2.0	0.0	0.0	0.0	1.09	50.7‴	0.5639‴	21.8	49.4	0.7137	21.3
4′	0.22	2.5	0.0	0.0	0.0	2.5	5.00	18.2	0.1727	7.8	24.9	0.2464	10.7
5′	0.22	3.0	1.5	0.5	0.5	0.5	2.85	56.0	0.8001	24.1	61.8	0.6604	26.6
6′	0.22	2.5	1.5	0.5	0.5	0.0	1.85	46.7	0.8738	20.1	54.3	0.6960	23.4
7″	0.25	3.0	1.5	0.5	0.5	0.5	2.85	60.1	0.7239	25.9	67.2	0.9322	28.9
8-1″	0.23	2.5	1.5	0.5	0.5	0.0	1.85	-	-		50.3	0.8077	21.7
8-2″	0.23	2.5	1.5	0.5	0.5	0.0	1.85	-	-		54.7	0.8052	23.6
9-1″	**0.22**	**2.5**	**1.5**	**0.5**	**0.5**	**0.0**	**1.85**	**-**	**-**		**52.5**	**0.7239**	**22.6**
9-2″	**0.22**	**2.5**	**1.5**	**0.5**	**0.5**	**0.0**	**1.85**	**-**	**-**		**59.2**	**0.8103**	**25.5**

* % by volume of concrete

† Fiber factor ($X_f = V_f \times L_f/d_f$ and $X_f < 2.5$ is recommended for sufficient flowability)

‡ Modulus of rupture

′ White Portland cement

″ Ordinary Portland cement type II/V

‴ Tested parallel to the casting direction

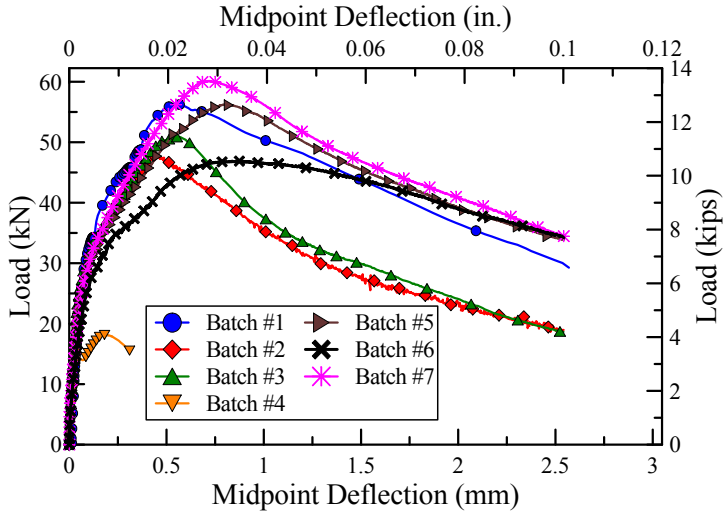

(a)

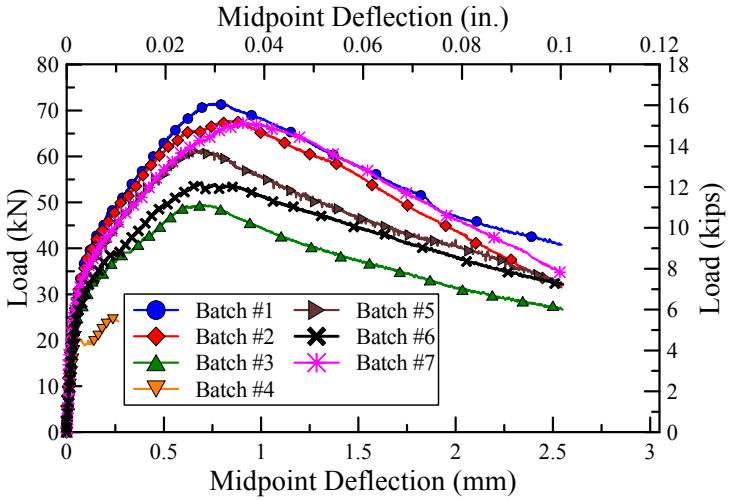

(b)

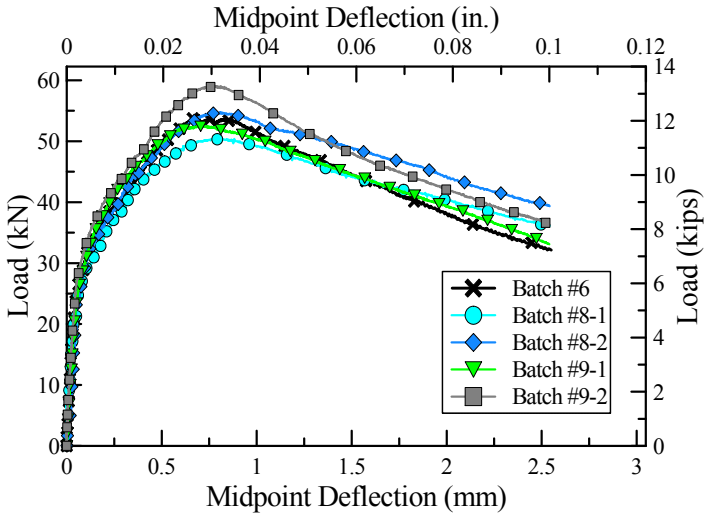

(c)

Figure 3 - Load-deflection curves of G-UHP-FRC 76.2 mm×76.2 mm×279.4 mm prisms under four-point bending at (a) 7-day using white Portland cement, (b) 56-day using white Portland cement, and (c) 56-day using ordinary Portland cement type II/V (compared with batch #6).

According to these results, the highest peak load and deflection at peak values were observed for batches with a cumulative fiber volume fraction of 3% (batch #1, #2, #5, and #7). Except for batch #5 with only 2.5% volume fraction of PVA fibers, all specimens showed very good ductility. By comparing batch #1 with batch #2, it seems that adding SF-4 long micro fibers in addition to the SF-5 hooked-end and SF-3 short micro fibers leads to a higher peak load and deflection at peak. Comparing the results of batch #2 with batch #3, especially at 56-day, does show that adding 1% by volume of micro fibers results in higher strength and ductility as expected since there are more fibers in the matrix that control micro cracks. Batch #4 was made with only 2.5% volume fraction of PVA fibers, which led to a very poor flowability. A premature failure was observed for both prisms tested at 7- and 56-day, due to fracture of PVA fibers shortly after first-cracking. Batch #5, which was made with all four different types of fibers, though was the second most ductile at 7-day, had the second least ductility at 56-day. However, later, batch #7 with the same volume fraction of all four fibers as batch #5 (though with a W/CM ratio of 0.25 and ordinary Portland cement as compared to white Portland cement), resulted in the most ductile prism at 56-day. Since PVA fibers are expensive and considerably reduce the flowability of concrete, batch #6 with 1.5% SF-5 hooked-end, 0.5% SF-4 long micro, and 0.5% SF-3 short micro steel fibers seemed to be a more reasonable choice from an economic point of view. These batches were made using a more efficient mixer with higher shear forces (compared to the preliminary flowability and compression tests presented in Section 3.1), leading to better flowabilities. Therefore, batch #8 was made with the same fiber hybridization as batch #6, however, with ordinary Portland cement, which is more common, and a lower W/CM ratio of 0.23. Since batch #8 was very flowable, batch #9 was made using ordinary Portland cement and a slightly lower W/CM ratio of 0.22, which resulted in reasonable flexural strength and high ductility. According to the results in Table 4 and Figure 3, batch #9 exhibited a comparable performance to that of batch #6. Therefore, batch #9 (mix #19 [Table 2] with a W/CM ratio of 0.22 and 1.5%, 0.5%, and 0.5% volume fractions of 30 mm SF-5 hooked-end, 19 mm SF-4 long micro, and 12 mm SF-3 short micro steel fibers, respectively) was chosen for further investigation of tensile properties and tension-stiffening of G-UHP-FRC.

The effect of fiber hybridization on flowability and compressive strength was also investigated. Therefore, two mixes with a total fiber volume fraction of 3.0% were tested, one with 1.5% SF-5 hooked-end, 0.75% SF-4 long micro, and 0.75% SF-3 short micro steel fibers (batch #2) and the other with 2% SF-5 hooked-end and 1% SF-3 short micro steel fibers by volume of concrete (batch #3). For comparison, a control mix without fibers was also tested to explore the effects of fiber addition on flowability and compressive strength. All three mixes had a W/CM ratio of 0.2. By comparing these mixes, it was observed that addition of fibers (especially SF-5 hooked-end fibers) reduces the flowability as expected but resulted in a higher compressive strength since fibers allow for better load redistribution after first cracking resulting in higher load-carrying capacity. The mixtures that use three different sizes of fibers resulted in higher compressive strengths, possibly due to a more efficient load redistribution and multi-scale crack control.

Compressive strength development of batch #9 (mix #3 [Table 2]) was also investigated by making and testing 50.8-mm G-UHP-FRC cube specimens under compression at different ages. The results are illustrated in Figure 4. It is noted that after 2 days, G-UHP-FRC has a compressive strength of 31.7 MPa that is comparable to that of conventional concrete after 28 days. It is also noticed that after 56 days of age, while the compressive strength development rate does slow down, it still increases with a steady slope, reaching 168 MPa after 680 days. This is believed to be due to continuing hydration and reaction product formation between the industrial by-products (FA,

SF, and GGBFS), and the cement particles. According to ACI Committee 209 [42], it is noted that moist-cured conventional concrete with normal Portland cement reaches approximately 85% of its ultimate strength after 28 days, and therefore, 28-day compressive strength is considered for design purposes. G-UHP-FRC, however, reached, after 56 days, about 83% of its 680-day compressive strength, and therefore, for design purposes, 56-day compressive strength is recommended for G-UHP-FRC mixtures.

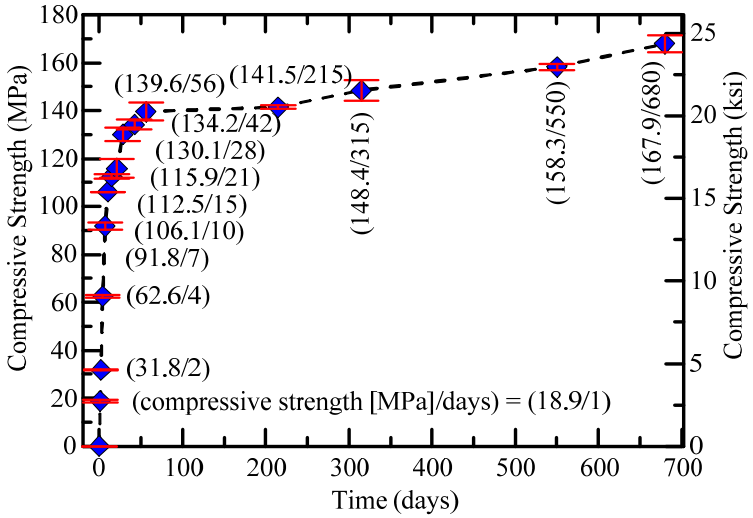

Figure 4 - Compressive strength development of G-UHP-FRC (batch #9 in Table 4).

2.3.3 Tensile test results of large-scale G-UHP-FRC specimens with fiber hybridization (without embedded rebar)

The tensile stress-strain curves and test results obtained from the large-scale dogbone-shaped tension specimens as well as another relevant test result from prior research [11] are all given in Table 5 and Figure 5.

Table 5 - Tensile testing results of dogbone-shaped tension specimens.

Specimen #	Material	W/CM	Fiber Type	V_f	σ_{pt}^* (MPa)	$\varepsilon_{pt}^\dagger$ (%)
Tested in prior research [11]						
1	UHP-FRC‡	0.184	Micro Straight	3.0	8.34	0.17
Tested in this research program						
2	G-UHP-FRC′	0.22	Hybrid	2.5	9.58	0.33
3	G-UHP-FRC″	0.23	Hybrid	2.5	6.83	0.24

* Peak tensile strength
† Strain at peak tensile strength
‡ Based on one tension specimen, tested by Aghdasi et al. [11]
′ G-UHP-FRC (W/CM = 0.22, batch #9 [Table 4], mix #19 [Table 2])
″ G-UHP-FRC (W/CM = 0.23, batch #8 [Table 4], mix #18 [Table 2])

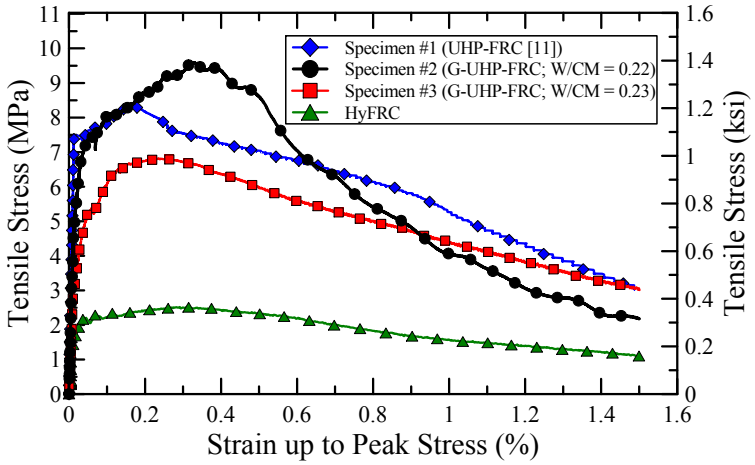

Figure 5 - Tensile stress-strain curves.

In this research, two G-UHP-FRC (specimens #2 and #3) tension specimens (without any embedded rebar) with two different W/CM ratios of 0.22 and 0.23, respectively, were made and tested for comparison purposes. By comparing specimens #2 (G-UHP-FRC) and #1 (UHP-FRC), it is observed that the newly developed G-UHP-FRC that uses three different types of fibers demonstrates a higher tensile strength (~ 15%) and ductility (strain at peak tensile strength of 0.33% that is about 94% higher than that 0.17% of specimen #1 [UHP-FRC]) despite a lower fiber volume fraction and 50% replacement of cement with 25% FA and 25% GGBFS. This enhancement in performance is attributed to fiber hybridization in specimen #2 (G-UHP-FRC). The HyFRC specimen showed a strain at peak tensile strength of 0.32%, which is about the same as that of specimen #2 (G-UHP-FRC), however, it is noted that specimen #2 (G-UHP-FRC) results in a tensile strength of 9.58 MPa, which is about 276% higher than that of the HyFRC specimen. In addition, by comparing specimens #2 (G-UHP-FRC [W/CM = 0.22]) and #3 (G-UHP-FRC [W/CM = 0.23]), it is noted that a slightly higher W/CM ratio of 0.23 compared to 0.22 leads to both lower tensile strength (~ 29%) and ductility (~ 27%). Therefore, batch #9 (Table 4; mix #19 [Table 2]) was used for casting of reinforced G-UHP-FRC specimens to obtain information on its tension-stiffening effect.

2.4 Summary and conclusions

In this research, a more sustainable approach was implemented to develop G-UHP-FRC for small as well as large-scale applications. Compared to UHP-FRC developed in prior research [11], 50% of Portland cement by weight was replaced by 25% FA class F and 25% GGBFS without compromising its later age compressive strength. The effects of various types of mix components and compositions were studied, and mixtures with high compressive strengths of up to 168 MPa were obtained after 680 days. Four-point flexural as well as direct tension tests of G-UHP-FRC were performed to further investigate and enhance its flexural and tensile mechanical properties by utilizing and optimizing a hybrid combination of different types of fibers. In addition, compressive strength development of G-UHP-FRC was monitored over a period of 680 days.

To summarize, the following conclusions can be drawn from the results presented in this chapter:

1. G-UHP-FRC mixtures with high flowability and compressive strengths exceeding 125 and 140 MPa after 28 and 56 days, respectively, were developed. This was achieved while 50% of Portland cement was replaced by 25% FA and 25% GGBFS.
2. Based on flexural experiments of G-UHP-FRC under 4-point bending, a total fiber volume fraction of 2.5% by volume, including 1.5% SF-5 hooked-end, 0.5% SF-4 long micro, and 0.5% SF-3 short micro steel fibers achieved sufficient post-cracking ductility and post-peak load-carrying capacity under flexure and uniaxial tension.
3. Compressive strength development of G-UHP-FRC was monitored over an extended period of about two years, which showed ever-increasing strength with the highest recorded value of about 168 MPa after about two years. For structural design purposes with G-UHP-FRC, it is recommended to use the 56-day compressive strength, which is about 83% of its highest recorded compressive strength. It was also noted that G-UHP-FRC at 2-day had obtained a comparable compressive strength to that of conventional concrete. All specimens were cured in the fog room (with more than 95% relative humidity at room temperature) until a day before testing.
4. High tensile strength (9.58 MPa) and high ductility (0.33% strain at peak tensile strength) were observed for a large-scale dogbone-shaped G-UHP-FRC tension specimen (without embedded rebar) tested under monotonic tensile forces.

Chapter 3

A Concrete Metamaterial: Octet-Truss Engineered Concrete (OTEC) for Lightweight Structures

3.1 Introduction

Materials for energy-efficient building systems, such as façade and flooring systems, must have a balance of strength, stiffness, low weight, and thermal resistance. Finding the optimum balance of these properties leads to both structural and non-structural improvements throughout the building. Building energy consumption comprises almost half of all energy usage in the U.S., and 45% of this is used for heating, cooling, and ventilation [43]. The magnitudes of these numbers highlight the need for thermally resistant façade systems. Materials with high thermal resistance and sufficient strength enable adequate insulation while keeping the weight and thickness of the building envelope to a minimum. Façade and flooring systems make up a large portion of the dead load in a building; thus, reductions in weight are reflected in the required structural system, particularly in earthquake-prone regions.

Foam concretes have been used for many years for lightweight, thermally resistant façades due to their low weight and good thermal properties. The most common method of producing foam concrete is the addition of aluminum powder, which reacts with calcium hydroxide in the cement paste to produce hydrogen bubbles resulting in a random pore structure throughout the cement matrix [44–46]. This random pore structure leads to an exponential decrease in strength and stiffness with increasing porosity, which is the main drawback of the use of foam concretes [26,47].

It is well known that cellular solids can deform in two ways: 1) bending or 2) stretching of the cell walls [48]. Poor mechanical performance of foam concretes is attributed to the stress flow in randomly distributed spherical pores. This type of microstructure is classified as bending-dominated. As shown in Figure 6, stresses applied to the material cause flexure in the pore walls that leads to the development of tensile stresses, causing a drop in the overall strength of the foam since cement paste has poor tensile capacity compared to its compressive strength. Stretching-dominated lattices overcome this behavior by arranging the material such that all elements are subjected to predominantly axial stresses, as shown in Figure 6 [26]. Although most cellular solids

are bending-dominated, those that are stretching-dominated are more efficient from a weight viewpoint for structural applications. This is because stretching-dominated cellular solids have a greater macroscopic modulus and initial yield strength compared to bending-dominated cellular materials of the same relative density. Stretching-dominated materials, however, have a softening post-yield response because of plastic buckling or brittle collapse of their struts [7,49]. Stretching-dominated lattices, such as octet-truss lattices, have been proven to be effective for metals and ceramics [27,50,51]. Octet lattices seem to be ideal for concrete as well, especially if the concrete exhibits ultra-high compressive strength since a compressive stress field places all elements in the lattice under compression. By arranging the material in this optimum pattern, higher strength and stiffness are achievable in an octet-truss lattice compared to foams with equivalent density.

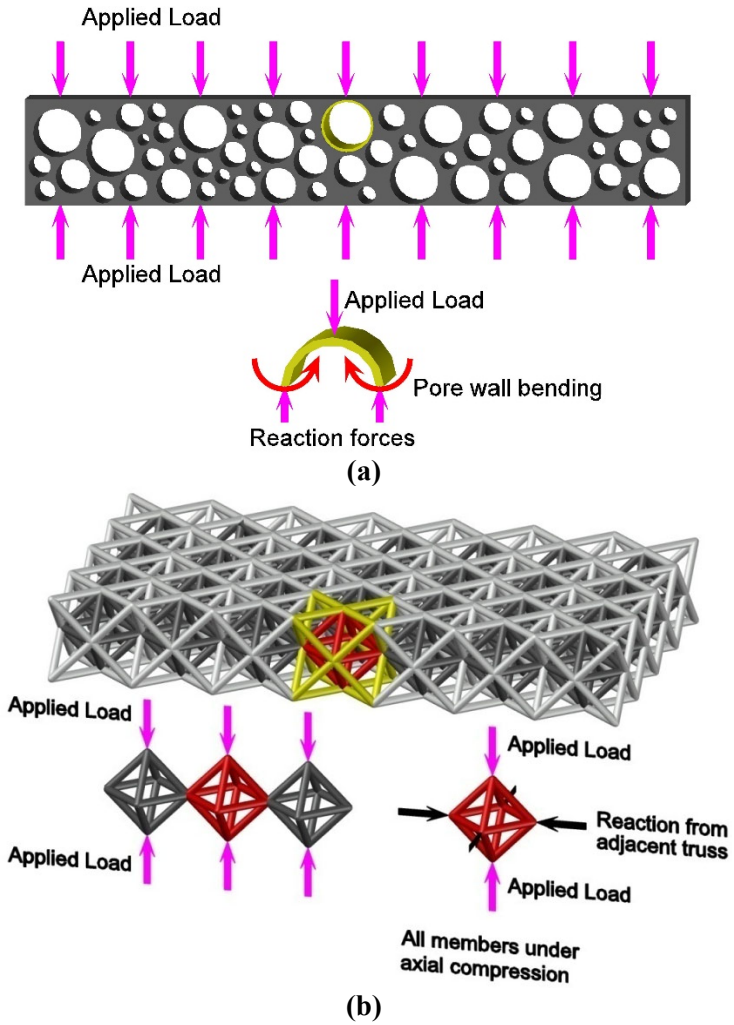

Figure 6 - (a) Bending of pore walls in foams (bending-dominated) and (b) stress flow in stretching-dominated lattices (octet-truss lattice).

Ultra-High Performance Fiber-Reinforced Concrete and green UHP-FRC developed in this research (Chapter 2) were used to manufacture Octet-Truss Engineered Concrete (OTEC) lattices. The performance of both G-UHP-FRC and UHP-FRC OTECs are investigated here, which could potentially be used in lightweight structures, such as energy-efficient building façade and flooring systems.

3.2 Fabrication of OTEC lattices with different porosities

3.2.1 Materials

Information for the materials used in here as well as mixture compositions are all summarized in Table 6. Flowability of the mixtures was examined according to ASTM C1437-07 [13]. In both G-UHP-FRC (mix #5 in Table 2, Chapter 2) and UHP-FRC (slightly modified third trial mix in Table 2, Chapter 2) mixtures, 0.5–2.0% by volume of 3 mm-long high modulus, ultra-high molecular weight polyethylene fibers of 38.4 μm diameter, with a tensile strength and elastic modulus of 2.2–2.4 GPa and 73–79 GPa, respectively, were introduced in order to obtain sufficient post-cracking ductility. Such short polyethylene fibers are desirable to ensure that the mixture is able to flow through the corners of the octet lattice mold without clogging during infiltration.

Table 6 - Materials and mixture compositions used in the experimental program.

Material	Description	Size*/Length (L)	G-UHP-FRC	UHP-FRC	Conventional Concrete†
Silica Sand 1 (S1)	460 Mesh	460 μm	0.7	0.6	0.0
Silica Sand 2 (S2)	120 Mesh	120 μm	0.3	0.3	0.0
Fine aggregate	90 Mesh	90 μm	0.0	0.0	2.05
Fiber‡	Polyethylene (PE)	38.4 μm / 3 mm	0.022′	0.005–0.016′	0.0
Cement (C)	Type II/V	15 μm	0.5	1.0	1.0
Fly Ash (FA)	Class F	10 μm	0.25	0.1	0.18
GGBFS″	-	15 μm	0.25	0.0	0.0
Glass Powder (GP)	White Micro Silica	1.8 μm	0.25	0.25	0.0
Silica Fume (SF)	Black Undensified	0.3 μm	0.0	0.25	0.0
	White Undensified	0.5 μm	0.25	0.0	0.0
HRWR‴	Polycarboxylate-based	-	0.02	0.02	0.0024
W/CM£	-	-	0.25	0.26	0.51
Flow diameter (mm)	-	-	254	224	254

* Median particle size
† Used in Section 3.3.2 as a control mix for comparison purposes
‡ High modulus, ultra-high molecular weight polyethylene fibers with a tensile strength and elastic modulus of 2.2–2.4 GPa and 73–79 GPa, respectively
′ 2.0, 1.5, 1.5, and 0.5–1.5% by volume, respectively
″ Ground granulated blast-furnace slag
‴ High-range water reducer
£ Water [W]/CM = [W/(C+FA+GGBFS+SF)]

Compressive strengths of 110–140 MPa were achieved for G-UHP-FRC and UHP-FRC (see Table 7 on page 33) based on 50.8-mm solid cube specimens along with high flowability of more than 220 mm, which later proved to be essential for the extrusion of G-UHP-FRC and UHP-FRC into 3D-printed octet lattice molds. The purpose of using UHP-FRC developed in prior research [11] was to enhance the compressive strength of OTEC unit cells, thereby providing a wider range of possibilities for future applications based on project requirements. UHP-FRC (Table 6), while using 100% cement, required a slightly higher water-to-cementitious materials ratio, W/CM ratio of 0.26, compared to prior research [11] in order to achieve sufficient flowability for proper infiltration of the 3D-printed octet lattice molds.

3.2.2 Octet lattice negative molds 3D-printed in Acrylonitrile Butadiene Styrene (ABS)

Creating the complex geometry of the octet-truss, illustrated in Figure 7a, from G-UHP-FRC or UHP-FRC, is difficult using traditional mold-making techniques. In recent years, however, additive manufacturing has enabled researchers and scientists to create complex geometries with great ease. In this study, negative octet molds, shown in Figure 7b, were 3D-printed in acrylonitrile butadiene styrene (ABS) using fused deposition modeling on a Stratasys Dimension 1200es printer. ABS filaments were deposited with a layer thickness of 0.1 mm to give a mold surface roughness that was tens of times smoother than the sizes of individual octet struts.

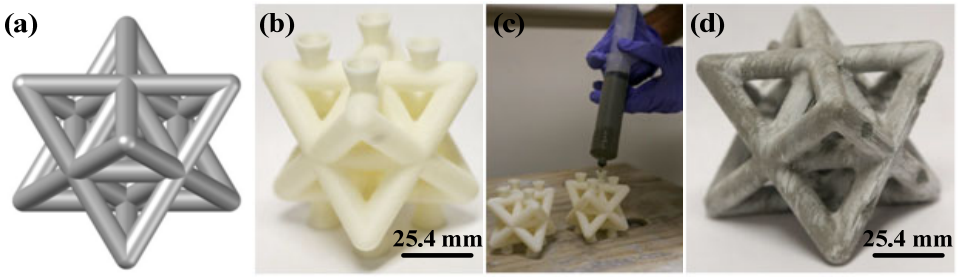

Figure 7 - (a) Schematic drawing of an octet lattice unit cell, (b) 3D-printed octet lattice unit cell ABS mold, (c) infiltrating molds on a vibrating table, and (d) final G-UHP-FRC/UHP-FRC OTEC unit cell.

Each octet mold cavity contains multiple overhanging regions, so, to prevent mold collapse during the layer-by-layer printing process, a pattern of soluble support material, Stratasys P400, was deposited into the cavities from the 3D printer's second extrusion nozzle. Once mold printing was complete, the support material was dissolved by placing the mold into a caustic lye bath (NaOH, with a concentration of about 2.0%) at 70°C for 2–3 days and then rinsing in tap water. This process resulted in a hollow mold prior to concrete infiltration.

3.2.3 Infiltration of Octet lattice negative molds

Four methods were used to infiltrate the 3D-printed ABS molds. Excellent flowability of G-UHP-FRC and UHP-FRC provided for the possibility of infiltrating these molds on a vibrating table, using a syringe as illustrated in Figure 7c. The printed mold incorporated eight small funnels (four for injection and four for inspection during infiltration) to serve as injection, inspection, and air exhaust sites. The molds were designed with a wall thickness of 1 mm, making them dissolvable upon immersion in acetone after infiltration and solidification. In this approach, vibration as well as positive pressure applied by using a syringe during extrusion were the mechanisms used to remove entrapped air. This method proved to be quite effective except in a couple cases where a few air voids were observed on top of the octet lattice unit cells after dissolving the ABS mold in acetone. Consequently, it was decided to try a few other methods to investigate whether entrapped air could be more effectively removed.

In the second approach, the molds were first infiltrated on top of a vibrating table (as in the first approach), and were then placed in a vacuum chamber (Bel-Art 42025 with 230mm plate) at 745 mbar for 1 minute to remove any remained entrapped air. The molds were then re-infiltrated to fill any space at the top of the mold cavity and placed back into the vacuum chamber. This process was repeated until no further air bubbles could be extracted from the molds. This method was

found to be very effective for obtaining air bubble-free octet lattice unit cells although it was somewhat laborious and impractical.

In the third approach (Figure 8b), an additional push-fit inlet adapter was printed onto the ABS mold, as shown in Figure 8a, to enable it to be connected via elastomeric piping to a vacuum system (at 745 mbar) from one side while G-UHP-FRC/UHP-FRC was being infiltrated into the mold using a syringe from the opposite side. This setup meant that the mold would, to a large extent, be evacuated before G-UHP-FRC/UHP-FRC entered it, potentially reducing the risk of bubble entrapment. Furthermore, the vacuum was expected to help extract any air bubbles that had been entrained in the G-UHP-FRC/UHP-FRC mixture prior to infiltration. A trap was introduced between the vacuum system and the mold to prevent any material from entering the vacuum system. This method, however, was not found very effective, on the one hand because the ABS molds were not completely air-tight, and on the other hand because vacuum without vibration could not effectively extract entrapped air bubbles. Indeed, a few octet lattice unit cells made using this approach had visible large defects.

Therefore, a fourth method was proposed, as illustrated in Figure 8c, that used a separatory funnel to infiltrate G-UHP-FRC/UHP-FRC into ABS molds that had been printed with thicker (1.8 mm) walls to make them air-tight. The valve of the separatory funnel allowed the flow of G-UHP-FRC/UHP-FRC to be controlled independently of the vacuum, the idea being that the mold cavity could be completely evacuated before any G-UHP-FRC was introduced, fully eliminating air entrapment. However, it was found that the high strength of vacuum developed inside the mold caused separation of the G-UHP-FRC/UHP-FRC mixture and extraction of sands with larger particle sizes from the matrix. This separation resulted in the formation of a rather dry matrix, clogging the vacuum tubing between the separatory tube and the mold and preventing the matrix from filling the mold.

It was therefore decided to use the first approach throughout most of the remaining experiments, since, while still quite effective and practical, it required considerably less effort. Through repetition, this approach was mastered in such a way that G-UHP-FRC/UHP-FRC OTECs with no visible defects could be produced.

Figure 7d shows the final G-UHP-FRC/UHP-FRC OTEC unit cell after dissolving the ABS mold in acetone.

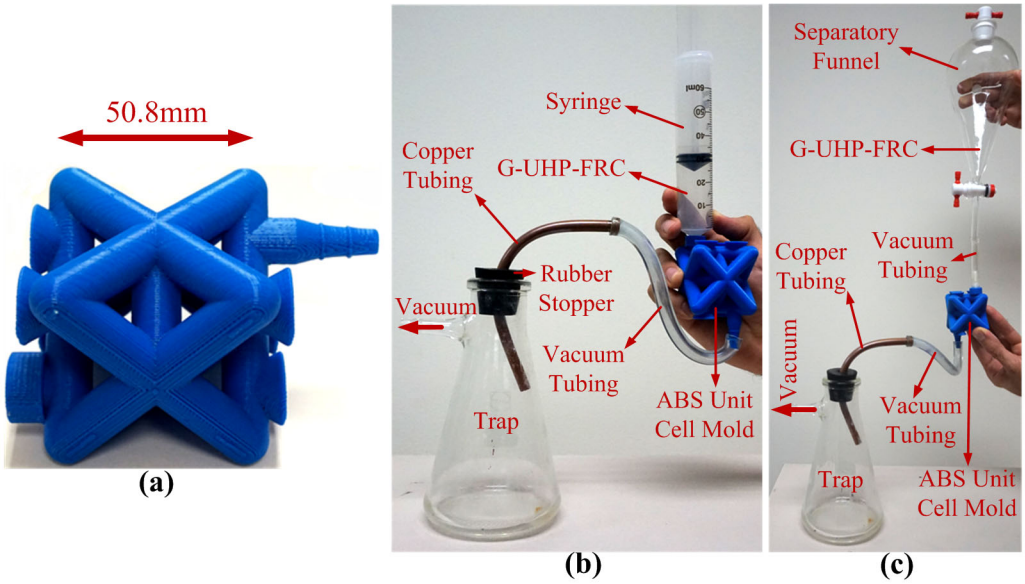

Figure 8 - (a) ABS mold with an additional push-fit inlet adapter; infiltration of octet lattice unit cell molds with G-UHP-FRC/UHP-FRC using the (b) third approach (negative pressure created by vacuum + positive pressure using a syringe) and (c) the fourth approach (negative pressure throughout the whole system using vacuum and a separatory funnel).

3.2.4 Dissolving the ABS molds in acetone

Upon adequate infiltration, the specimens were left to set in a fog room (with more than 95% relative humidity at room temperature) for about 24 hours, after which they were placed in an acetone bath at room temperature for 24–48 hours to dissolve away the ABS mold. Prior to using this manufacturing technique, the effect of acetone on the compressive strength of G-UHP-FRC was tested by placing three 50.8-mm solid cubes of G-UHP-FRC in an acetone bath for 24 hours and then testing them under compression. The compressive strengths of these cubes were compared to three control 50.8-mm solid cubes from the same batch that had not been placed in acetone. The average compressive strength of the samples exposed to acetone differed by less than about 3% from that of the control specimens, with the acetone-exposed specimens exhibiting the slightly higher average strength. These results sufficed to show that acetone does not adversely influence the mechanical properties of G-UHP-FRC and UHP-FRC.

3.2.5 Curing OTEC material specimens

After dissolving away the ABS molds, all material specimens, with the exception of a few, were placed in a fog room (with more than 95% relative humidity at room temperature) until a day before testing (usually at 28 days after casting). Although not quantified in this research, it is believed that due to high particle packing density of the developed G-UHP-FRC/UHP-FRC, water permeation is limited to only a few millimeters from any exposed surface. Therefore, though water/moisture curing may not have a noticeable effect on the compressive strength development of 50.8-mm solid cube specimens, it was believed that it would most likely affect strength development of OTEC unit cell elements since the diameter sizes varied from only 8 to 12 mm, allowing water and moisture to penetrate the elements almost all the way through.

Hence, in order to investigate the effects of different types of water/moisture curing on the compressive strength development of OTEC unit cells, eight specimens with 8 mm-diameter elements were made and cured using three different methods for comparison purposes. Two specimens were cured at room temperature and humidity as control samples, three specimens were cured in the fog room, and three more were immersed in water, all of which were removed from their curing environment a day before testing (at 28 days after casting).

3.3 Mechanical testing

3.3.1 Uniaxial compression tests of OTEC material specimens

Throughout this research, $(50.8\ \text{mm})^3$ OTEC unit cell material specimens were made with four different element diameters of 8, 10, 11, and 12 mm, resulting in void fractions (porosities) of 66.4, 53.6, 47.5, and 41.9%, respectively, as compared to a 50.8-mm solid cube. These OTEC unit cells were tested under compression using holders whose geometries were customized for each element diameter. In most cases the holders were milled from 6061 aluminum, as shown in Figure 9. The purpose of using a holder is to properly restrain the nodes of the truss from lateral displacement, and thus simulate the stress state that exists in octet lattice structures having many cells in at least two directions, as would be found, for example, in an OTEC panel. Large two- or three-dimensional arrays of OTEC cells are almost completely stretching-dominated structures, and when loaded compressively at their largest two opposing boundaries (*e.g.* on opposite sides of a panel), all their struts experience largely uniaxial compressive loads. In contrast, if a single isolated octet unit cell, or just a few cells, were to be loaded without lateral constraints, relatively large flexural as well as tensile loads would be induced in some elements, leading to behavior that would not be representative of that anticipated in larger built structures.

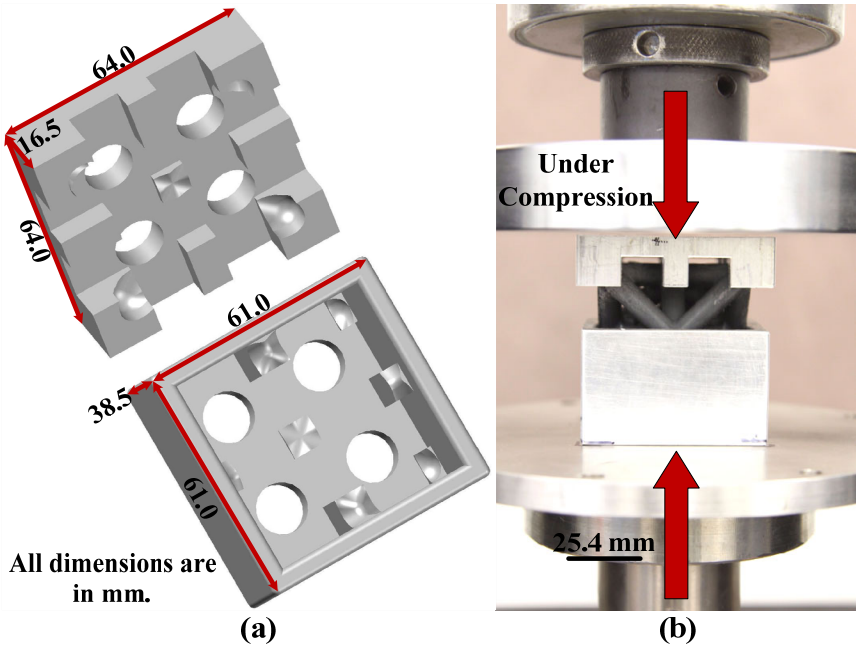

Figure 9 - (a) Aluminum holder for compression test of OTEC unit cell material specimens and (b) an OTEC unit cell with 8 mm-diameter elements under compression using the aluminum holders.

In addition to OTEC unit cell material specimens, companion G-UHP-FRC and UHP-FRC 50.8-mm solid cube material specimens were made and tested under compression for comparison purposes. Compressive strengths of both 50.8-mm solid cube and OTEC unit cell material specimens were obtained in accordance with ASTM C109/109M-16 [14].

Four sets of OTEC unit cell material specimens were made and tested under compression throughout this research. In the first set of experiments, nine OTEC unit cells with 8, 10, and 12 mm-diameter elements were made using G-UHP-FRC (Table 6) in order to quantify the effects of varying the void fraction of an OTEC unit cell on its compressive strength. These samples were later tested under uniaxial compression using 3D-printed ABS holders. Soon, it was realized that these ABS holders were not very effective in restraining the nodes since multiple cracks were induced in the holders during testing. Therefore, for the remaining experiments, the holders were machined from 6061 aluminum, as mentioned above. In addition, a few more trial OTEC unit cells with 8 mm-diameter elements were made with a slightly different mix designs to explore the possibility of enhancing their compressive strengths compared to the results thus far collected.

Furthermore, in the first set of experiments, two 50.8-mm foam G-UHPC (G-UHP-FRC without fibers) cubes with a void fraction of 45.3% were also made and tested under compression, for comparison purposes with OTEC unit cells. Foaming was induced by aluminum powder that was added to G-UHPC during the mixing procedure. Aluminum powder reacts with the hydration products, especially calcium hydroxide, and results in the formation of tricalcium aluminate hydrate and hydrogen gas, which introduces entrapped air bubbles throughout the matrix.

In the second set of experiments, UHP-FRC (Table 6), using 100% cement and a slightly higher W/CM ratio of 0.26, was used to make six OTEC unit cell material specimens with 8 mm-diameter elements. The purpose of this experiment was to investigate the effects of three different fiber volume fractions (0.5, 1.0, and 1.5%) on the flowability of their matrices as well as the compressive strengths and post-cracking behavior of the OTEC unit cells. It should be noted here that in a few instances in this experiment, some flexural cracks were observed in a few elements that were attributed to the lack of sufficient depth of the top piece of the aluminum holder, thus allowing for some of the top nodes to slide transversely, inducing flexural moments. Therefore, for the rest of the experiments, the holder design was revised to include a deeper top piece, ensuring that all top nodes were properly restrained from any transverse displacement.

In the third set of experiments, UHP-FRC (Table 6) was used to make eight more OTEC unit cells with 8 mm-diameter elements to explore the effects of water/moisture curing on their compressive strength development.

In the fourth set of experiments, it was decided to continue using UHP-FRC with 0.5% volume fraction of fibers to make and test twelve more OTEC unit cells with 8, 10, and 11 mm-diameter elements in order to duplicate the results thus far achieved, by once more quantifying the effects of varying the void fraction of an OTEC unit cell on its compressive strength.

The G-UHP-FRC 50.8-mm solid cube, foam cube, as well as 8,10, and 11 mm OTEC unit cell material specimens are all illustrated in Figure 10. In addition, using UHP-FRC, a 3×3×1-cell OTEC panel with 8 mm-thick flanges on both sides and 8 mm-diameter elements, which is shown in Figure 11a, was cast successfully without any visible surface voids or defects.

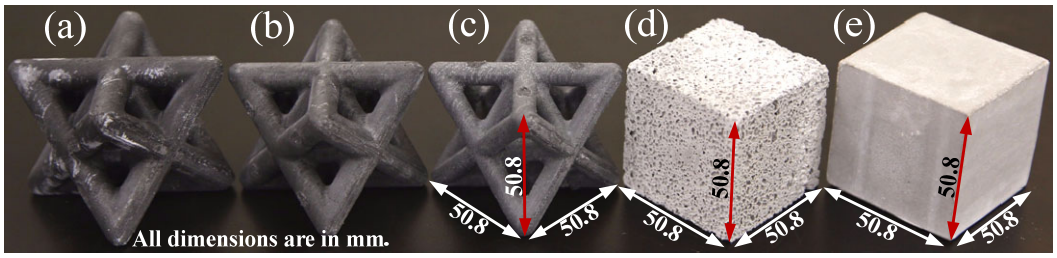

Figure 10 - 50.8-mm side-length UHP-FRC OTEC unit cell material specimens with (a) 11, (b) 10, and (c) 8 mm-diameter elements and (d) 50.8-mm foam G-UHPC cube and (e) 50.8-mm solid G-UHP-FRC cube material specimens before testing under uniaxial compression.

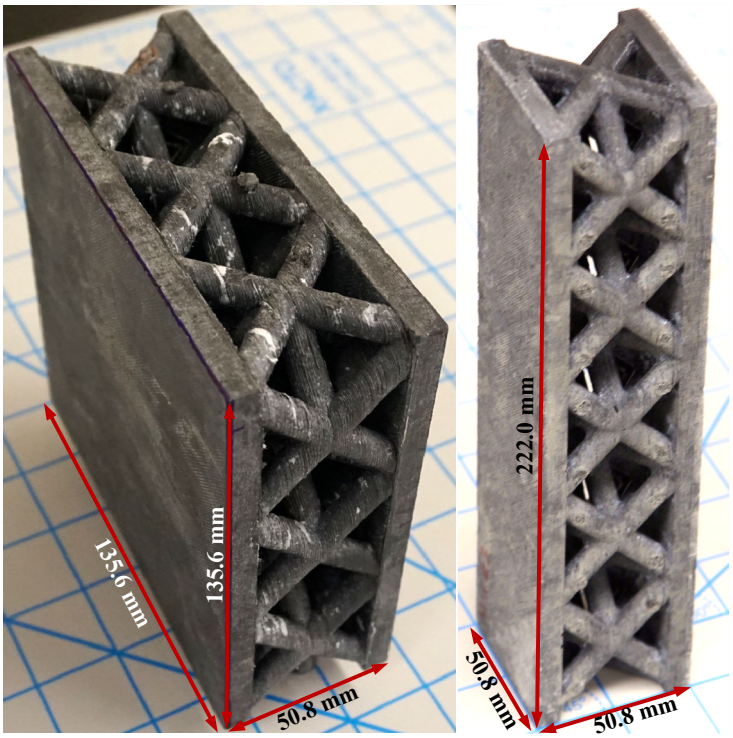

Figure 11 - (a) 3×3×1-cell OTEC panel showing surface defect-free production and (b) 5×1×1-cell OTEC flexural material specimen.

Furthermore, it was desired to understand whether the dependence of compressive strength on void fraction that was observed in Experiments #1 and #4 could also be seen with a polymeric material and in structures with a higher confidence of having no surface or internal void defects. Therefore, three further octet lattice unit cells with 8, 10, and 11 mm-diameter elements as well as a 50.8-mm solid cube were directly printed from the polymer polylactic acid (PLA) using a Type A Pro fused deposition modeling machine. These samples were also then tested under uniaxial compression (Experiment #5).

For the first two sets of experiments, the OTEC unit cells were tested under compression using a hydraulic load-controlled machine with a constant loading rate of 1.5 kN/sec, while, for the last three experiments, all specimens were tested using a displacement-controlled machine at a constant displacement rate of 6 mm/min. The latter approach allowed for recording the cross-head displacement, from which compressive stress-strain curves were generated.

In addition, theoretical strength values for 8, 10, and 11 mm UHP-FRC OTEC unit cells were calculated using the structural analysis software package OpenSees [52], where two formulations were used to model the specimens for comparison purposes. The first, and simplest, model uses pinned truss elements and a brittle material model. In this model, each member of the OTEC specimen is modeled with a single truss element. This type of model is most commonly used to predict the strength of structures with slender elements, as flexural behavior has only a minor effect on such elements and is often neglected. The second formulation uses a force-based beam-column element with a circular fiber section at each integration point and a brittle material model. Each member is divided into four beam-column elements to improve accuracy. This model is better suited to less slender elements because it accounts for flexural behavior in the elements, though it neglects shear deformations. Horizontal displacements and all rotations were restrained in the nodes for all three specimens to mimic the boundary conditions imposed by the aluminum holders used in the experimental tests. Vertical displacement was restrained in the bottom nodes and imposed on the top nodes by the displacement-controlled integrator used in analysis.

Compression test results of all of the OTEC unit cells, 50.8-mm foam, and solid G-UHP-FRC and UHP-FRC cubes after 28 days of curing (unless otherwise specified) are summarized in Table 7.

Table 7 - Compression test results of OTEC unit cells and foam and solid G-UHP-FRC and UHP-FRC cubes after 28 days (unless otherwise specified).

Specimen	Exp. #	Fiber V_f* (%)	Porosity (%)	Density (kg/m^3)	Compressive Strength (MPa)				Standard Error (MPa)	Average Strength (MPa)
					#1	#2	#3	#4		
8 mm OTEC	1‖	2.0	66.4	769	5.5	6.2	9.7	-	1.3	7.1
10 mm OTEC		2.0	53.6	1,063	12.1	8.4	10.0	-	1.1	10.2
12 mm OTEC		2.0	41.9	1,330	19.2	16.2	14.5	-	1.4	16.6
Solid cube†		2.0	0.0	2,290	123.9	137.0	124.1	-	4.3	128.3
Foam cube‖		0.0	45.3	1,274	4.8	3.7	-	-	-	4.3
Solid cube‖		0.0	0.0	2,329	116.4	-	-	-	-	116.4
8mm lattice cell‡	1ǂ	1.5	66.4	763	**12.8**	7.0	-	-	-	9.9
Solid cube‡		1.5	0.0	2,271	139.8	145.0	137.8	-	2.1	140.9
8mm lattice cell	1‖	1.5	66.4	761	7.6	9.5	**10.7**	-	0.9	9.3
Solid cube		1.5	0.0	2,266	118.8	126.6	-	-	-	122.7
8 mm OTEC	2ǂ	0.5	66.4	772	6.1	5.4	-	-	-	5.7
Solid cube		0.5	0.0	2,298	112.1	117.2	106.1	-	3.2	111.8
8 mm OTEC		1.0	66.4	762	4.7	6.3	-	-	-	5.5
Solid cube		1.0	0.0	2,267	111.6	105.6	109.9	-	1.8	109.0
8 mm OTEC		1.5	66.4	750	4.7	5.0	-	-	-	4.8
Solid cube		1.5	0.0	2,233	106.4	107.1	104.1	-	0.9	105.9
8 mm OTEC′	3ǂ	0.5	66.4	763	8.0	8.8	-	-	-	8.4
8 mm OTEC″		**0.5**	**66.4**	**763**	**13.0**	**10.0**	**12.5**	**-**	**0.9**	**11.8**
8 mm OTEC‴		0.5	66.4	763	**10.7**	**11.3**	**11.7**	-	0.3	11.3
8 mm OTEC£	4ǂ	**0.5**	**66.4**	**763**	**12.2**	**11.7**	**13.8**	**10.7**	**0.7**	**12.1**
10 mm OTEC£		0.5	53.6	1,053	19.6	18.2	15.4	13.9	1.3	16.7
11 mm OTEC£		0.5	47.5	1,192	21.4	19.6	22.3	22.4	0.6	21.4
Solid cube£		0.5	0.0	2,270	149.4	139.8	-	-	-	144.6
8 mm PLA lattice cell	5	-	66.4	356	5.7	-	-	-	-	5.7
10 mm PLA lattice cell		-	53.6	492	9.3	-	-	-	-	9.3
11 mm PLA lattice cell		-	47.5	556	13.3	-	-	-	-	13.3
Solid PLA cube		-	0.0	1,060	-	-	-	-	-	-

* Fiber volume fraction
† Tested after 225 days
‡ Tested after 39 days
′ Cured at room temperature and humidity
″ Cured in the fog room with more than 95% relative humidity at room temperature
‴ Immersed in water
£ Tested after 50 days
╫ G-UHP-FRC
╪ UHP-FRC
‖ G-UHPC

The results of the first set of experiments show that it is possible to obtain much higher compressive strengths from G-UHP-FRC/UHP-FRC OTEC unit cells than from foam G-UHPC cubes with a comparable void fraction. As later confirmed in the fourth and fifth set of experiments, it was further noticed that an OTEC unit cell with 8 mm-diameter elements (referred to as the "8 mm OTEC" in Table 7) demonstrates a higher specific compressive strength than that of an estimation expected from a log-log regression based on the strength values of the other specimens with lower porosities (*i.e.* the 10 and 12 mm OTEC unit cells and the 50.8-mm solid cube). Therefore, for the next two experiments (Experiments #2 and #3), 8 mm OTEC unit cells were used to further study the effects of various fiber volume fractions and different curing methods on their compressive strengths. In addition, these experiments were carried out with the aim of further enhancing the compressive strengths of the 8 mm OTEC unit cells beyond 10 MPa.

In the second set of experiments, the effects of fiber volume fraction on both fresh and hardened properties were investigated, and as the results in Table 7 suggest, a somewhat linear reduction in strength, as well as flowability (not measured quantitatively, but observed qualitatively) is noticed with an increase in the fiber volume fraction for both the solid cubes and 8 mm OTEC unit cells. This effect is believed to be due to the fact that reduced flowability is more likely to result in more entrapped air and small defects, thus lowering the strength. The fibers do, however, increase post-cracking toughness by adding more ductility to the matrix.

In the third set of experiments, in which three different methods of curing were employed, a 40% increase in compressive strength was achieved by curing the 8 mm UHP-FRC OTEC unit cells in the fog room versus under regular room conditions. This pronounced effect gives validity to the assumption made earlier, since the strut diameter is only 8 mm, water and moisture are able to penetrate sufficiently far into the elements to allow for a higher degree of cement hydration. The goal of reaching more than 10 MPa in compressive strength was accomplished for all of the specimens that were either cured in the fog room or immersed in water, which are indicated in bold in Table 7. Although all material specimens were removed from their curing environment and moved to room temperature and humidity a day before testing, this does not appear to have led to the elements drying out internally. After compressive testing, fragments of all OTEC unit cells that had been either immersed in water or kept in the fog room, were examined visually, and the UHP-FRC was seen to be still wet inside, further confirming the penetration of water into the elements. A slightly lower average compressive strength (~4% lower) was measured for the OTEC unit cells that had been immersed in water compared to those cured in the fog room, but this difference is not statistically significant as indicated by a one-sided Student's t-test performed at the 5% level of significance.

The stress-strain curves for all 8 mm UHP-FRC OTEC unit cells tested during this experiment are shown in Figure 12. Figure 12d further demonstrates higher stiffness, peak load, strain at peak

(higher ductility), and toughness for the material specimens that were either cured in the fog room or immersed in water compared to those that were merely kept at room temperature and humidity.

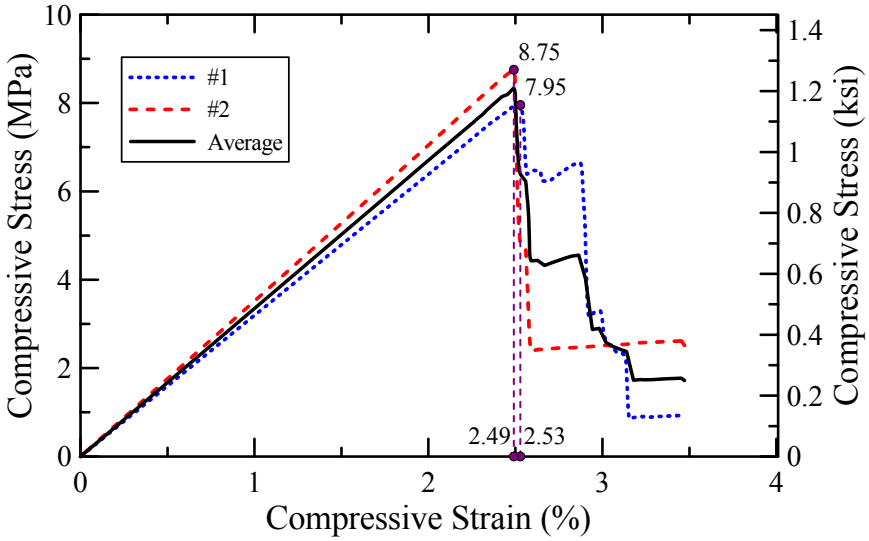

(a)

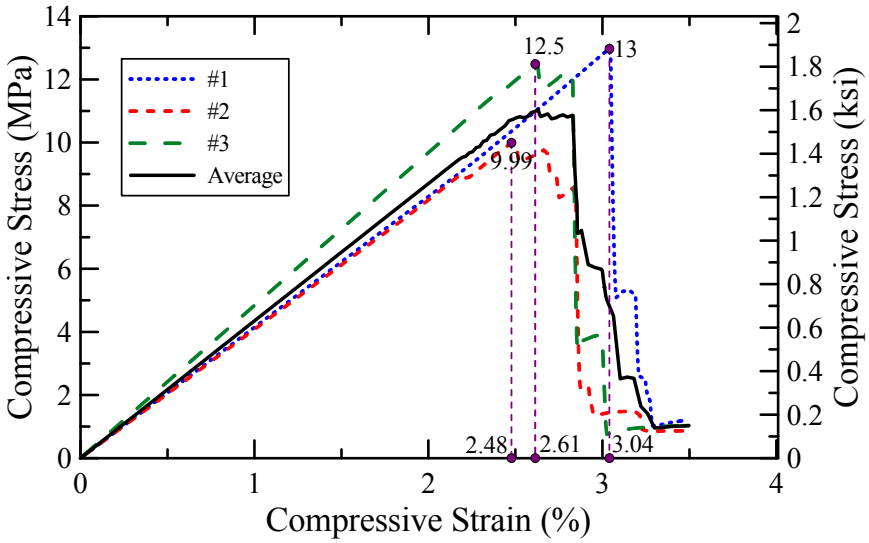

(b)

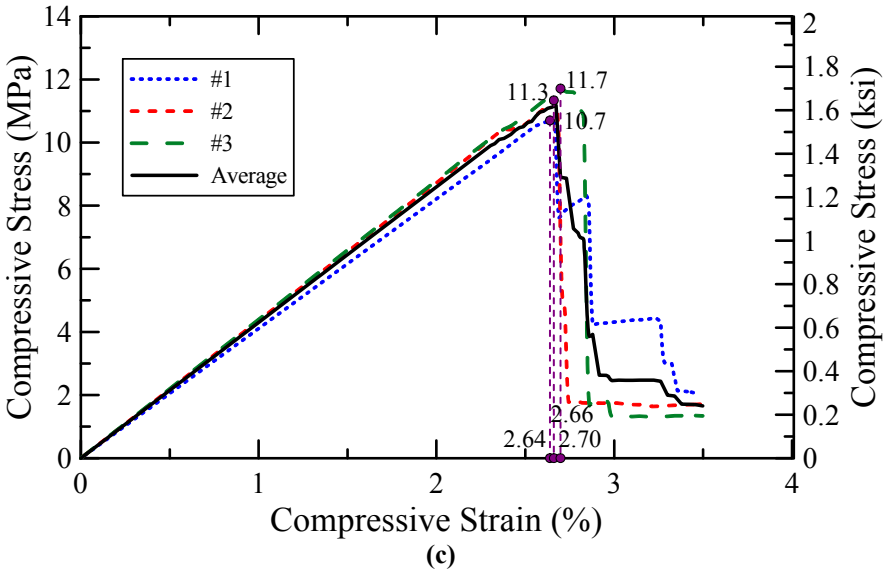

(c)

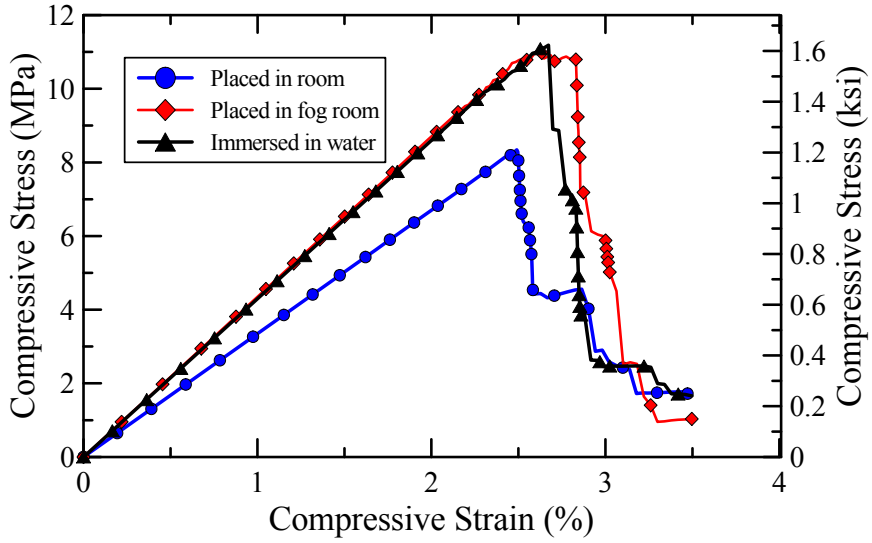

(d)

Figure 12 - Stress-strain curves for 8 mm UHP-FRC OTEC unit cells (a) cured at room temperature and humidity, (b) placed in the fog room (with more than 95% relative humidity at room temperature), and (c) immersed in water until a day before testing, and (d) average stress-strain curves for 8 mm UHP-FRC OTEC unit cells cured using three different methods (Experiment #3).

According to the results of the fourth set of experiments, compressive strengths well beyond 10 MPa were measured for all four 8 mm OTEC unit cells. An average increase of 38% and 77% in compressive strength were obtained for 10 and 11 mm OTEC unit cells, respectively, compared to 8 mm OTEC unit cells. As for the failure mode of the UHP-FRC OTEC unit cells tested in Experiments #3 and #4, all diagonal elements experienced columnar failure under compression characterized by development of tensile cracks along the direction of these elements. UHP-FRC, like other types of concrete, is much weaker in tension than in compression (~1/10); thus, when a UHP-FRC element is tested under compression, its lateral expansion (due to Poisson's effect) followed by development of lateral tensile stresses ultimately results in the formation of tensile cracks along the direction of the applied compressive force. This phenomenon explains the formation of cracks along the diagonal elements of the UHP-FRC OTEC unit cells (Figure 13a) as

well as the vertical cracks that were observed after testing the 50.8-mm solid UHP-FRC cube specimens (Figure 13b) under uniaxial compression. The stress-strain response of UHP-FRC, with 0.5% volume fraction of PE fibers, under uniaxial compression is shown in Figure 14, and Figure 15 illustrates all of the stress-strain curves of the UHP-FRC OTEC unit cells tested in this experiment, the averages of which are all included in Figure 15d along with the foam G-UHPC cube tested in the first experiment. It should be noted that the 11 mm UHP-FRC OTEC and the foam G-UHPC cube have similar densities.

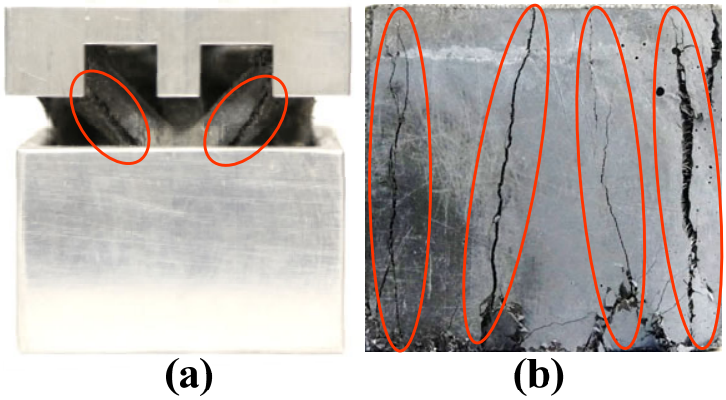

Figure 13 - (a) Formation of columnar cracks along the diagonal elements of the UHP-FRC OTEC unit cells and (b) vertical columnar cracks of 50.8-mm solid UHP-FRC cube specimens after testing under uniaxial compression.

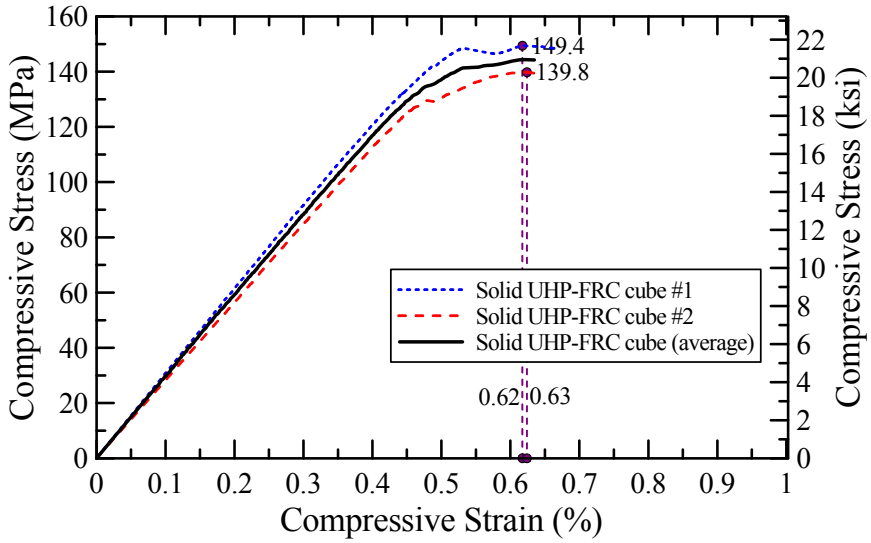

Figure 14 - Stress-strain curve of UHP-FRC with 0.5% volume fraction of PE fibers tested under uniaxial compression in Experiment #4.

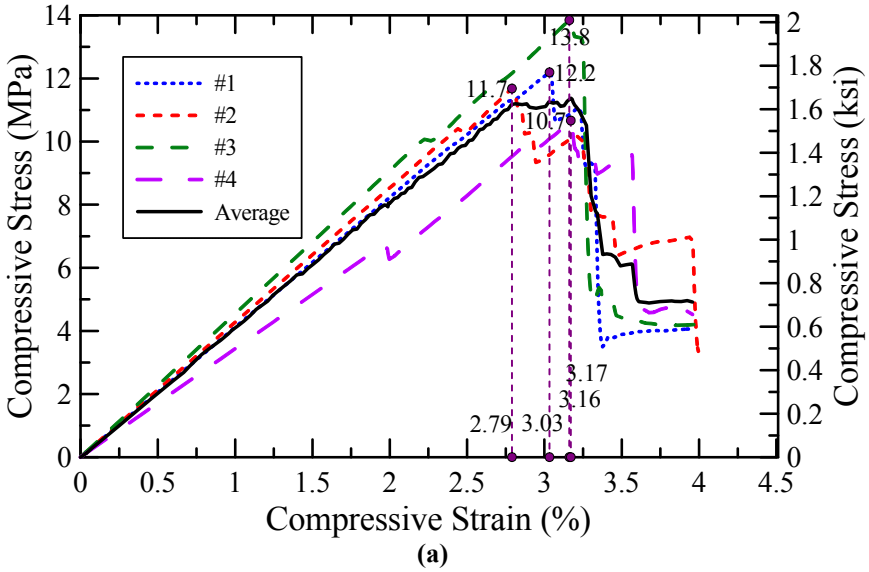
Compressive Stress (MPa)
Compressive Stress (ksi)
Compressive Strain (%)
#1
#2
#3
#4
Average
13.8
12.2
11.7
10.7
3.17
3.16
2.79
3.03

(a)

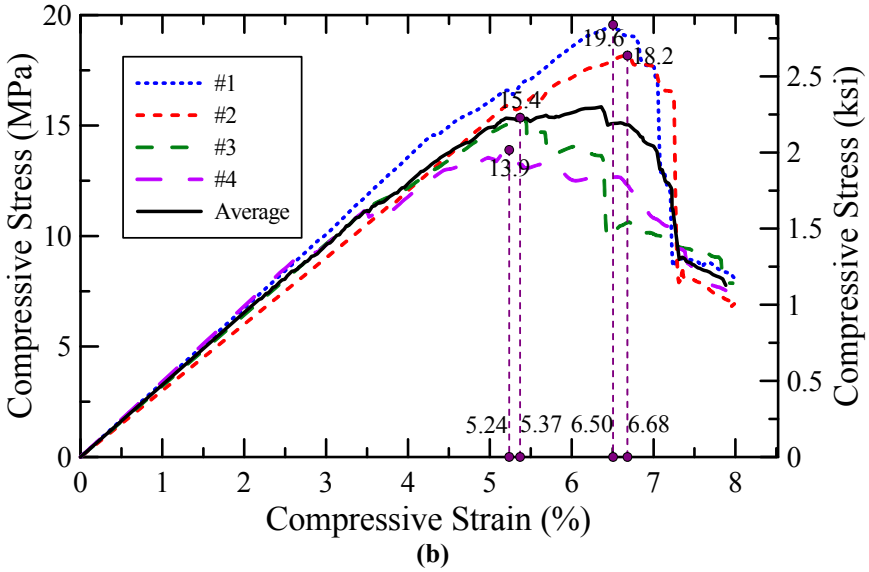
Compressive Stress (MPa)
Compressive Stress (ksi)
Compressive Strain (%)
#1
#2
#3
#4
Average
19.6
18.2
15.4
13.9
5.24
5.37
6.50
6.68

(b)

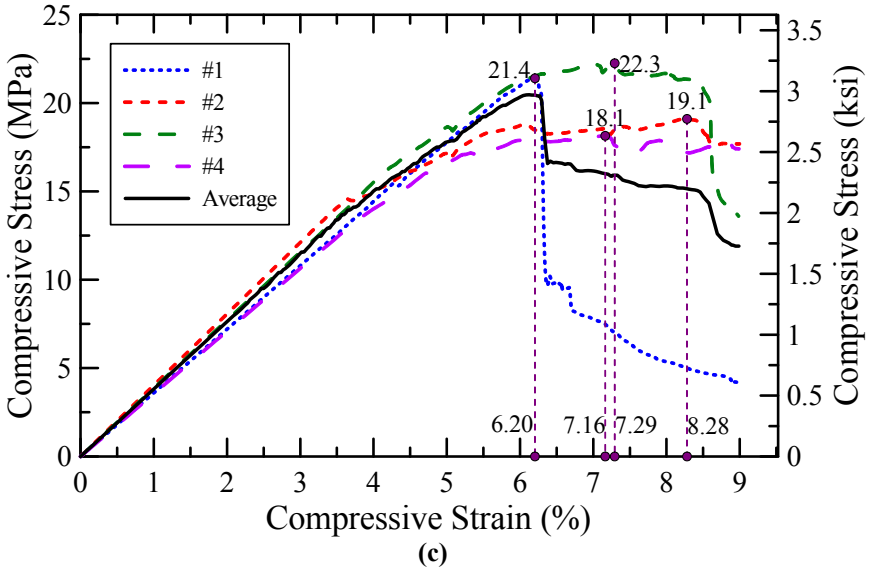
Compressive Stress (MPa)
Compressive Stress (ksi)
Compressive Strain (%)
#1
#2
#3
#4
Average
21.4
22.3
19.1
18.1
6.20
7.16
7.29
8.28

(c)

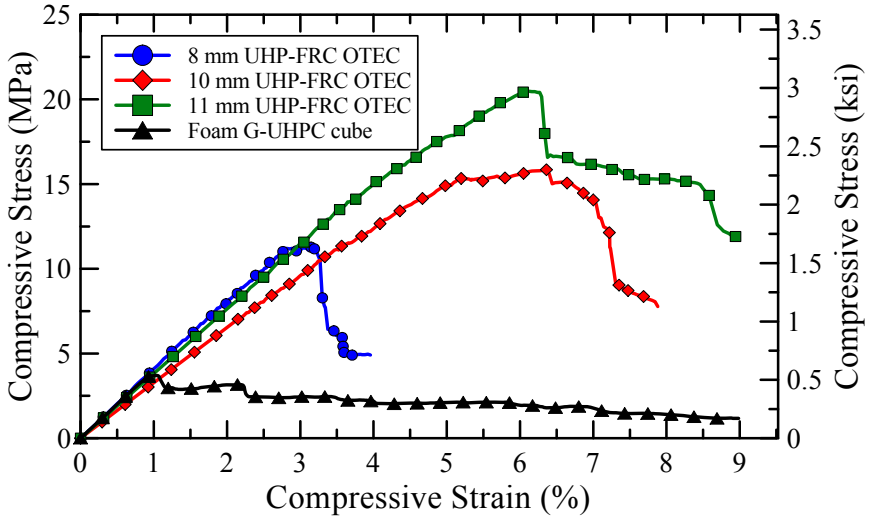

(d)

Figure 15 - Stress-strain curves for (a) 8 mm, (b) 10 mm, (c) 11 mm UHP-FRC OTEC unit cells (d) all OTEC unit cells including the foam G-UHPC cube (Experiment #1), tested under uniaxial compression (Experiment #4) (The foam G-UHPC cube and the 11 mm UHP-FRC OTEC specimens have similar densities).

Although all of the three 8, 10, and 11 mm UHP-FRC OTEC unit cells have a higher porosity (66.4, 53.6, and 47.5%, respectively) compared to the foam G-UHPC cube (45.3% porosity), they all obtained much higher peak loads, strains at peak, and toughness, verifying the efficiency of the UHP-FRC OTEC unit cells in regard to their performance under uniaxial compression.

In the fifth set of experiments, average increases of 63% and 133% in compressive strength were obtained for 10 and 11 mm PLA lattice cells, respectively, compared to the 8 mm PLA lattice cell. The failure of the PLA octet lattice cells was largely dominated by the flexural moments that were induced at the ends of each of the diagonal elements, resulting in double-curvature of these elements. It should be noted that the PLA solid cube did not fail at the end, and the test had to be stopped to avoid any damage to instrumentation. For comparison purposes, however, its load at 45% compressive strain (close to that reached by the 10 and 11 mm PLA lattice cells) was used to calculate its compressive strength.

A summary of the results of the first, fourth, and the fifth experiments is plotted, similar to that of [53], in Figure 16, which shows compressive strength versus density with log-log scaling. As also expressed earlier, what is apparent is that the 8 mm octet lattice cell, for all these three experiments, performs better than would be estimated from a log-log regression based on the strength values of the other specimens with lower porosities (*i.e.* the 10 and 11 mm lattice cells and the 50.8-mm solid cube). A similar claim could also be made for the 10 mm octet lattice compared to the 11 mm (or 12 mm) lattice cell and the solid cube. This effect is attributed to two factors: 1) the smaller the strut or element diameter, the less material is used per unit of lattice cell volume, resulting in a lower probability of containing defects above a certain size which would weaken the lattice elements, and 2) an octet lattice cell with more slender elements (8 mm compared to 10 and 11 mm lattice cells) is presumably more stretching-dominated, and hence, experiences much less shear and flexural moments at the nodes.

Table 8 summarizes the estimated compressive strengths for all of the specimens based on a log-log regression using the last three data points (the 10 mm, 11 mm [or 12 mm] lattice cells, and

solid cubes). As the errors in Table 8 show, this regression considerably underestimates the compressive strengths of the 8 mm octet lattice cells. It is also worth noting that these errors are much smaller for the PLA lattice cells and solid cube (Experiment #5): this difference is expected, since 3D-printing PLA will have presumably resulted in lower defect densities in the components produced than the casting of the G-UHP-FRC and UHP-FRC OTEC unit cell specimens.

Furthermore, according to Figure 16, it is noted that PLA octet lattice unit cells are able to achieve comparable compressive strengths to those of UHP-FRC OTEC unit cells while having a lower density. However, stiffness of PLA octet lattice unit cells (not reported here) is much less than that of UHP-FRC OTEC unit cells.

Table 8 - Estimated compressive strengths based on a log-log regression according to the data points corresponding to the 10 and 11 mm (or 12 mm) lattice cells and solid cubes.

Experiment #	Specimen	Density (kg/m^3)	Compressive Strength (MPa)	Estimated Strength* (MPa)	Error (%)
1	8 mm G-UHP-FRC OTEC	769	7.1	3.0	-57.2
	10 mm G-UHP-FRC OTEC	1,063	10.2	9.1	-10.8
	12 mm G-UHP-FRC OTEC	1,330	16.6	19.4	17.0
	Solid G-UHP-FRC cube	2,290	128.3	122.2	-4.8
4	8 mm UHP-FRC OTEC	763	12.1	6.1	-49.9
	10 mm UHP-FRC OTEC	1,053	16.7	15.4	-7.7
	11 mm UHP-FRC OTEC	1,192	21.4	22.1	3.2
	Solid UHP-FRC cube	2,270	144.6	142.7	-1.3
5	8 mm PLA lattice cell	356	5.7	3.8	-32.8
	10 mm PLA lattice cell	492	9.3	9.4	0.7
	11 mm PLA lattice cell	556	13.3	13.1	-1.3
	Solid PLA cube	1,060	78.2	78.2	-0.1

* Based on a log-log regression using the last three data points

The suggestion that higher void fractions in OTEC lattices give higher specific strengths is further explored in Figure 17, where relative density is plotted against normalized compressive strength. Here, the performances of different octet lattice cells as well as the foam G-UHPC and solid cube specimens, tested in Experiments #1, #4, and #5, are compared with the limit of stretching-dominated as well as bending-dominated ideal behaviors.

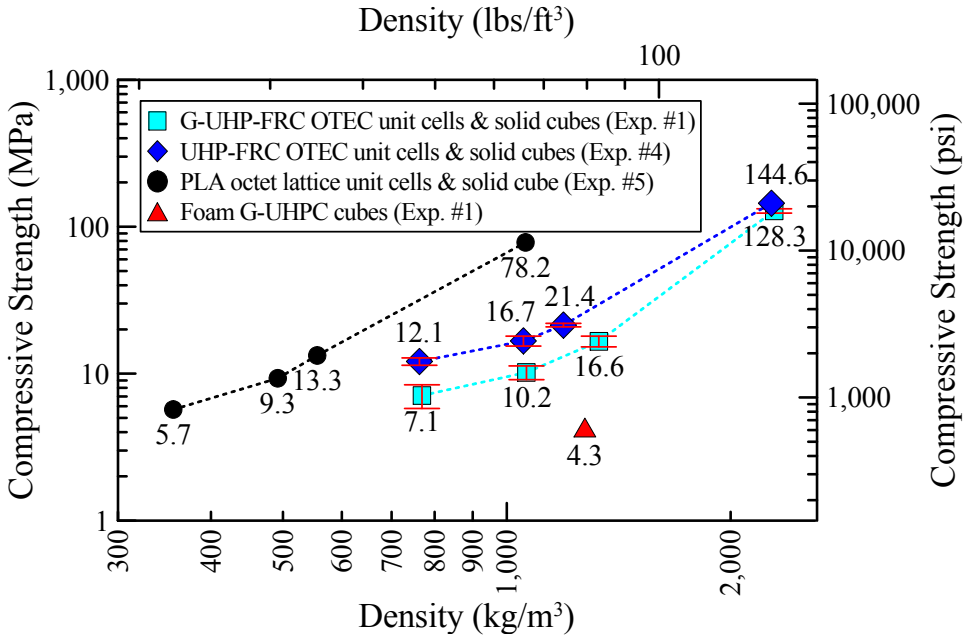

Figure 16 - Compressive strength versus density for octet lattice unit cells and foam G-UHPC and solid G-UHP-FRC and UHP-FRC cubes tested under Experiments #1, #4, and #5.

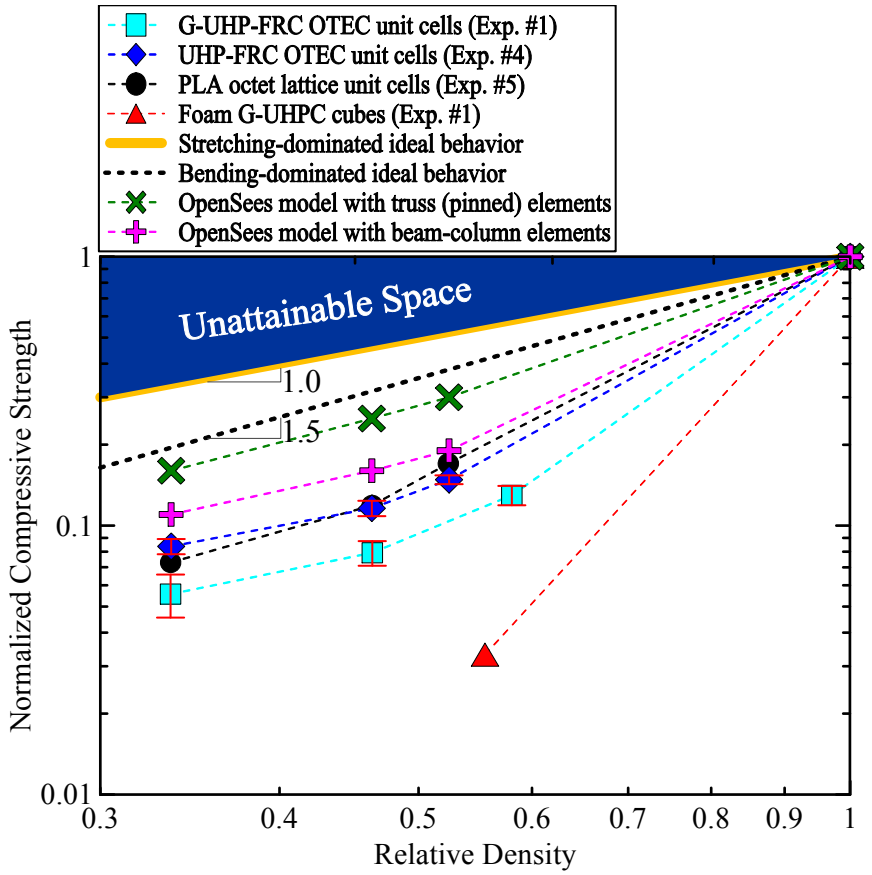

Figure 17 - Normalized compressive strength versus porosity for octet lattice cells and foam G-UHPC concrete tested under Experiments #1, #4, and #5 compared to the ideal behavior.

The stretching-dominated ideal limit, with a logarithmic slope of 1.0 [26], interpolates between the extreme cases of 100% of the potential compressive strength obtained at 0% porosity (this is the case for 50.8-mm solid G-UHPC, G-UHP-FRC, UHP-FRC, and PLA cubes) and zero strength at 100% porosity (as with air). The bending-dominated ideal behavior has a theoretical logarithmic slope of 1.5 [26]. It is apparent that all OTEC unit cells diverge less from the ideal behavior than foam G-UHPC cubes, and among the octet lattice cells, the 8 mm design, as expected, deviates the least from ideal behavior. In addition, by comparing the plots for the PLA octet lattice unit cells with those of UHP-FRC OTEC unit cells, a very similar normalized performance trend is noticed for the two types of materials, which is not only an indication of the validity of the tests and reproducibility of the results for different materials, but more importantly is an indication of an expected normalized performance for the UHP-FRC OTEC unit cells similar to that of a polymeric material with a higher certainty of having no surface or internal void defects.

According to Figure 17, it is observed that the first OpenSees [52] model with pinned truss elements, thus only allowing for axial forces in the elements, results in a linear behavior just below the bending-dominated ideal behavior. Therefore, even with a defect-free model under pure axial compressive forces, for brittle materials, it is not possible to reach any of the ideal behaviors. Using beam-column elements in the second OpenSees [52] model allowed for the development of bending moments in the elements. This leads to a behavior that results from both stretching and bending. The stretching effect, however, is more pronounced as the elements become more slender. This is observed for both the second model as well as the experiments (Experiments #5 and #6) for the 8 mm octet lattice cell since its behavior deviates from the trend of other designs with less slender elements and towards the behavior of the first model with pinned truss elements. In general, very comparable trend and normalized compressive strength values were calculated for the 8, 10, and 11 mm UHP-FRC OTEC unit cells using beam-column elements, by considering the effects of bending moments, in OpenSees [52], which again gives validity to the experimental tests.

3.3.2 Flexural tests

3.3.2.1 Four-point bending tests of G-UHP-FRC 5×1×1-cell OTEC and solid UHP-FRC and conventional concrete flexural beam specimens

In addition to OTEC unit cells tested under uniaxial compression, four G-UHP-FRC 5×1×1-cell OTEC flexural material specimens with 8 mm-thick flanges on both sides and 8 mm-diameter elements were cast using 3D-printed ABS molds. One of these specimens is illustrated in Figure 11b. The specimens were then tested under four-point bending in order to characterize their flexural behavior. Figure 18 illustrates the test setup and its dimensions. One of the four G-UHP-FRC specimens was cured at room temperature and humidity while the rest of the specimens were cured in the fog room (with more than 95% relative humidity at room temperature) until a day before testing. For comparison purposes, two solid UHP-FRC (Table 6) control specimens were also made, one with the same dimensions (50.8 mm×50.8 mm×222.0 mm) and one with the same mass (26.7 mm×50.8 mm×222.0 mm) as those of the G-UHP-FRC 5×1×1-cell OTEC flexural material specimens. To add to this comparison, another solid control specimen (50.8 mm×50.8 mm×222.0 mm) was cast using conventional concrete (Table 6). All control specimens were also cured in the fog room until a day before testing.

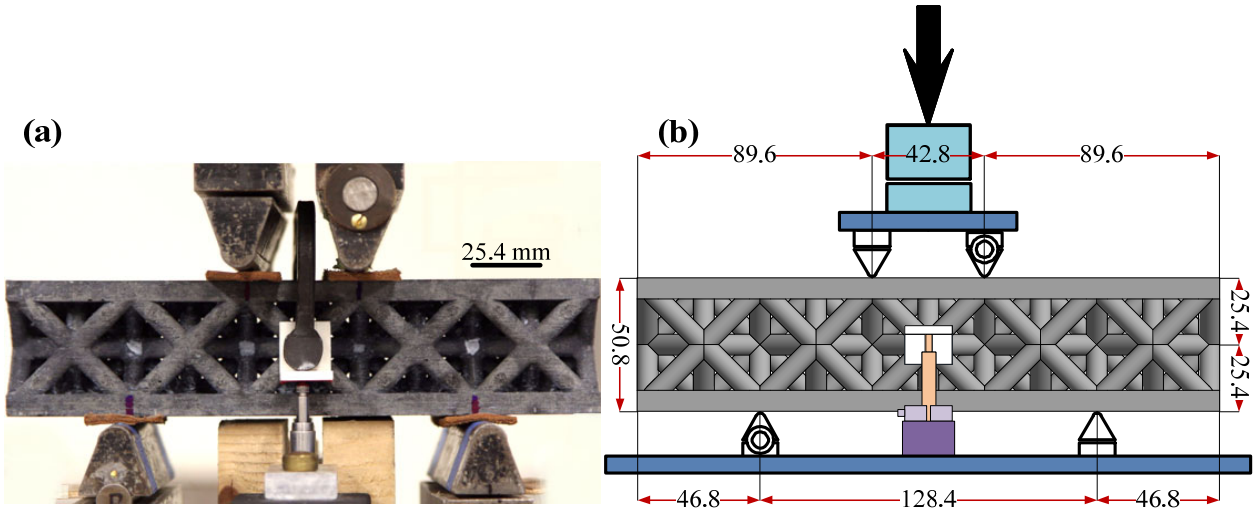

Figure 18 - (a) Actual and (b) schematic design of the four-point bending test setup of G-UHP-FRC 5×1×1-cell OTEC flexural beams (As illustrated in the photo, a C-clamp was used to attach a 3D-printed PLA angle to the middle node on both sides of the beam to allow for deflection measurements using a linear variable differential transformer [LVDT]).

The load-deflection curves of the three G-UHP-FRC 5×1×1-cell OTEC flexural material specimens under four-point bending are illustrated in Figure 19. For all these three specimens, the failure mode was primarily dominated by flexure (compared to shear as another possible failure mode often observed for flexural specimens with small span-to-depth ratios). Higher peak loads (an average increase of 97%), initial stiffness, and flexural toughness were recorded for the two specimens that were cured in the fog room (with more than 95% relative humidity at room temperature) compared to the one cured at room temperature and humidity. This effect is compatible with the results of the 8 mm UHP-FRC OTEC unit cells, cured using three different methods and tested under uniaxial compression in the third set of experiments (Figure 12), presented in Section 3.3.1.

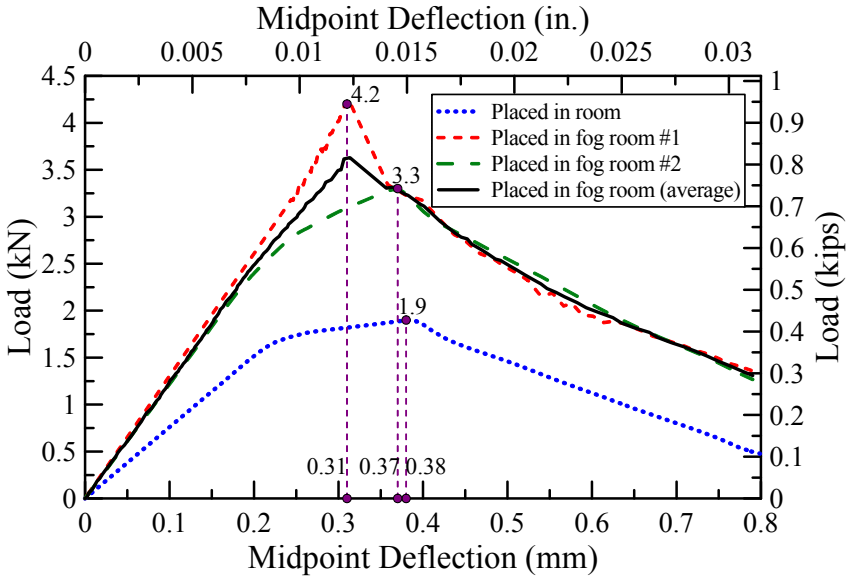

Figure 19 - Load-deflection curves of G-UHP-FRC 5×1×1-cell OTEC flexural material specimens under four-point bending at 28 days after casting.

In Figure 20, the load-deflection curves of G-UHP-FRC 5×1×1-cell OTEC flexural material specimens are plotted on the same graph as the load-deflection curves for the control specimens, including the solid conventional concrete flexural specimen (Table 6) with the same external volume; the solid UHP-FRC flexural specimen with the same external volume; and the solid UHP-FRC flexural specimen with the same mass. The fourth G-UHP-FRC 5×1×1-cell OTEC flexural material specimen performed slightly better than the average of the two specimens that were cured in the fog room, due to some minor changes in the mix design and also its older age. The peak load, midpoint deflection at peak, as well as flexural toughness (area under the load-deflection curves) values are also summarized in Table 9. It is observed that the G-UHP-FRC OTEC flexural specimens were able to achieve up to 65 and 71% of the flexural toughness of the solid UHP-FRC flexural specimen with the same volume, while only having a mass of about 53% of that of this solid specimen. An increase in flexural toughness of about 254 and 283% were achieved for the G-UHP-FRC OTEC flexural specimens as compared to the solid UHP-FRC flexural specimen with the same mass. Similarly, the G-UHP-FRC OTEC flexural specimens obtained an increase in flexural toughness of about 85 and 100% as compared to the solid conventional concrete flexural specimen (Table 6) with the same volume, while also reaching 73 and 94% of its peak load under flexure. These results suffice to illustrate the excellent performance of the G-UHP-FRC OTEC specimens under flexure.

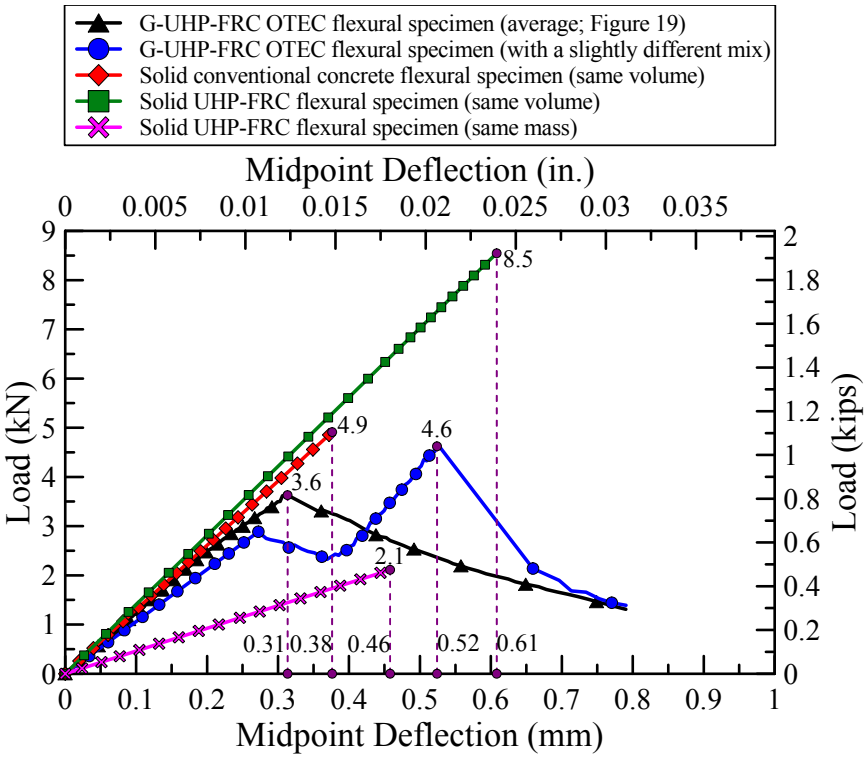

Figure 20 - Load-deflection curves of G-UHP-FRC 5×1×1-cell OTEC flexural material specimens compared with solid flexural control specimens (with either the same external volume [not the same material volume] or the same mass as those of the OTEC flexural specimens) under four-point bending at 28 days after casting.

Table 9 - Peak load, midpoint deflection at peak, and flexural toughness values for the flexural specimens of Figure 20 under four-point bending at 28 days after casting.

Flexural specimen	Dimensions (mm^3)	Mass (g)	Peak load (kN)	Midpoint deflection at peak (mm)	Flexural toughness (kN-mm)	Compressive strength (MPa)
G-UHP-FRC OTEC (average)	50.8×50.8×222.0	665.3	3.6	0.31	1.70	128.3*
G-UHP-FRC OTEC†	50.8×50.8×222.0	664.3	4.6	0.52	1.84	122.7*
Solid conventional concrete (same vol.)‡″	50.8×50.8×222.0	1,207.1	4.9	0.38	0.92	36.5′
Solid UHP-FRC (same vol.)″	50.8×50.8×222.0	1,262.8	8.5	0.61	2.60	143.5′
Solid UHP-FRC (same mass)‴	26.7×50.8×222.0	660.7	2.1	0.46	0.48	143.5′

* Refer to Table 7
† G-UHP-FRC with a slightly different mix design compared to that of Experiment #1, tested after 181 days
‡ Refer to Table 6
′ Average of three samples
″ This specimen had the same external volume (not the same material volume) as those of the OTEC flexural specimens for comparison purposes
‴ This specimen had the same mass as those of the OTEC flexural specimens for comparison purposes

It should be mentioned that most of the results presented so far in this chapter have been published in [2].

3.3.2.2 Four-point bending tests of PLA octet-lattice-reinforced Ultra-High Performance Concrete (UHPC)

To examine the effects of polylactic acid (PLA) lattice-reinforcements on the flexural properties of concrete (stiffness, strength, and flexural toughness), 3D-printed PLA octet-lattices with a volumetric ratio of 33.7%, shown in Figure 21a, were infiltrated by Ultra-High Performance Concrete (UHPC with the same mix design as UHP-FRC in Table 6, but without fibers). These lattices were infiltrated by UHPC with different volume percentages of 100% (i.e. fully infiltrated), 75%, and 37.5% (75% and 37.5% partial infiltrations were evenly distributed on both sides of the lattices to create a double-skin structure as shown in Figure 23) to make three 76.2 mm×76.2 mm×279.4 mm prisms for four-point bending according to ASTM C78 [39]. The two PLA octet-lattice reinforced UHPC specimens with 75% and 37.5% infiltrations were of special interest since they result in an air gap in the center, as illustrated in Figure 23, which provides thermal insultation when such structures are used in façade and flooring systems. These two PLA octet-lattice reinforced UHPC specimens with 75% and 37.5% infiltrations were made in two steps. In the first step, 76.2 mm×76.2 mm×279.4 mm molds were filled with a predetermined amount of UHPC material to reach half of the infiltration percentage on one side of the PLA octet-lattice after submerging it into the UHPC matrix in the mold. The second step included the same procedure however, on the other side of the lattice after one day, when the first flange had sufficiently hardened. These two steps were done on top of a vibrating table to ensure proper infiltration and avoidance of air void formations. The PLA octet-lattice reinforced UHPC with 100% infiltration (or fully-infiltrated) was produced in one step by simply placing the PLA octet-lattice in a 76.2 mm×76.2 mm×279.4 mm mold and infiltrating it with UHPC. High flowability of the UHPC matrix allowed for this process to be accomplished without any difficulties. For comparison purposes, two plain 3D-printed PLA octet-lattices (0.0% infiltration with UHPC) as well as one plain UHPC, one plain conventional concrete (Table 6), and one UHP-FRC (Table 6) 4×1×1-cell OTEC beam (different from those in Section 3.3.2.1) all with the same dimensions (76.2 mm×76.2

mm×279.4 mm) were also tested under four-point bending after 7 days of curing in the fog room. The 4×1×1-cell OTEC beam was made by infiltrating a 3D-printed ABS mold that was later dissolved away in acetone.

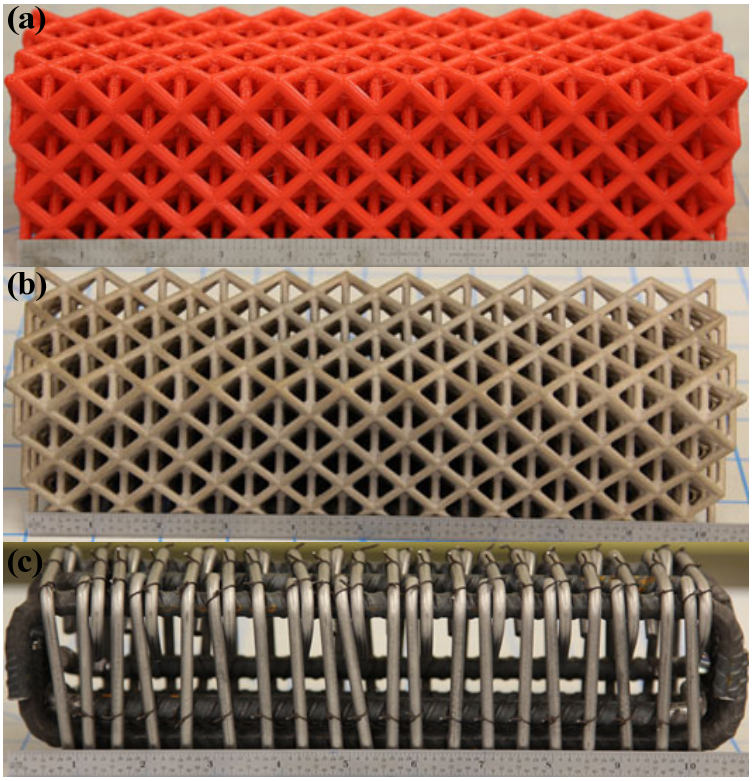

Figure 21 - (a) Plain 3D-printed PLA octet-lattice, (b) Plain 3D-printed stainless octet-lattice, and (c) conventional longitudinal and transverse reinforcement.

The load-deflection curves of the three 3D-printed PLA octet-lattice reinforced UHPC prisms, with volumetric infiltration percentages of 100%, 75%, and 37.5%, under four-point bending are illustrated in Figure 22a and Figure 22b up to a midpoint deflection of 1.5 mm and up to failure, respectively. Both figures include the results of plain 3D-printed PLA octet-lattices (0.0% infiltration) for comparison. In addition, Figure 22a plots the response of three control flexural material specimens, namely, plain UHPC, plain conventional concrete, and a UHP-FRC 4×1×1-cell OTEC beam for comparison purposes. As mentioned before, all of these flexural specimens tested here have the same volumetric dimensions of 76.2 mm×76.2 mm×279.4 mm. The peak load and its corresponding midpoint deflection as well as modulus of rupture for all flexural specimens tested in this experiment are summarized in Table 10. The primary failure mode for all prisms was controlled by flexure, as observed from Figure 23. By comparing the response of plain PLA octet-lattices (0.0% infiltration) with PLA octet-lattice reinforced UHPC with 75% and 37.5% infiltrations, it is noted that by infiltrating the PLA lattices on both sides with UHPC, a stiffer response is gained, however at the expense of the ultimate flexural strength and toughness. This effect is believed to be due to localization of failure in one or a few dominant cracks first forming in the UHPC matrix and shortly after propagating through the depth of the PLA octet-lattice. The final failure however, is characterized as a ductile failure due to post-peak toughening mechanisms as observed from Figure 22b. For the plain PLA octet-lattices (0.0% infiltration) much higher peak loads were recorded (~130%) compared to PLA octet-lattice reinforced UHPC specimens with

75% and 37.5% infiltrations. Although an overall ductile response was recorded for both plain PLA octet-lattices (0.0% infiltration), the final failure was very sudden with almost no post-peak load carrying capacity, as could also be inferred from Figure 22b. By comparing the PLA octet-lattice reinforced UHPC with 100% infiltration (or fully-infiltrated) with other specimens, it is observed that higher stiffness and strength could be achieved when PLA octet-lattices are fully infiltrated with UHPC. However, it is noted that it does lead to lower ductility. This is expected since stiffening and strengthening mechanisms are often at the expense of ductility and toughness.

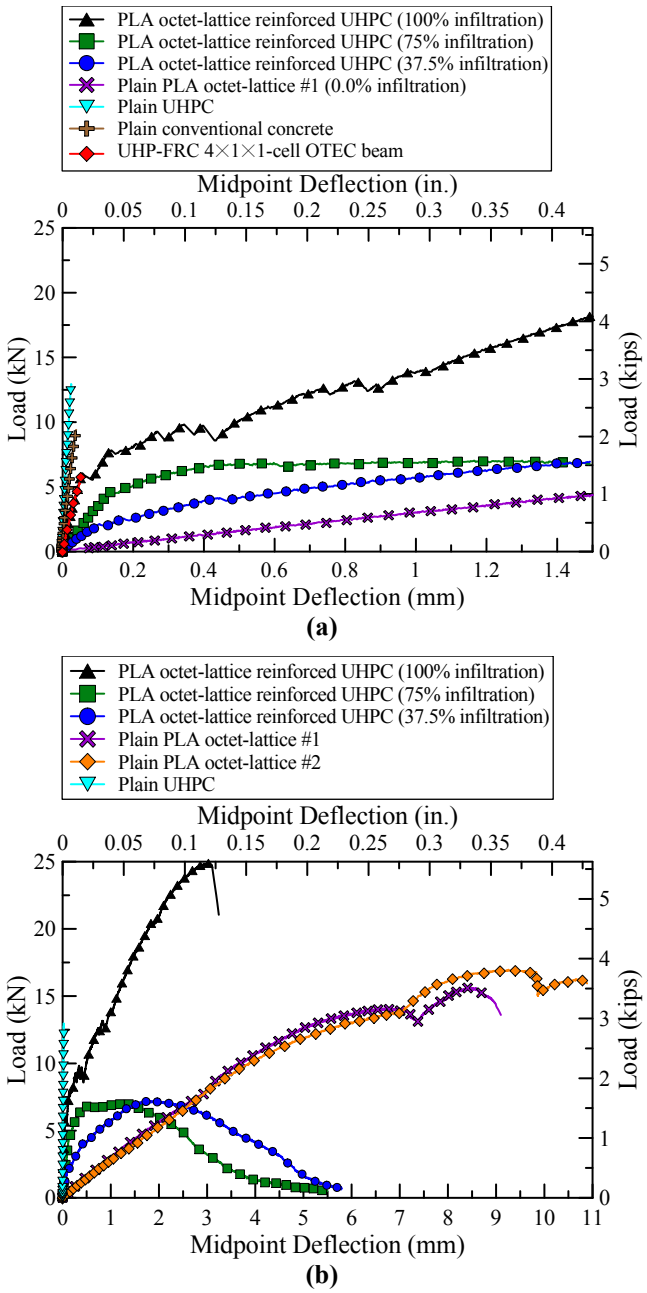

Figure 22 - Load-deflection curves of 3D-printed PLA octet-lattice reinforced UHPC flexural material specimens (a) up to a midpoint deflection of 1.5 mm compared with plain 3D-printed PLA octet-lattices and plain UHPC, plain conventional concrete, and OTEC with the same dimensions and (b) all the way to failure under four-point bending at 7 days after casting.

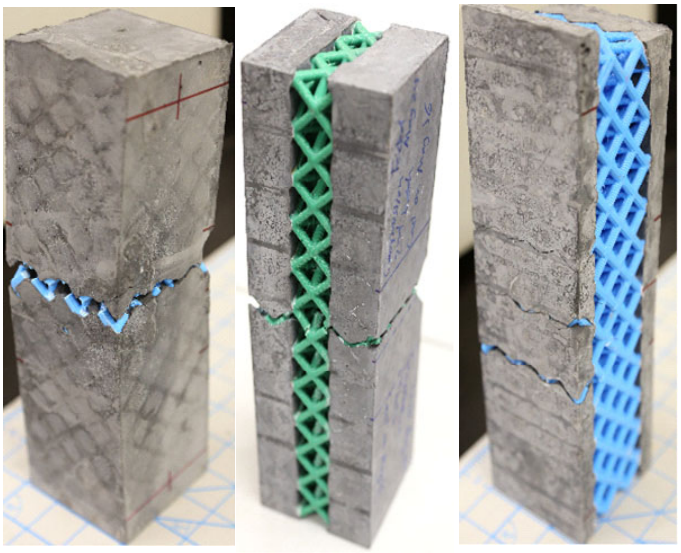

Figure 23 - PLA octet-lattice reinforced UHPC with 100%, 75%, and 37.5% infiltration.

According to Figure 22a, it is interesting to note that the 4×1×1-cell OTEC flexural specimen showed a similar initial branch and stiffness in its response compared to the fully-infiltrated PLA octet-lattice reinforced UHPC (with 100% infiltration), but was not able to achieve higher flexural strength and toughness after first-cracking, which is also not quite comparable to the responses that were recorded for 5×1×1-cell OTEC flexural beams (50.8 mm×50.8 mm×222.0 mm) presented in Section 3.3.2.1. This is due to the fact that the 4×1×1-cell OTEC flexural beam (76.2 mm×76.2 mm×279.4 mm) tested here was slightly scaled up in size, which could have led to a higher probability of containing defects. Therefore, when larger-size OTEC flexural specimens are designed, it may be needed to further reinforce their flanges either with steel rebars or polymer fiber strands in order to achieve the desired response.

Table 10 - Peak load, midpoint deflection at peak, and modulus of rupture values for the flexural specimens under four-point bending after 7 days unless otherwise specified.

Flexural specimen*	Infiltration Percentage (%)	Peak load (kN)	Midpoint deflection at peak (mm)	Modulus of rupture (MPa)
PLA octet-lattice reinforced UHPC	100.0%	24.9	3.03	12.9
PLA octet-lattice reinforced UHPC	75.0%	7.0	1.30	3.6
PLA octet-lattice reinforced UHPC	37.5%	7.2	1.83	3.7
Plain PLA octet-lattice #1	0.0%	15.6	8.51	8.1
Plain PLA octet-lattice #2	0.0%	17.0	9.25	8.8
Plain UHPC	100.0%	13.0	0.02	6.7
Plain conventional concrete	100.0%	9.4	0.04	4.9
OTEC	-	5.9	0.06	3.0
Stainless steel octet-lattice reinforced UHPC†	100.0%	155.5	0.70	80.3
Conventional reinforced UHPC†	100.0%	256.6	1.65	132.6

* All flexural specimens have the same volumetric dimensions of 76.2 mm×76.2 mm×279.4 mm
† Tested later after 113 days

3.3.2.3 Four-point bending tests of stainless steel octet-lattice-reinforced and conventionally reinforced Ultra-High Performance Concrete (UHPC)

In addition to these specimens, it was desired to examine the effects of metallic lattice-reinforcement in UHPC and test whether this new concrete reinforcement approach could possibly lead to more desirable mechanical properties for the composite and instigate new and innovative methods of manufacturing reinforced concrete composites, especially considering the advent of fast-growing additive manufacturing techniques. Therefore, a 3D-printed stainless steel octet-lattice with a volumetric ratio of 19.2%, shown in Figure 21b, was ordered through a 3D-printing company that manufactured the lattice using binder jetting technology onto a powder bed. In this method, the lattice is first 3D-printed using alloy 420 stainless steel, then cured in an oven, sintered, and infiltrated with bronze above 1,100^{o}C, resulting in a matrix material composed of 60% stainless steel and 40% bronze (90% Cu and 10% Sn). This lattice was later fully infiltrated by UHPC to make a 76.2 mm×76.2 mm×279.4 mm prism for four-point bending according to ASTM C78 [39]. For comparison purposes, a conventional steel cage composed of longitudinal and transverse reinforcement, illustrated in Figure 21c, with a similar volumetric reinforcing ratio to that of the lattice (~19.2%) was made and infiltrated by UHPC, which was also tested under four-point bending. As illustrated in Figure 21c, longitudinal tension and compression steel reinforcement consisting of five (in two layers on the bottom) and three (in one layer on top) No. 3 A706 Grade 60 mild steel reinforcing rebars, respectively, were used for reinforcing this specimen, as conventionally done in practice. Both of these specimens were infiltrated on top of a vibrating table for extracting probable air bubbles from the UHPC matrix.

The load-deflection curves of the stainless steel 3D-printed octet-lattice reinforced UHPC and the conventionally reinforced UHPC are illustrated in Figure 24, and peak load, midpoint deflection at peak and modulus of rupture values for these specimens are summarized in Table 10. A very ductile behavior was observed for the conventionally reinforced UHPC, and its final failure was characterized by crushing of UHPC on top, which is preferable over fracture of steel reinforcing bars. The stainless steel octet-lattice reinforced UHPC however, fractured abruptly as also seen in Figure 24. After testing, the fractured surface was studied under a microscope, which revealed cavities and sizable defects in the elements of the stainless steel 3D-printed octet-lattice. These cavities are believed to be due to poor quality sintering and bronze infiltration during the manufacturing process of the lattice. However, a more gradual and smoother plasticity can be observed based on the load-deflection curve for this specimen. This alludes to a more progressive yielding of the octet-lattice elements as compared to yielding-at-once of lumped reinforcement on the top and bottom of the cross section, resulting in a plateau in the response. Based on these results, lattice-reinforcing concrete can possibly lead to new approaches in manufacturing structural elements with more desirable mechanical properties. However, while additive manufacturing techniques are being perfected within the next years, other techniques, such as water-jetting or laser-cutting, could be used to manufacture steel lattices that could then be infiltrated with high-performance concrete composites, like UHPC, UHP-FRC, and G-UHP-FRC.

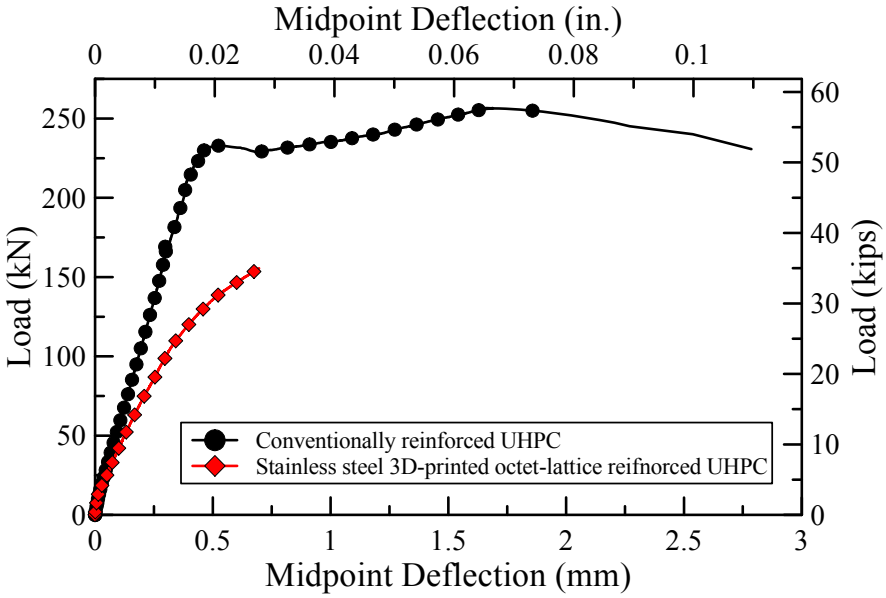

Figure 24 - Load-deflection curves of stainless steel 3D-printed octet-lattice reinforced UHPC and conventionally reinforced UHPC.

3.4 Summary and conclusions

By using G-UHP-FRC and UHP-FRC (Chapter 2), much higher compressive strengths were recorded for OTEC unit cells compared to foam G-UHPC cubes. For example, the compressive strength values of the OTEC unit cell specimens with various element diameters (8, 10, and 11 mm resulting in 66.4, 53.6, and 47.5% porosity, respectively) tested in Experiment #4 considerably exceeded that of the control foam G-UHPC specimens (45.3% porosity) with a geometrically disordered pore structure (by about 180, 290, and 400%, respectively). To summarize, the following conclusions can be drawn from this research:

1. For UHP-FRC OTEC specimens with 8 mm-diameter elements, up to about a 40% increase in compressive strength and a 97% increase in flexural capacity as well as higher stiffness and flexural toughness could be achieved by curing OTEC specimens in a fog room with more than 95% relative humidity at room temperature. This effect is believed to be due to a higher degree of cement hydration as a result of sufficient water permeability into the first few millimeters from any exposed surface of UHP-FRC.
2. Highest average compressive strength of 12.1 MPa was recorded for 8 mm UHP-FRC OTEC unit cells, compared to which an average increase of 38% and 77% was obtained for 10 and 11 mm UHP-FRC OTEC unit cells, respectively. Furthermore, the greater efficiency of the UHP-FRC OTEC unit cells (with 8, 10, and 11 mm-diameter elements resulting in 66.4, 53.6, and 47.5% porosity, respectively), in regard to peak load, strain at peak, and toughness under uniaxial compression was verified compared to that of foam G-UHPC cubes (45.3% porosity).
3. Octet lattice cells with higher porosity, and thus lower density reach compressive strength values that are much closer to the ideal than those attained by specimens with lower porosities. This difference is attributed to two factors: 1) an 8 mm lattice cell uses less material per unit of lattice cell volume compared to 10 and 11 mm lattice cells, leading to a lower probability of containing defects larger than a given size and hence low-strength

components, and 2) an octet lattice cell that uses more slender elements (8 mm compared to 10 and 11 mm lattice cells) undergoes much less shear and flexural moments at the nodes due to a more stretching-dominated mechanism.

4. A similar normalized performance trend was observed for both PLA octet lattice unit cells and UHP-FRC OTEC unit cells tested under uniaxial compression, testifying to the reproducibility of the results for different materials as well as creating confidence in the normalized results recorded for the UHP-FRC OTEC unit cells similar to that of a polymeric material with a higher certainty of having no surface or internal void defects.
5. By modeling the UHP-FRC OTEC unit cells in OpenSees [52], it was observed that even with a defect-free model for brittle materials under pure axial compressive forces, using pinned truss elements, it is impossible to reach any of the ideal behaviors. Using beam-column elements in the model, however, allows for the development of bending moments in the elements, which results in a behavior due to both stretching and bending. The stretching effect, however, is more prominent as the elements become more slender. This was observed for the 8 mm octet lattice cell (with the most slender elements) for both the second OpenSees [52] model, using beam-column elements, as well as the experiments (Experiments #5 and #6).
6. Up to 71 and 100% of the flexural toughness of the solid UHP-FRC and conventional concrete flexural specimens, respectively, was achieved with the G-UHP-FRC OTEC flexural specimen with the same volume while also reaching 94% of the peak load of the solid conventional concrete specimen under flexure, only having a mass of about 53–55% of that of these solid specimens. Such UHP-FRC and G-UHP-FRC OTEC structures encased between skins would entrap air and potentially provide excellent thermal insulation.
7. A stiffer and more ductile flexural response was recorded for PLA octet-lattice reinforced UHPC with 75% and 37.5% infiltrations compared to plain PLA octet-lattices, however, at the expense of the peak flexural strength and toughness (56–57% reduction in flexural strength). This was attributed to the localization of failure in one or a few macro cracks, propagating through the depth of the PLA octet-lattice. The fully-infiltrated PLA octet-lattice (100% infiltration), however, achieved higher stiffness and strength (53% increase in flexural strength), but lower ductility compared to plain PLA octet-lattices. Lattice-reinforcing UHPC could potentially lead to new manufacturing techniques to design and construct structural elements with more desirable mechanical and functional properties.

Based on these results, utilizing G-UHP-FRC and UHP-FRC OTECs (such as 50.8-mm side-length OTEC cells with 8 mm-diameter elements [porosity of 66.4%] as studied extensively in this research), is recommended for lightweight façade and flooring systems. The application of OTECs and lattice-reinforced UHPC could very well be extended to load-bearing structural systems, such as space trusses, concrete shells, shear walls, and the like, which will be investigated in the future.

Chapter 4

Influence of Steel Reinforcing Bar up to Fracture on Tension-Stiffening Behavior of Green Ultra-High Performance Fiber-Reinforced Concrete (G-UHP-FRC)

4.1 Introduction

Excellent mechanical properties of Ultra-High Performance Fiber-Reinforced Concrete (UHP-FRC) composites have generated great enthusiasm in concrete technology and research. During the last decade, an ever-increasing number of researchers have been developing and studying UHP-FRC while its application in the industry has also been significantly escalating as more nations adopt it for retrofitting or rebuilding their infrastructure. Except for a few cases, research on UHP-FRC, however, has predominantly focused on improving its tensile mechanical properties, mainly through achieving high strains under uniaxial tension, far beyond that of steel reinforcing bars at yielding (~0.25–0.35%). Although considerable research has been performed by many researchers in the area of UHP-FRC development, except for a few experiments of large-scale flexural tests of proprietary UHP-FRC specimens, such as in [34,54], literature is void of large-scale tensile testing of UHP-FRC specimens. Many researchers have reported high tensile strength and ductility for UHP-FRC, however, based on small-scale material specimens, which may not be realistic if such composites are to be used for large-scale structural applications.

Large-scale tensile testing of UHP-FRC reinforced with steel rebars, except for a few cases [30–33] as discussed in Chapter 1, has not been more systematically attempted to date to the best of the author's knowledge, and among the existing research, results up to fracture of the steel reinforcing bar are rarely reported. Therefore, large-scale tensile testing of UHP-FRC up to large deformations is necessary, not only for structural design applications, but more importantly to prevent any undesirable premature failure when used in structural members. Most UHP-FRC composites are designed to carry tensile forces up to strains far beyond the yield strain of reinforcing steel. However, high strain capacity does not necessarily ensure ductile behavior when reinforcing bars are used in UHP-FRC. Strain localization followed by early fracture of steel reinforcing bars has been reported based on tension-stiffening experiments of reinforced high-

performance fiber-reinforced cementitious composites (HP-FRCC), such as engineering cementitious composite (ECC) that is known to have a tensile strain capacity of up to 5%, as well as for UHP-FRC, leading to an overall brittle failure [29–33]. So far, no comprehensive solution has been proposed to avoid early fracture of the reinforcing bar in such composites.

According to [29], for example, fracture of steel reinforcing bars embedded in various HP-FRCC materials under uniaxial tension was observed at much lower strain values compared to the bare rebar or even to reinforcing bars embedded in conventional reinforced concrete samples without fibers. For instance, the steel reinforcing bar embedded in ECC was fractured at an average strain value of 3.5% as compared to that of 10.3% for conventional reinforced concrete (with no fibers) with the same steel reinforcing bar ratio. In a prior tension-stiffening experiment [11], where a 101.6 mm×101.6 mm×177.8 mm dogbone-shaped UHP-FRC tension specimen was reinforced with a deformed No. 3 A706 Grade 60 mild steel rebar extending the full length of the specimen (reinforcing ratio of 0.69%), the reinforcing bar was fractured at an overall strain value of 5.8% which is about 3 times smaller than that of the bare rebar. Lack of a uniform strain distribution along the steel reinforcing bar and therefore, early strain-hardening of the rebar within a localized macro crack followed by the unloading of the reinforcement elsewhere are believed to be the main causes of such premature fractures in HP-FRCC and UHP-FRC materials. Therefore, this research investigates more deeply the causes of such failures through a comprehensive study of the tension-stiffening effect of green UHP-FRC (G-UHP-FRC) by testing large-scale dogbone-shaped specimens reinforced with steel reinforcing bars under uniaxial tension.

4.2 Experimental program

G-UHP-FRC and HyFRC materials were evaluated using dogbone-shaped specimens, each reinforced with a single deformed steel bar. Load and axial displacements were measured throughout the experiments up to fracture of the steel reinforcing bar. The reinforcement in two of the G-UHP-FRC specimens were instrumented with post-yield strain gauges to identify initial yielding, strain-hardening, and strain distribution of the steel bar along the gauge length.

4.2.1 Materials

G-UHP-FRC and HyFRC were studied in this chapter, which were made according to [1] and [41], respectively. A summary of the materials characteristics is provided in Chapter 1, Table 1, and the mix proportions for both mixtures are summarized in Table 11.

Table 11 - Primary mixture weight ratios.

Mix	C	FA	GGBFS	CA	FA	S1	S2	SF	W/CM Ratio	HRWR	GP	Fiber*, V_f (%)
HyFRC	1.0	0.0	0.0	1.83	2.02	0.0	0.0	0.0	0.54	0.0	0.0	1.5†
G-UHP-FRC′	0.5	0.25	0.25	0.0	0.0	0.7	0.3	0.25	0.22	0.02	0.25	2.5‡

* % by volume of concrete

† 0.8% SF-1, 0.5% SF-2, 0.2% PVA fibers by volume of concrete

‡ 0.5% SF-3, 0.5% SF-4, and 1.5% SF-5 fibers by volume of concrete

′ G-UHP-FRC: W/CM = 0.22, batch #9 [Table 4], mix #19 [Table 2] in Chapter 2

4.2.1.1 Hybrid Fiber-Reinforced Concrete (HyFRC)

For comparison purposes, HyFRC [41] with 0.8% SF-1, 0.5% SF-2, 0.2% PVA fibers (Table 1) by volume of concrete, and a W/CM ratio of 0.54 was used. A characteristic response of HyFRC under uniaxial tension is illustrated in Figure 25a according to Chapter 2. HyFRC exhibited a compressive strength of 37.2 MPa and a tensile strength of 2.55 MPa with a corresponding strain of 0.32% at peak tensile strength. HyFRC composites exhibit multiple cracking and strain-hardening after first cracking, which are achieved mainly by using a hybrid combination of both PVA microfibers and steel macrofibers with different lengths and aspect ratios to control cracking at microscale and macroscale, respectively. Details on the development and mechanical properties of HyFRC are provided in [41].

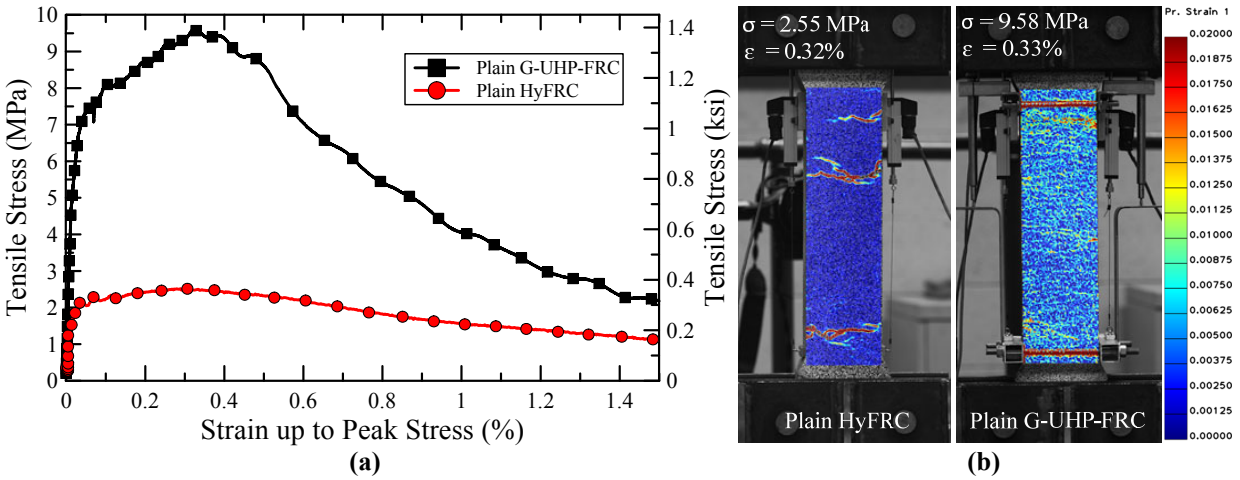

Figure 25 - (a) Uniaxial tensile response of 101.6 mm×101.6 mm×355.6 mm large-scale dogbone-shaped material specimens of HyFRC and G-UHP-FRC based on Chapter 2 and (b) their DIC images at peak stress.

4.2.1.2 Green Ultra-High Performance Fiber-Reinforced Concrete

According to Chapter 2, the G-UHP-FRC mixture used in this research replaces 50% of Portland cement, compared to UHP-FRC mixtures in [11], by 25% fly ash (FA), and 25% ground granulated blast furnace slag (GGBFS). G-UHP-FRC uses a water-to-cementitious materials ratio (W/CM = Water[W]/(C+FA+GGBFS+SF)) of 0.22 with a hybrid combination of micro and macrofibers including 0.5% SF-3 short micro, 0.5% SF-4 long micro, and 1.5% SF-5 hooked-end steel fibers. A maximum compressive strength of about 170 MPa was reported for the G-UHP-FRC mixture according to Chapter 2. Uniaxial tensile response of G-UHP-FRC is also illustrated in Figure 25a according to Chapter 2. A high tensile strength of 9.58 MPa with a corresponding strain of 0.33% at peak tensile strength were observed for G-UHP-FRC tension specimen under uniaxial tension. Same as HyFRC, G-UHP-FRC exhibits multiple cracking, strain-hardening, and post-peak load-carrying capacity by means of fiber hybridization. More detailed information on the development and properties of G-UHP-FRC are presented in Chapter 2.

4.2.2 Test specimens

4.2.2.1 Tension-stiffening specimens

In the tension-stiffening experiments performed by Moreno et al. [29], uniaxial tensile load was applied directly on the reinforcing bar, which extended at both ends of the specimens. In tension-stiffening experiments, if a cracked section is weaker than adjacent uncracked sections, it leads to localized strain concentration in the cracked region, resulting in a strain softening behavior. During softening, while larger deformations occur at the cracked section, elastic deformations of adjacent uncracked sections start to recover. This causes the steel rebar in the uncracked region to experience unloading during softening. Therefore, in this study, the behavior of large-scale dogbone-shaped specimens with embedded steel reinforcing bar was investigated (compared to applying the loads directly on the steel rebar). This allows the embedded steel rebar in the uncracked region to start unloading when a localized macro crack forms, which represents a more realistic and conservative approach.

Eleven G-UHP-FRC and one HyFRC large-scale dogbone-shaped specimens, with a cross section of 101.6 mm×101.6 mm and a gauge length of 355.6 mm, reinforced with a single deformed steel reinforcing bar were tested under uniaxial tension up to fracture of the steel rebar. The tension-stiffening test setup as well as specimen geometry and reinforcing details are illustrated in Figure 26. As shown, the steel rebars, placed in the center of the specimens, were headed on both sides to avoid any slippage and extend the full length of the specimens. In addition, steel mesh and transverse hooks were used, as illustrated in Figure 26, to avoid any undesirable failure outside of the gauge length.

Carreira and Chu [55] showed that the behavior of reinforced concrete in tension is affected by the gauge length, and therefore, they suggested that in order to avoid the effects of primary crack systems and slippage of the reinforcement at the ends of the specimen, the gauge length should be long and far enough from the point of load application (at least one development length). Therefore, longer dogbone-shaped tension specimens with the same cross section of 101.6 mm×101.6 mm with a gauge length of 355.6 mm (twice as long as prior research [11]) were considered for the tension experiments in order to achieve a more realistic composite behavior of G-UHP-FRC and the reinforcing rebar.

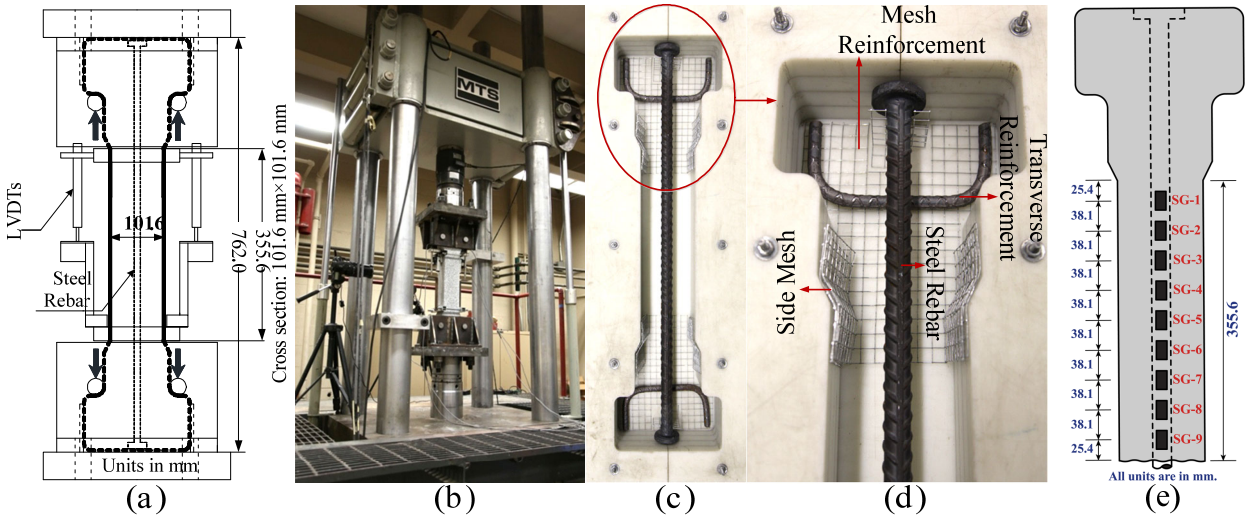

Figure 26 - (a) Schematic and (b) actual design of the tension-stiffening test setup, (c) and (d) reinforcement details of the tension-stiffening specimens, and (e) strain gauge locations for gauged tension-stiffening specimens.

The details of the tension-stiffening specimens are given in Table 12. As for the naming convention of each specimen, for ease of reference, the initial letter(s) represent the concrete material and the first and the second numbers are the rebar No. and rebar grade, respectively. For example, G-5-75 and G-5-S75 stand for G-UHP-FRC reinforced, in the center, with a No. 5 Grade 75 mild steel rebar and a No. 5 Grade 75 stainless steel rebar, respectively. All specimens were cured in the fog room (with more than 95% relative humidity at room temperature) until one day before testing. Two of the G-UHP-FRC specimens (G-5-60 (SG) and G-7-60 (SG) [Table 12]) each had nine strain gauges placed along the length, only on one side, of the embedded steel reinforcing rebar in the gauge length region. The strain gauges were located at 38.1 mm intervals with the end gauges placed 25.4 mm from the ends of the gauge length (355.6 mm) inward, as illustrated in Figure 26.

Table 12 - Tension-stiffening specimens tested under uniaxial tension.

Specimen Name	Material	Rebar No.	Rebar Diameter (mm)	Rebar Type	Rebar Grade	Reinforcing ratio (RR, %)
Hy-5-60	HyFRC	5	15.875	A706	60	1.98
G-4-60	G-UHP-FRC	4	12.7	A706	60	1.27
G-5-60	G-UHP-FRC	5	15.875	A706	60	1.98
G-5-60 (SG)*	G-UHP-FRC	5	15.875	A706	60	1.98
G-5-75	G-UHP-FRC	5	15.875	A615	75	1.98
G-5-S75	G-UHP-FRC	5	15.875	A276	Stainless 75	1.98
G-5-100	G-UHP-FRC	5	15.875	A615	100	1.98
G-6-60	G-UHP-FRC	6	19.05	A706	60	2.83
G-6-75	G-UHP-FRC	6	19.05	A615	75	2.83
G-6-S75	G-UHP-FRC	6	19.05	A276	Stainless 75	2.83
G-7-60	G-UHP-FRC	7	22.225	A706	60	3.90
G-7-60 (SG)*	G-UHP-FRC	7	22.225	A706	60	3.90

* Specimens with 9 strain gauges on the rebar within the gauge length

A706 Grade 60 mild steel rebars No. 4, 5, 6, and 7, leading to reinforcing ratios (RR) of 1.27, 1.98, 2.83, and 3.90%, respectively, were used to investigate the effects of various reinforcing ratios up to about 4% on the tension-stiffening behavior of reinforced G-UHP-FRC. The main objective here was to explore whether the premature failure of tension-stiffening specimens due to early strain localization reported by other researchers (summarized in Chapter 1) could be avoided by increasing the longitudinal reinforcing ratio, leading to an increase in the load taken by the cracked section, forcing other transverse macro cracks to form. Furthermore, it was believed that using a higher reinforcing ratio would lead to a higher possibility of the formation of longitudinal splitting cracks along the gauge length, leading to a more distributed plasticity along the embedded rebar, and hence, a more overall ductile behavior. No. 5 and 6 A615 Grade 75 as well as No. 5 A615 Grade 100 steel rebars were also used to investigate whether an increase in the yield and ultimate tensile strength of the embedded rebar can lead to multiple transverse macro crack formation. Moreover, it was known that A276 Grade 75 stainless steel strain-hardens right after yielding without exhibiting a pronounced yielding plateau and finally, achieving a very high ductility and toughness. This was believed to prevent the exhaustion of fibers bridging the crack, preserving the load-carrying capacity of the matrix, and thus leading to the formation of other transverse cracks. Therefore, No. 5 and 6 A276 Grade 75 stainless steel rebars were used as well to explore if higher ductility and toughness as well as a reduced yielding plateau for such steel reinforcement will allow for the formation of multiple transverse macro cracks, and thus a higher overall ductility for the tension-stiffening specimens.

4.2.2.2 Reinforcing steel rebars

Seven bare steel reinforcing bars, listed in Table 13, were tested to obtain their stress-strain response under uniaxial tension. All except two bare steel rebars used in tension-stiffening specimens, listed in Table 13, were included in these series of uniaxial tensile tests. No. 4 A706 Grade 60 mild and No. 5 A276 Grade 75 stainless steel bare rebars were excluded because the tensile performance of their subsequent larger rebar sizes, namely No. 5 A706 Grade 60 mild and No. 6 A276 Grade 75 stainless steel bare rebars, were of more interest. Similar to the tension-stiffening specimens, the first and the second numbers, used in specimen names, are the rebar No. and rebar grade, respectively.

Table 13 - Steel reinforcing bars tested under tension.

Specimen Name	Rebar No.	Rebar Diameter (mm)	Rebar Type	Rebar Grade
ST-5-60	5	15.875	A706	60
ST-5-75	5	15.875	A615	75
ST-5-100	5	15.875	A615	100
ST-6-60	6	19.05	A706	60
ST-6-75	6	19.05	A615	75
ST-6-S75	6	19.05	A276	Stainless 75
ST-7-60	7	22.225	A706	60

4.2.3 Testing setup, instrumentation, and measurements

The testing setup is shown in Figure 26. The gauge length was 355.6 mm long. All tension-stiffening specimens were tested using a displacement-controlled 1,300-kN universal testing machine under uniaxial tension with a constant displacement rate of 0.508 mm/min. Force was measured by the testing machine, and elongation of the region of interest was measured with linear variable displacement transducers (LVDTs). Two LVDTs were used on each side, with different displacement ranges, to measure elongations as accurately as possible during both elastic and inelastic responses. The average deformation was later divided by the gauge length (355.6 mm) to calculate the average axial strain of the specimen. Strains of the two strain-gauged specimens (Table 12) were measured using post-yield strain gauges placed on one side of the embedded steel rebar. The seven bare steel rebars were tested using a 530-kN universal testing machine. For these tests, an extensometer was used to measure the deformation of the bare reinforcing bars.

4.2.4 Stress distributions and crack formations in reinforced concrete tension members

In this section, a similar approach to [56–58] is implemented for analyzing various stress distributions in cracked reinforced concrete tension members to calculate steel, concrete, and bond stresses as illustrated in Figure 27a.

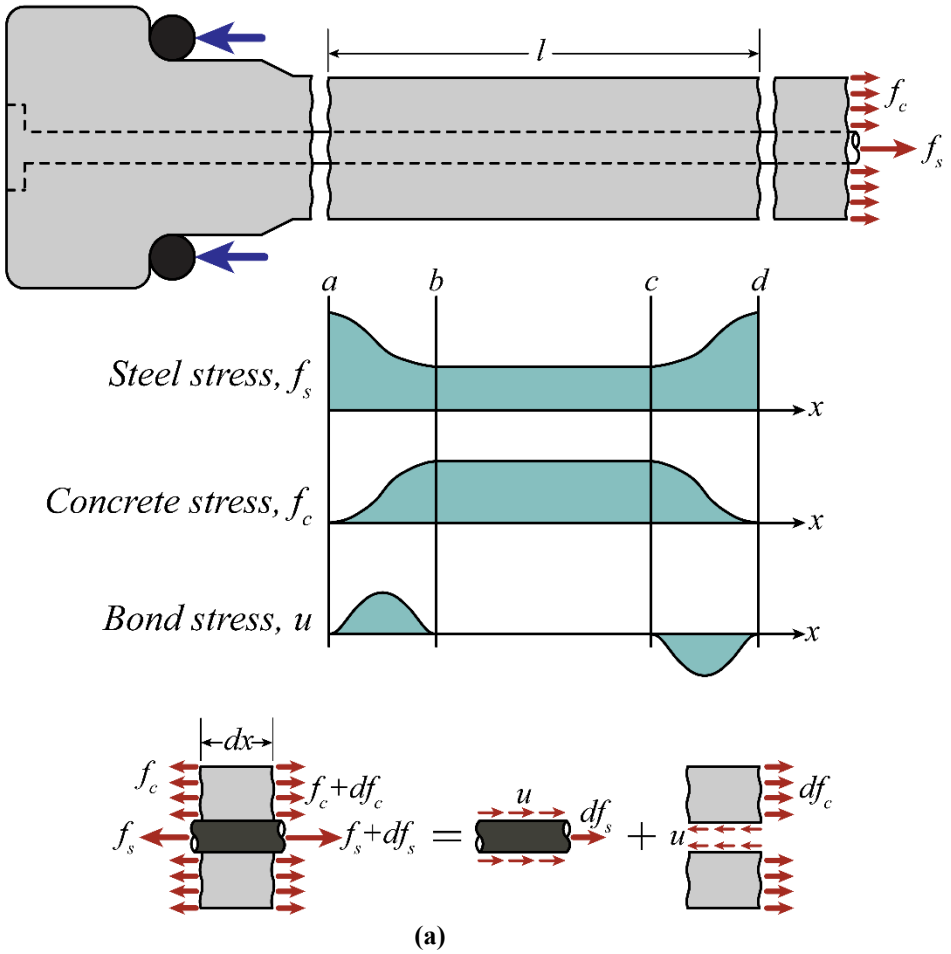

(a)

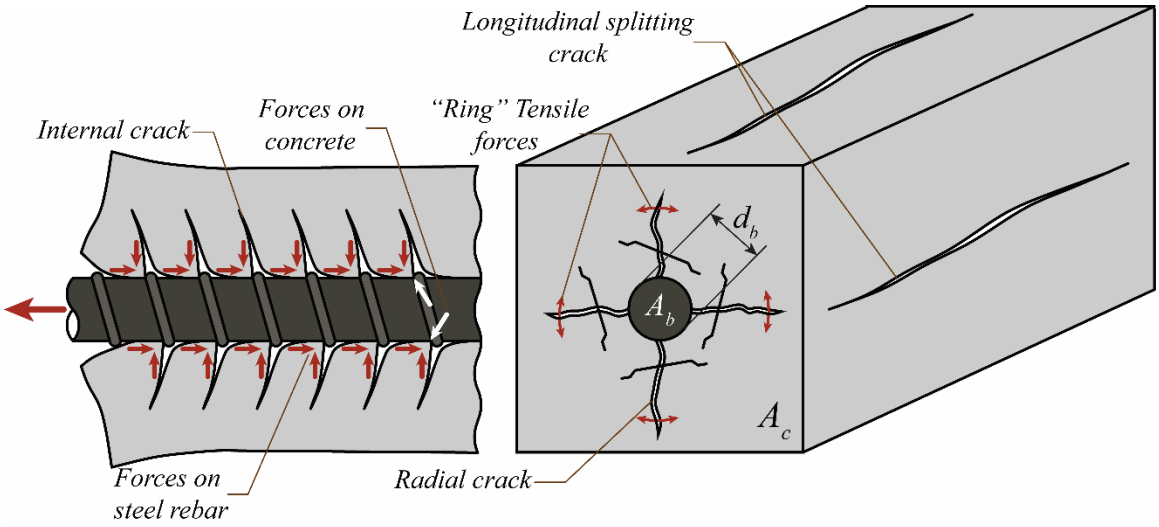

(b)

Figure 27 - (a) Stress distributions and free body digram of a finite segment of tension-stiffening specimens and (b) crack formations in cracked G-UHP-FRC tension-stiffening specimens [56–58].

According to [57], a minimum longitudinal reinforcing ratio is required for tension members as expressed in Eq. (1), which assumes that after cracking, the reinforcing bar should be able to stand the maximum tensile force carried by the concrete cross section. In Eq. (1), A_{st}, A_g, f_t, and f_y are the nominal cross sectional area of steel reinforcement, concrete gross cross sectional area, maximum tensile stress carried by the concrete cross section, and tensile yield stress of steel reinforcement, respectively. A cracked section becomes weaker compared to adjacent uncracked sections if Eq. (1) is not satisfied. This could lead to a brittle failure due to localized strain concentration in the cracked region.

$$\rho_l = \frac{A_{st}}{A_g} > \frac{f_t}{f_y} \tag{1}$$

In Figure 27a, a dogbone-shaped tension member, reinforced with a single deformed steel rebar in the center, is under uniaxial tension. Here, it is assumed that sufficient longitudinal reinforcing ratio is provided to allow for the formation of two macro cracks at sections *a* and *d* at some loading step. It is assumed that the reinforcing steel carries all the tensile force at these cracked sections. In theory, it is deemed reasonable to assume that along a central region *bc*, concrete and steel experience equal strain if the uncracked length *l* is sufficiently long. In this region, steel and concrete share the tensile force, the portion of each could be estimated based on their individual tensile stress-strain response. In regions *ab* and *cd*, steel stress, f_s, is reduced as concrete stress, f_c, is increased. This necessitates the development of bond stresses, *u*, between steel and concrete, which were first observed by Goto [56].

Figure 27a also shows the free body diagram of a segment of the reinforced tension member with length *dx*. By writing force equilibrium for this element, the relation between bond stress, *u*, steel stress, f_s, and concrete stress, f_c, can be derived as expressed in Eq. (2). Therefore, bond stress can be related to steel and concrete stress gradients as expressed in Eq. (3). It is logical then to assume

that there exists no bond stress along the *bc* segment since steel and concrete stresses are constant. This is consistent with the earlier statement that concrete and steel undergo equal and uniform elongation along the *bc* segment due to lack of any slippage between steel and concrete.

$$df_s A_b = -u\pi d_b dx = -df_c A_c \tag{2}$$

$$u = -\frac{df_s}{dx}\frac{A_b}{\pi d_b} = -\frac{df_s}{dx}\frac{d_b}{4} = \frac{df_c}{dx}\frac{A_c}{\pi d_b} \tag{3}$$

Here, A_b, d_b, and A_c represent the nominal area and diameter of the steel reinforcing rebar and the concrete gross cross sectional area, respectively. According to Eq. (3), bond stress can be calculated from either steel or concrete stress gradient. Steel strain distribution can be measured by strain gauges placed on the steel rebar. After obtaining the tensile stress-strain response of the bare steel rebar, it is then possible to determine the steel stress gradient, and thus the bond stress, along the length of the sample. Similarly, concrete strain distribution can be obtained using Digital Image Correlation (DIC) techniques. Therefore, it is also possible to determine the concrete stress gradient, and hence the bond stress, using the corrected tensile stress-strain response of concrete (Figure 36b), discussed later in Section 4.3.3.

Figure 27b shows different possible crack formations in a reinforced concrete tension member. Development of tensile stresses in concrete in the longitudinal direction, caused by rebar ribs due to rebar slippage near the cracked regions, result in the formation of internal cracks, shown in Figure 27b. Development of so called "ring" tensile stresses in concrete in the cross sectional plane lead to development and propagation of radial cracks, which can then propagate along the longitudinal direction resulting in the formation of longitudinal splitting cracks parallel to the length of the rebar, as also illustrated in Figure 27b. These cracks allow for the distribution of plasticity along the embedded steel reinforcing bar and cause the composite behavior between concrete and steel reinforcement to diminish. However, formation of such cracks, in case of large deformations, is deemed necessary to achieve higher average tensile strain, and hence ductility, for tension-stiffening specimens prior to fracture of the steel rebar.

4.2.5 Tension-stiffening effect and bond behavior

Although in this research, the tension-stiffening effect of reinforced conventional concrete was not investigated, it deems necessary to address it for the sake of comparison. Moreno et al. [29] observed loss of tension-stiffening effect in reinforced conventional concrete prior to yielding of the reinforcing bar, which was attributed to early formation of longitudinal splitting cracks along the gauge length parallel to the length of the rebar. This in turn resulted in a spread of plastic deformation along the steel rebar and thus a ductile behavior up to fracture of the reinforcing bar. Initiation and formation of longitudinal splitting cracks, however, is much more difficult in HP-FRCC and (G)UHP-FRC composites compared to conventional concrete. This is due to active confinement provided by fiber-bridging upon initiation of such cracks, leading to a higher bond strength between the cementitious composite and the rebar. Although a greater bond strength could ensure better active confinement and shorter development lengths required in congested regions of structural members, such as beam-column connections, it could negatively impact the overall tensile ductility and thus the flexural performance of such composites. Therefore, more definitive conclusions could be made when tension-stiffening is studied along with bond behavior.

To this end, G-7-60 (with overall ductile behaviors, according to results reported later in Section 4.3.1) was selected to further investigate their ultimate deformation capacity by calculating their concrete and bond stresses at different stages of testing. To conduct this analysis, DIC techniques were used. To this end, specimens were painted to obtain a speckled pattern (shown later in Figure 32) that would then be used to measure deformations and strains based on relative displacements of speckles, using the DIC software, OpteCAL. Using one of the post-processing tools in OpteCAL, it is made possible to introduce virtual strain gauges on any surface with the speckled pattern to measure local deformations and thus principle strains. For G-7-60, nineteen virtual concrete strain gauges in series were used, extending in the center of the front surface the full length of the gauged region. These one dimensional virtual strain gauges were each about 100 pixels long (~17 mm). Using the post-processing tools of OpteCAL, local concrete strain values were measured for each image according to the readings of virtual strain gauges. Then, by using the corrected tensile stress-strain response of G-UHP-FRC, presented later in Figure 36b, concrete stresses were estimated along the gauge length based on the strain values measured in the previous step. By re-writing Eq. (3) in Section 4.2.4 in the form of Eq. (4) for a finite segment of the tension-stiffening specimens, the bond stress for each segment with length $\Delta x \approx 17\ mm$ could be readily estimated.

In addition, G-7-60 (SG) was also further investigated by calculating its steel and bond stresses at different stages of testing. Here, however, based on the strain values measured by the strain gauges on the embedded rebar in G-7-60 (SG), the tensile stress experienced by the steel rebar at the location of each strain gauge could then be estimated, using the tensile response of its bare steel rebar (ST-7-60). The tensile stress gradient in the embedded steel rebar along a finite segment could then be calculated. Therefore, according to Eq. (4), similarly, the bond stress for each segment with length $\Delta x = 38.1\ mm$ could be calculated.

$$u = \frac{\Delta f_c}{\Delta x}\frac{A_c}{\pi d_b} = -\frac{\Delta f_s}{\Delta x}\frac{d_b}{4} \tag{4}$$

4.3 Experimental results and discussions

4.3.1 Tension-stiffening response

4.3.1.1 Initial response up to 1.0% strain

The total tensile load versus average tensile strain for five tension-stiffening specimens (G-5-100, G-6-60, G-6-75, G-6-S75, and G-7-60) as well as their corresponding bare steel rebars (ST-5-100, ST-6-60, ST-6-75, ST-6-S75, ST-7-60) up to 1.0% strain is illustrated in Figure 28. G-5-60 and G-5-75 are not included here since their corresponding bare steel rebar tensile responses were not properly recorded by the extensometer during their elastic regime, probably due to instrument slippage during testing. According to Figure 28, a similar initial performance up to an average specimen strain of about 1.0% is observed for G-5-100, G-6-60, G-6-75, G-6-S75, and G-7-60, and in general, for all reinforced G-UHP-FRC specimens. Tension-stiffening effect before yielding of the reinforcing steel and tension-strengthening after yielding (the ability of the specimen to carry greater loads than the yield strength of the steel rebar), as shown in Figure 28a, were observed for all reinforced G-UHP-FRC specimens. As mentioned earlier, according to [29], the tension-stiffening and tension-strengthening effects were lost in reinforced conventional concrete prior to yielding of the embedded steel rebar due to early formation of longitudinal splitting cracks. Therefore, the considerable tension-stiffening and tension-strengthening effects in reinforced G-

UHP-FRC specimens and their exceptional overall performance up to an average specimen tensile strain of 1.0% may suggest an unwarranted conclusion that the longitudinal steel reinforcing ratio of reinforced G-UHP-FRC specimens could possibly be reduced from a sustainability and economic point of view, by using a steel rebar with a smaller nominal cross sectional area while keeping the concrete dimensions the same. As later discussed in this research, the tension-stiffening and tension-strengthening effects of reinforced G-UHP-FRC, and in general any HP-FRCC materials, should be studied up to fracture of their embedded steel reinforcement in order to avoid any undesirable and unexpected brittle failure, especially when used in structural elements.

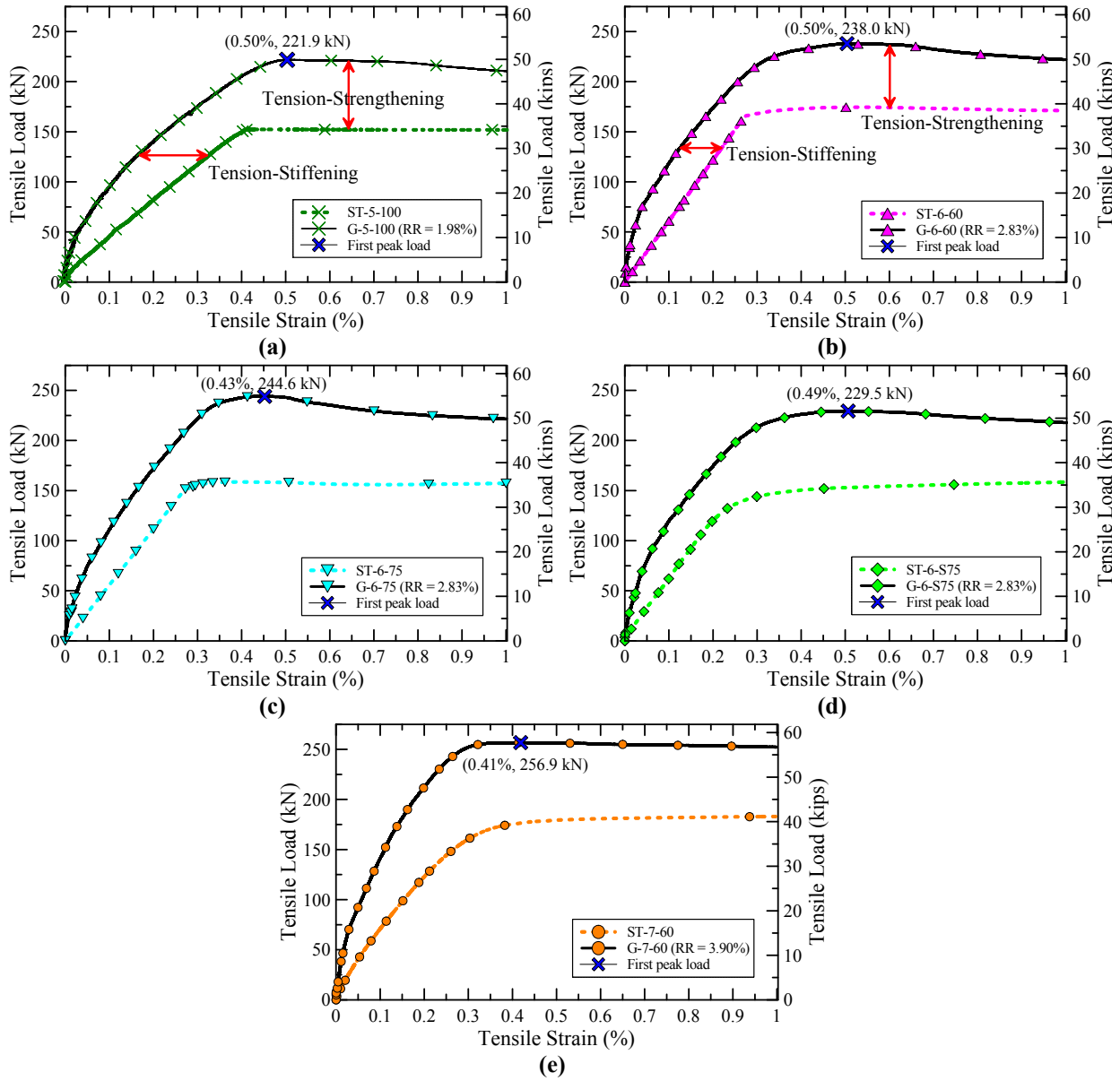

Figure 28 - Total tensile load versus average tensile strain up to 1.0% for (a) G-5-100 and ST-5-100, (b) G-6-60 and ST-6-60, (c) G-6-75 and ST-6-75, (d) G-6-S75 and ST-6-S75, and (e) G-7-60 and ST-7-60 (the blue cross on the load-strain curves corresponds to the first peak load, for which the corresponding tensile strain and load are also displayed on each graph).

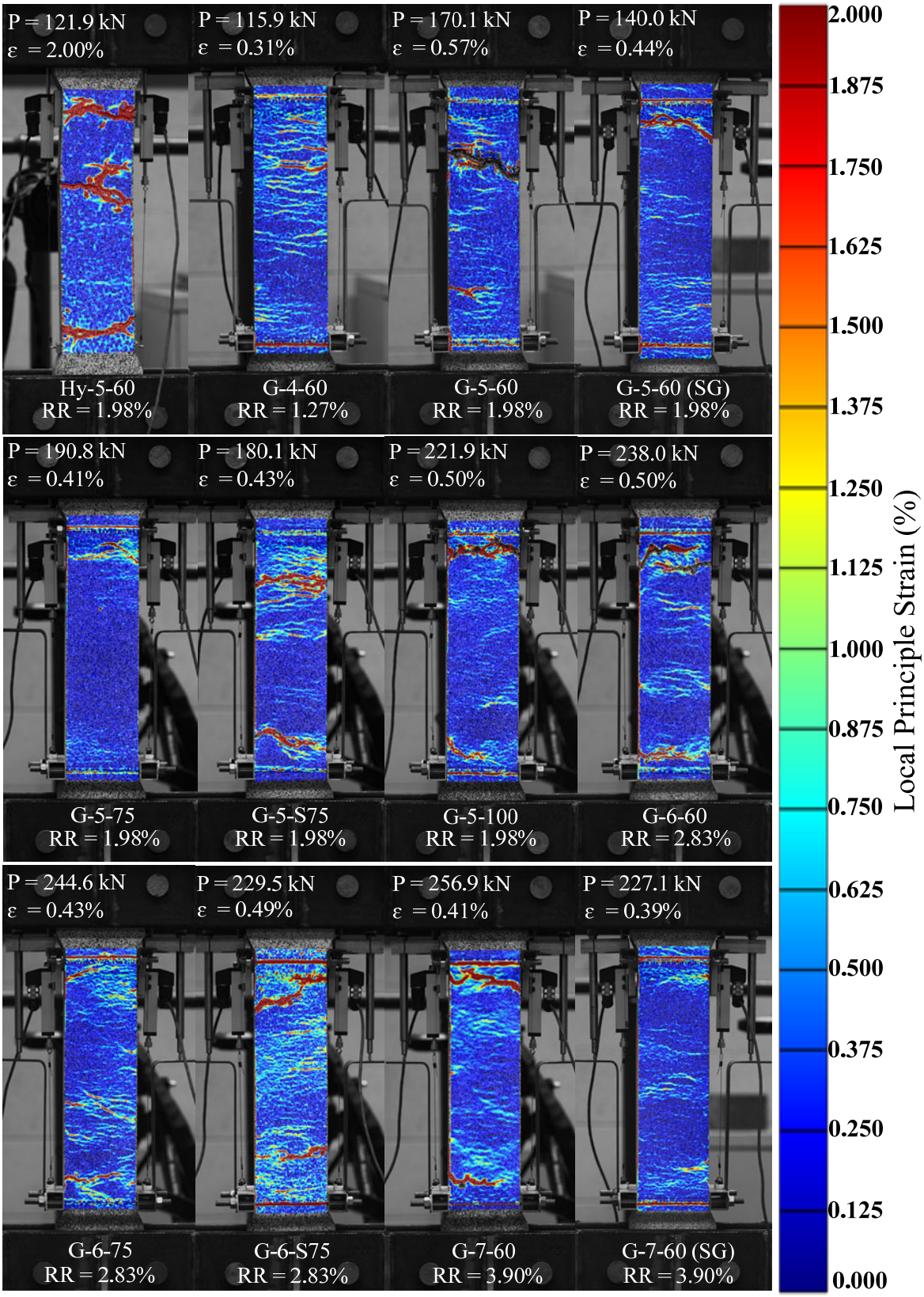

Figure 29 - DIC images of tension-stiffening specimens at first peak load (P is the first peak load and ε is its corresponding average specimen strain).

Figure 29 includes the DIC images of tension-stiffening specimens at first peak load (P). Average tensile specimen strains (ε) as well as longitudinal steel reinforcing ratios (RR) are also shown for each image in Figure 29. Moreover, a color scale is provided to estimate the local principle tensile strains on the surface of each specimen at first peak tensile load. It is believed that G-UHP-FRC and the embedded reinforcing steel carry the applied tensile load in proportion to their modulus of elasticity and area and deform together with somewhat compatible elongations through multiple microcracking of G-UHP-FRC as observed using DIC techniques (Figure 29) until a strain value of about 0.3–0.4% (Figure 28) at which the steel reinforcing bar starts to yield. The rebar yielding leads to a dramatic drop in stiffness of the embedded steel rebar, especially during its yielding plateau. Further deformations start to localize at the weakest section along the gauge length, where later a macro crack is formed, and fiber pullout can be observed. This very quickly results in the first peak load at a strain value of about 0.4–0.5%, as indicated in Figure 28 as well as Figure 29, immediately after which initial softening occurs. In some cases, such as for G-4-60, G-5-75, G-6-75 and G-7-60 (SG) as could be inferred from Figure 29, the first peak load precedes a fully-formed macro crack. It is also noticed that as expected, the first peak load increases as the steel reinforcing ratio is increased. No visible longitudinal splitting cracks were observed for any of the tension-stiffening specimens up to this point (strain of 1.0%). It should be noted that if the section is not sufficiently reinforced, a brittle failure is very likely to follow.

According to Figure 29, it could be observed that Hy-5-60 formed three dominant macro cracks at its first peak load at an average specimen strain of 2.00%. All reinforced G-UHP-FRC specimens, however, had their first peak load earlier at an average tensile strain of less than 0.6% (0.31–0.57%). Based on Figure 29, it is further noticed that most reinforced G-UHP-FRC specimens formed multiple micro cracks, visible as yellow, green, and cyan hairlines on the surface of each specimen, up to the first peak load.

4.3.1.2 Full response under tension up to fracture of the steel rebar

The total tensile load versus average tensile strain for all twelve tension-stiffening specimens in Table 12 is given in Figure 30a and Figure 30b. The tensile response of G-5-S75 and G-6-S75 were plotted separately in Figure 30b because of their much higher ultimate strain capacity. The tensile load-strain curves for the seven bare steel rebar specimens listed in Table 13 are also illustrated in Figure 30c. The tension-stiffening response of some representative specimens are plotted in Figure 31 on the same graphs with their corresponding bare steel rebar response for comparison purposes. The tension-stiffening as well as the bare steel reinforcing bar tensile test results are all summarized in Table 14 and Table 15, respectively.

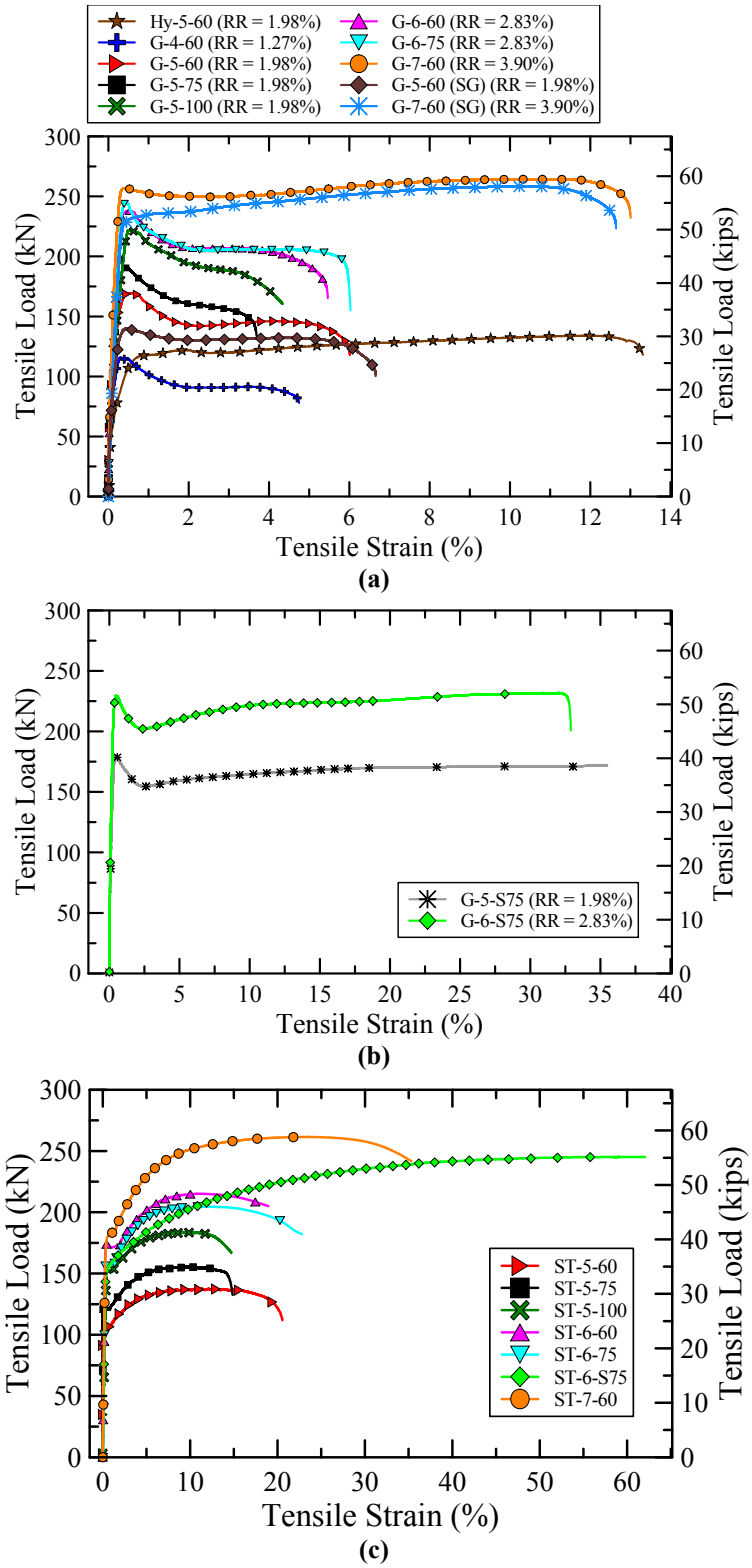

Figure 30 - Total tensile load versus average tensile strain up to fracture of the steel rebar for (a) Hy-5-60, G-4-60, G-5-60, G-5-75, G-5-100, G-6-60, G-6-75, G-7-60, G-5-60 (SG), and G-7-60 (SG) and (b) G-5-S75 and G-6-S75, and (c) ST-5-60, ST-5-75, ST-5-100, ST-6-60, ST-6-75, ST-6-S75, and ST-7-60.

According to Figure 30a, a more ductile behavior is observed for Hy-5-60, with a steel reinforcing ratio of 1.98%, and G-7-60 and G-7-60 (SG), both with a steel reinforcing ratio of 3.90%. For the rest of the specimens in Figure 30a, an overall brittle failure is observed since they all fractured at a specimen strain of less than about 7.0%. By comparing the response of G-4-60, G-5-60, G-6-60, and G-7-60 specimens in Figure 30a, it is noted that by increasing the steel reinforcing ratio from 1.27% (G-4-60) to 1.98% (G-5-60) and then to 2.83% (G-6-60), only a higher first peak load could be achieved, and an overall brittle failure could not be prevented. A very similar softening response right after the first peak load is experienced by G-4-60, G-5-60, and G-6-60, and they were never able to recover higher loads beyond their first peak load. In other words, their first peak load was the same as their maximum peak load. However, by increasing the rebar reinforcing ratio to 3.90% (G-7-60), the G-7-60 specimen was able to achieve higher loads beyond its first peak load and first dominant crack formation, leading to a more overall ductile behavior. Similarly, by increasing the reinforcing ratio from 1.98% for G-5-75 to 2.83% for G-6-75, a higher first peak load was achieved. For G-5-75 (RR = 1.98%), G-5-100 (RR = 1.98%), and G-6-75 (RR = 2.83%), the steel reinforcing ratio did not, however, prove to be sufficient for these specimens to recover higher loads beyond their first peak load and first dominant crack formation, leading to an overall brittle failure.

According to Figure 30b, both G-5-S75 and G-6-S75 specimens were able to achieve much higher specimen strains at fracture due to their highly ductile embedded stainless steel rebar. It is further observed that G-6-S75 was able to achieve higher loads beyond its first peak load while this was not the case for G-5-S75. It is believed that the initial tensile softening behavior right after the first peak load observed for all of the reinforced G-UHP-FRC specimens, even including G-7-60 and G-6-S75 with a more ductile response, is due to the displacement-controlled nature of the experiment.

According to Figure 30c, as expected, higher peak loads were achieved as the nominal rebar area was increased, and all steel rebars showed strain-hardening after yielding. ST-6-S75 and ST-7-60 achieved higher peak loads as well as tensile ductility and toughness compared to other rebars. Except for ST-5-60 and ST-6-S75, all other steel rebars exhibited a yielding plateau after yielding. Furthermore, it is noticed that as expected, ST-5-75 achieved a higher peak load than ST-5-60, however, ST-6-60 slightly outperformed ST-6-75 by reaching a higher peak tensile load. This is believed to have also led to a very similar tensile performance for G-6-60 and G-6-75, according to Figure 30a.

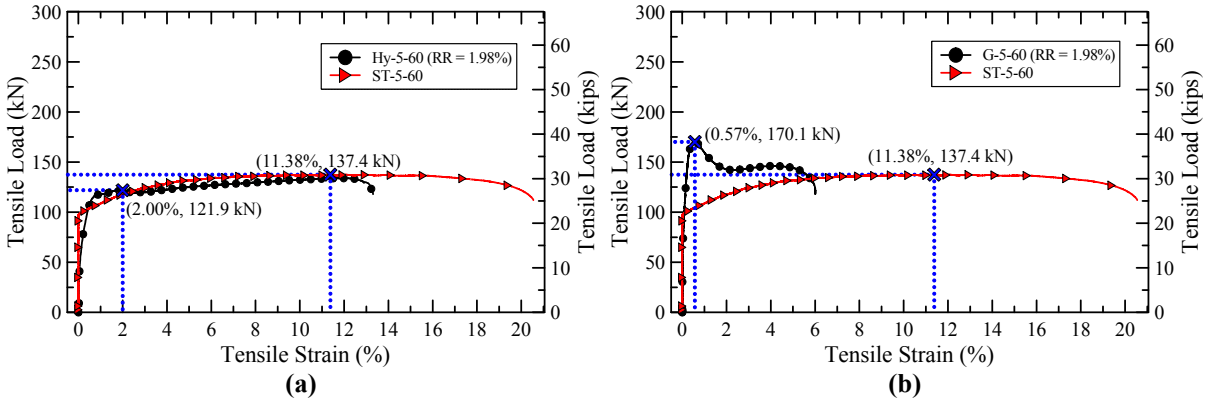

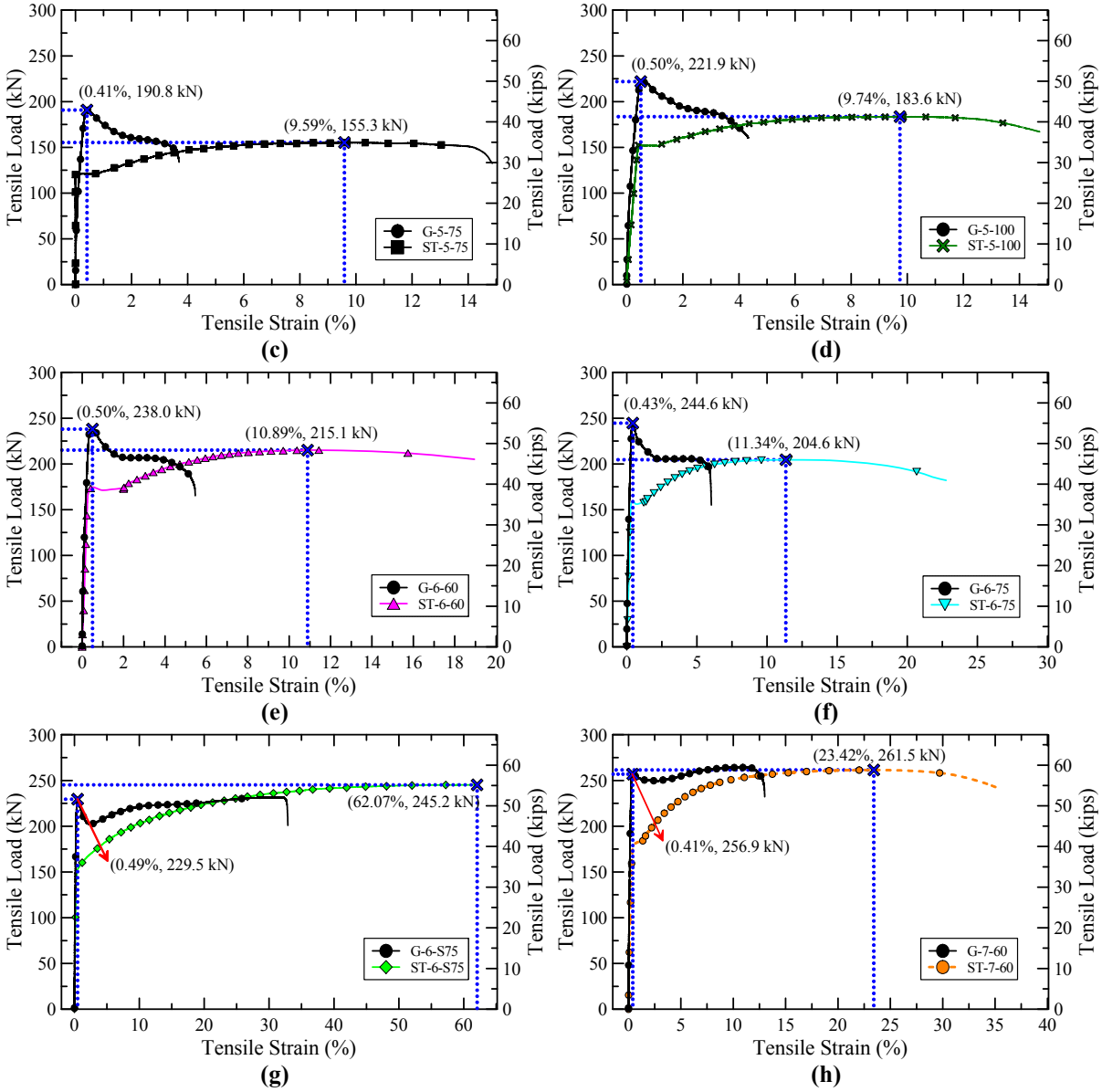

Figure 31 - Total tensile load-strain curves of some representative tension-stiffening specimens with their corresponding bare steel rebar response.

In Figure 31, the first peak tensile load of the tension-stiffening specimens and the ultimate peak tensile load of their embedded bare steel rebar as well as their corresponding average tensile strains are indicated on each graph. It could be observed that for G-5-60, G-5-75, G-5-100, G-6-60, and G-6-75, their first peak load is bigger than the ultimate peak tensile load of their corresponding embedded bare steel rebar. This is believed to be the reason why these tension-stiffening specimens were not able to reach higher loads after their first peak load, and thus exhibited an overall brittle failure. On the other hand, for Hy-5-60, G-6-S75, and G-7-60, however, it is noticed that their first peak load is less than the ultimate peak tensile load of their corresponding embedded bare steel rebar. Therefore, Hy-5-60, G-6-S75, and G-7-60 were all able to achieve higher loads after their first peak load, leading to a more ductile performance up to the fracture of their steel reinforcement. As expressed earlier, it should be noted that increasing the longitudinal steel reinforcing ratio in tension-stiffening specimens (by increasing the rebar size while keeping the concrete dimensions

the same), and thus increasing the ultimate peak tensile load that can be carried by the embedded steel rebar, leads to a higher first peak load for the tension-stiffening specimen as well. Therefore, a more ductile behavior is not guaranteed only by increasing the longitudinal reinforcing ratio of the tension-stiffening specimens, which is, for example, the case when comparing G-6-60 and G-6-75 with G-5-60 and G-5-75, respectively. However, as a higher ultimate peak tensile load for the embedded bare steel rebar is achieved compared to the first peak load of the tension-stiffening specimen, a more ductile behavior is more likely, as was the case for G-7-60 compared to G-6-60.

The summation of the yield strength of the steel rebar and the tensile strength of plain G-UHP-FRC can be considered as an upper bound for the first peak load of reinforced G-UHP-FRC specimens. Therefore, based on the explanation above and the results of G-5-60, G-5-75, G-5-100, G-6-60, G-6-75, G-6-S75, G-7-60, and the tensile response of their corresponding embedded steel rebars, the following equations are used to recommend the minimum required longitudinal reinforcing ratio in reinforced G-UHP-FRC tension specimens to achieve a ductile behavior:

$$c\left(f_{ct}(A_g - A_{st}) + f_{sy}A_{st}\right) < f_{su}A_{st} \tag{5}$$

$$\rho_l > \frac{cf_{ct}}{f_{su} - cf_{sy}} \tag{6}$$

Where c is a constant less than or equal to 1.0 (most conservative), f_{ct} *(MPa)* is the peak tensile strength of plain G-UHP-FRC, f_{sy} and f_{su} *(MPa)* are the yield and peak tensile strength of the embedded steel rebar, respectively, A_g and A_{st} *(mm²)* are the concrete gross cross sectional area and steel rebar area, respectively, and ρ_l is the longitudinal reinforcing ratio, defined as the area of the steel rebar (A_{st}) divided by the net cross sectional area of G-UHP-FRC ($A_g - A_{st}$). A c value of 0.913 is suggested here based on the results, which leads to a coefficient of determination of 0.917. Eq. (6) suggests that the ratio of peak to yield tensile strength (f_{su}/f_{sy} or σ_{pt}/σ_{yt} in Table 15) is of great importance to achieve a ductile behavior, and the higher this ratio, the lower will be the minimum required longitudinal reinforcing ratio.

Table 14 - Tension-stiffening test results.

Specimen Name	Reinforcing ratio (%)	P_t^* (kN)	ε_t† (%)	P_{pt}‡ (kN)	σ_{pt}' (MPa)	ε_{pt}'' (%)	ε_f''' (%)	f'_c£ (MPa)	Time‖ (days)
Hy-5-60	**1.98**	**121.9**	**2.00**	**134.1**	**13.0**	**11.79**	**13.31**	**37.2**‖	**76**
G-4-60	1.27	115.9	0.31	115.7	11.2	0.31	4.75	168.2	160
G-5-60	1.98	170.1	0.57	170.1	16.4	0.57	6.01	155.1	157
G-5-60 (SG)	1.98	140.0	0.44	140.0	13.6	0.44	6.66	-	98
G-5-75	1.98	190.8	0.41	190.8	18.5	0.41	3.69	154.6	260
G-5-S75	1.98	180.1	0.43	180.1	17.4	0.43	35.48	161.7	294
G-5-100	1.98	221.9	0.50	221.9	21.5	0.50	4.33	150.5	255
G-6-60	2.83	238.0	0.50	238.0	23.1	0.50	5.46	156.0	291
G-6-75	2.83	244.6	0.43	244.6	23.7	0.43	6.03	144.7	256
G-6-S75	**2.83**	229.5	0.49	**231.8**	**22.5**	**32.01**	**32.89**	**146.7**	**259**
G-7-60	**3.90**	**256.9**	**0.41**	**264.4**	**25.6**	**10.20**	**13.01**	**160.9**	**289**
G-7-60 (SG)	**3.90**	**227.1**	**0.39**	**258.3**	**25.0**	**10.44**	**12.64**	**-**	**98**

* First peak tensile load

† Strain at first peak tensile load

‡ Peak tensile load
′ Peak tensile strength
″ Strain at peak tensile strength
‴ Strain at fracture of the steel rebar
£ Compressive strength based on average of three samples at the time of testing the tension-stiffening specimens
╫ Time (days) after casting when the tension-stiffening specimens and the companion cubes were tested
‖ Compressive strength after 28 days

Table 15 - Bare steel rebar tensile test results.

Specimen Name	σ_{yt}^{*} (MPa)	$\varepsilon_{y}^{\dagger}$ (%)	$\varepsilon_{sh}^{\ddagger}$ (%)	P_{pt}' (kN)	σ_{pt}'' (MPa)	ε_{pt}''' (%)	$\varepsilon_{f}^{£}$ (%)	$\sigma_{pt}/\sigma_{yt}^{╫}$
ST-5-60	506.8	0.30	0.30	137.4	694.2	11.38	20.25	1.37
ST-5-75	611.3	0.30	0.80	155.3	784.7	9.59	14.86	1.28
ST-5-100	768.1	0.42	1.12	183.6	927.4	9.74	14.72	1.21
ST-6-60	611.6	0.27	2.02	215.1	754.7	10.89	18.95	1.23
ST-6-75	555.6	0.30	1.39	204.6	717.7	11.34	22.77	1.29
ST-6-S75	533.1	0.30	0.30	245.2	860.2	62.07	62.07	1.61
ST-7-60	459.7	0.30	1.40	261.5	674.1	23.42	35.31	1.47

* 0.2% offset yield strength
† Strain at yielding
‡ Strain at the initiation of strain-hardening
′ Peak tensile load
″ Peak tensile strength
‴ Strain at peak tensile strength
£ Strain at fracture of the rebar
╫ Peak to yield tensile strength ratio

Only fiber pullout and no fiber fracture were observed for all the tension-stiffening specimens. A more ductile behavior was observed for Hy-5-60, with a reinforcing ratio of 1.98%, up to a maximum strain of 13.31% as compared to that of 7.4% [29] with a reinforcing ratio of 1.2%. This is attributed to a more uniform elongation along the steel rebar due to both the formation of multiple transverse macro cracks (3–4 cracks) as shown in Figure 29 for Hy-5-60 (at an average specimen strain of about 2.00%) as well as initiation of visible longitudinal splitting cracks on the sides of the specimen at about the same strain value (2.00%). Therefore, a minimum longitudinal reinforcing ratio of ~2.0% (A706 Grade 60 mild steel reinforcement) is recommended to observe an overall ductile behavior for reinforced HyFRC tension members.

According to Table 14 as well as Figure 31 for some representative specimens, G-4-60, G-5-60, G-5-60 (SG), G-6-60, G-5-75, G-6-75, and G-5-100 all illustrated an overall brittle failure since their strain values at fracture of the steel rebar ranged from ~3.7 to ~6.7%, much less than the strain at fracture of the bare rebar, which is more than 14.0% (Table 15). As also mentioned earlier, this was attributed to strain localization at one location due to yielding of the steel reinforcing bar. A visible dominant macro crack then forms at the weakest section because of strain localization. Consequently, further overall elongations (through crack opening) were only limited to the cracked region where early strain-hardening and ultimately fracture of the steel rebar would occur. In addition, no major visible longitudinal splitting cracks were observed for these specimens except for G-6-75 and G-6-60 for both of which a short hairline splitting crack was observed at least on one side at ~1.40% and ~3.00% strains, respectively, after strain localization at 0.43% and ~0.50%

strains, respectively. Hence, ensuring that Eq. (1) is satisfied, which holds for all tension-stiffening specimens except for G-4-60, does not necessarily ensure an overall ductile behavior.

Longitudinal splitting cracks do not form easily in reinforced G-UHP-FRC specimens because of the following reasons: 1) G-UHP-FRC is able to carry loads after cracking due to fiber bridging. Therefore, the steel rebar carries only a part and not all of the total tensile force after first-cracking, depending on the reinforcing ratio. Hence, almost no or much less slippage will occur to cause splitting cracks; 2) G-UHP-FRC is about 5–6 times stronger than conventional plain concrete and HyFRC, thus the tensile stresses exerted on G-UHP-FRC by the steel rebar ribs (Figure 27) have to be more than the tensile strength of G-UHP-FRC for any longitudinal splitting cracks to initiate; 3) even after the initiation of such cracks, they are immediately bridged and confined by fibers, making it harder for these cracks to propagate; and 4) in addition, concrete crushing in between the rebar ribs after large overall deformations, which can lead to a more uniform elongation along the steel rebar, is unlikely due to ultra-high compressive strength of G-UHP-FRC.

An overall ductile response was recorded for G-7-60, G-7-60 (SG), G-5-S75, and G-6-S75. For G-7-60, which reached a maximum strain of 13.01%, this was attributed to the formation of two dominant transverse macro cracks, initiated simultaneously at 0.42% strain immediately after its first peak strength, as well as longitudinal splitting cracks, as illustrated in Figure 32. Initiation of hairline splitting cracks was first recorded at a strain of ~1.19% for G-7-60 on the sides surface, which then grew longer and wider up to the maximum tensile load at a strain of 10.20%. Maximum transverse macro crack and longitudinal splitting crack openings of 24.5 and 2.3 mm, respectively, were recorded for G-7-60. Based on the results of this specimen, it is believed that the initiation and formation of longitudinal splitting cracks significantly contributes to achieving an overall ductile behavior. This is due to partial loss of bond between the G-UHP-FRC matrix and the steel rebar, allowing for propagation of plastic deformation along the steel rebar, which is further explored in Section 4.3.4.

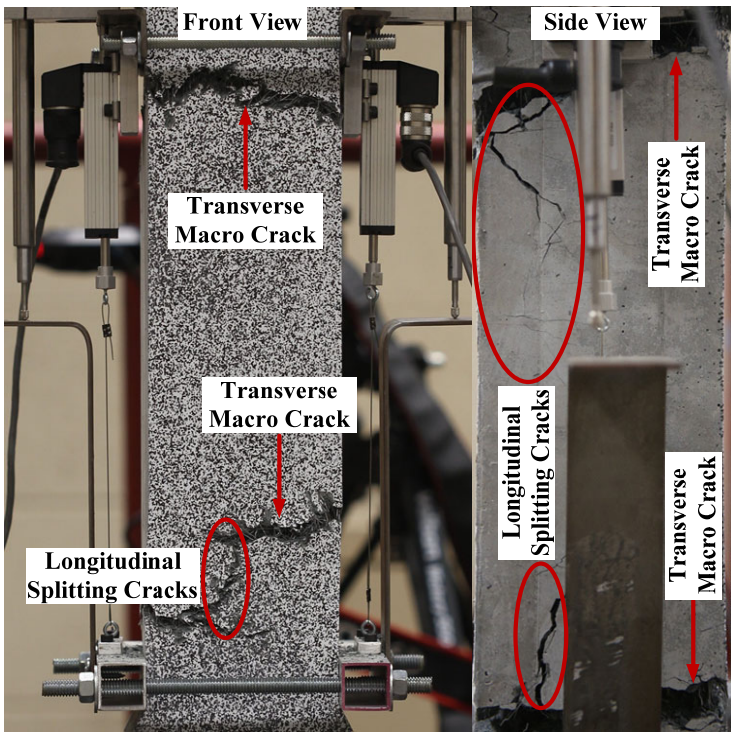

Figure 32 - Longitudinal splitting cracks and multiple transverse macro cracks for G-7-60 (RR = 3.90%).

Though G-5-S75 reached a maximum strain (at fracture of its reinforcing rebar) of 35.48% and thus showed a ductile behavior, its maximum load was recorded at 0.43% strain. It only experienced a single transverse macro crack and no visible longitudinal splitting cracks. Its high ductility, therefore, is believed to be due to the fact that its bare stainless steel reinforcing bar achieves very high ductility with strain at fracture of more than 60%. Furthermore, a 9.0% uniform reduction in diameter of the stainless steel rebar due to Poisson's effect was observed for the embedded rebar of G-5-S75, which at the end, fractured outside of the gauge length.

G-6-S75 reached its maximum tensile load at 32.01% and its maximum strain (at fracture of its reinforcing bar) at 32.89%. This ductile behavior is believed to be due to the formation of multiple transverse macro and longitudinal splitting cracks. Similar to G-5-S75, a 7.9% uniform reduction in diameter, due to Poisson's effect, was measured for the embedded stainless steel reinforcing bar of G-6-S75 after its removal from the test setup. Two major differences, however, were observed for G-6-S75 compared to G-7-60: 1) the initiation of the longitudinal splitting cracks was delayed until ~4.48% strain compared to ~1.19% of G-7-60, and 2) the second macro crack was not formed until a strain of 14.80% was reached while both dominant macro cracks of G-7-60 initiated at 0.42% strain, which also corresponded to its first peak load. While the two simultaneous dominant cracks of G-7-60 (at 0.42% strain) as well as the first macro crack of G-6-S75 (at 0.65% strain) initiated due to strain localization at the weakest sections shortly after rebar yielding, the second dominant crack of G-6-S75 (at 14.80% strain) is believed to have formed due to redistribution of tensile forces as a result of the formation of longitudinal splitting cracks.

It is believed that for G-7-60 and G-6-S75, the initiation and propagation of longitudinal splitting cracks were made possible due to three main reasons: 1) by increasing the longitudinal reinforcing ratios for these specimens, the load taken by the steel rebar at the transverse macro crack region is

larger and therefore, slippage between rebar and G-UHP-FRC is more likely to occur, leading to development of higher bond stresses that can cause longitudinal splitting cracks to initiate and 2) according to Figure 33, when a higher longitudinal reinforcing ratio is used (by using a larger rebar size while concrete dimensions are kept constant), effective confinement on the steel rebar is reduced due to the existence of less G-UHP-FRC matrix as well as fibers surrounding the rebar, thus leading to a lower bond strength, which in turn, makes the formation of longitudinal splitting cracks easier, and 3) a higher reinforcing ratio, as could be inferred from Figure 33, results in a shorter crack length due to a smaller cover (for both transverse macro and longitudinal splitting cracks) along the cross section of the specimen, and thus allowing longitudinal splitting cracks to propagate more easily and rapidly.

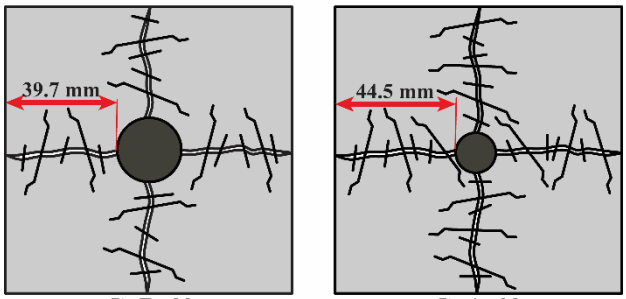

Figure 33 - Rebar confinement and splitting crack formation for G-7-60 (RR = 3.90%) versus G-4-60 (RR = 1.27%)

4.3.2 Rebar strain-hardening and fracture for gauged specimens

The full load-strain response of the two specimens that included strain gauges, namely G-5-60 (SG) and G-7-60 (SG) are given in Figure 30a. The strain measured by the nine individual strain gauges along the embedded rebar in G-5-60 (SG) and G-7-60 (SG) specimens are shown in Figure 34a and Figure 34b, respectively, as the average specimen strain increases up to the fracture of the embedded rebar at 6.7% and 12.6%, respectively. For G-5-60 (SG), SG-1 was damaged at an average specimen strain of about 4.2%, and for G-7-60 (SG), SG-1, SG-6, and SG-2 stopped recording at average specimen strains of 1.0%, 5.2%, and 6.2%, respectively. According to the results of Figure 30c and Table 15, where the tensile load versus strain response of bare steel rebars are presented, the onset of strain-hardening for ST-7-60 was observed at 1.4% strain, indicated in Figure 34b with a red dashed line, while for ST-5-60, the onset of its strain-hardening was observed right after yielding at a strain of about 0.3%. As seen in Figure 34a, a nonuniform strain distribution along the embedded rebar with strain localizations at SG-1 and SG-4 were recorded for G-5-60 (SG). One dominant crack formed at the location of SG-1, reaching up to about 10.0% strain as measured by SG-1, thus confirming early strain-hardening and consequently fracture of the steel rebar at this location.

On the other hand, in Figure 34b, a uniform strain distribution was recorded along the embedded rebar in the G-7-60 (SG) specimen, and all nine strain gauges experienced strains well beyond the initiation of strain-hardening at 1.4% strain. This points to distributed plasticity and therefore, better use of material along the G-7-60 (SG) specimen, which is in contrast to the behavior of the G-5-60 (SG) specimen. As also mentioned before, this is attributed to the formation of multiple transverse macro cracks, including two main dominant cracks, one at the location of SG-1, which initiated at a specimen strain of about 0.45% and another between SG-5 and SG-6 at a specimen

strain of about 1.64%, as well as longitudinal splitting cracks that became visible on the side surfaces at specimen strains of 0.75%, 1.90%, and 2.28% toward the top, middle, and bottom of the specimen, respectively. The latter two visible splitting cracks were connected at a later specimen strain of about 6.54%, indicating distribution of plasticity along the steel rebar.

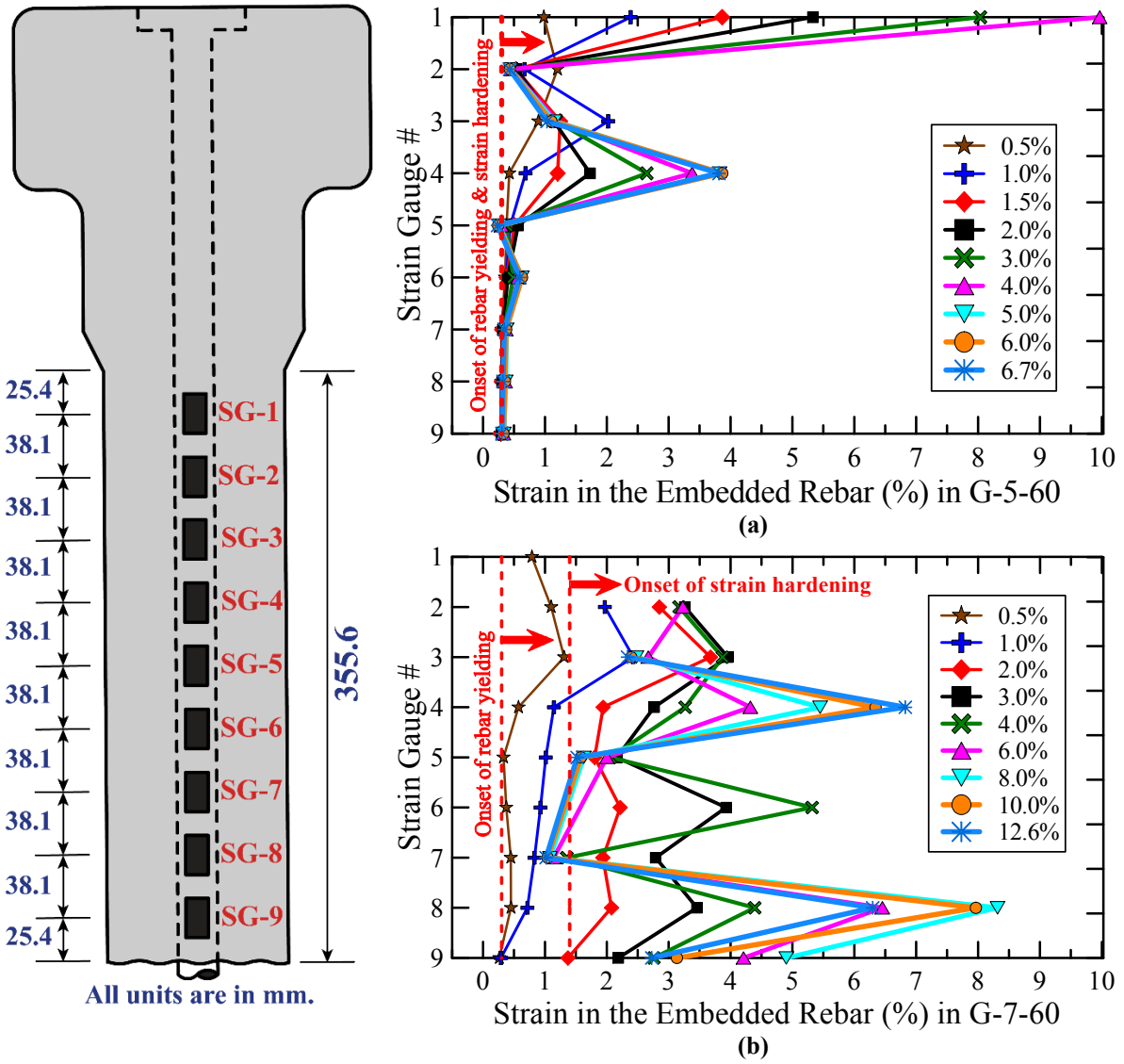

Figure 34 - Strain in the embedded rebar inside (a) G-5-60 (SG) and (b) G-7-60 (SG) at different levels of total specimen strain, which is indicated in the legends.

Figure 35a and Figure 35b compare strain in the embedded steel rebar versus average strain in the tension-stiffening specimens G-5-60 (SG) and G-7-60 (SG), respectively. Figure 35c locates the onset of strain-hardening in the steel reinforcing bar at the location of each individual strain gauge. The following observations are drawn from these plots: 1) for G-5-60 (SG) except for SG-1 and SG-4, all gauges experienced very small strain values due to the formation of one dominant macro crack at the location of SG-1, 2) for G-7-60 (SG) on the other hand, while SG-1, SG-2, and SG-6 were damaged before the end of the experiment due to the formation of macro cracks at or near their location, other gauges also experienced much higher strain values beyond that of 1.4% at the onset of strain-hardening, 3) for G-7-60 (SG), all strain gauges started to strain-harden (at 1.4%

steel rebar strain) between specimen strain values of 0.54–2.02% according to Figure 35c; SG-1 experienced early strain-hardening at 0.54% specimen strain due to the formation of a transverse macro crack at its location whereas the onset of strain-hardening at SG-9 was delayed until a specimen strain of 2.02% after the formation and propagation of a longitudinal splitting crack and hence partial loss of bond stress near its location, 4) Figure 35a and Figure 35b also indicate partial unloading for multiple gauges in both specimens, which is more realistic and conservative and as mentioned before, allowed to occur since the tensile load is transferred through the dogbone shape of tension-stiffening specimens as compared to applying the load on the steel rebar, extending at the two ends [29,59], which does not allow for this phenomenon to happen, and 5) for both specimens, all strain gauges experienced equal strain values up to about 0.3% specimen strain, which corresponds to the yield strain of both ST-5-60 and ST-7-60.

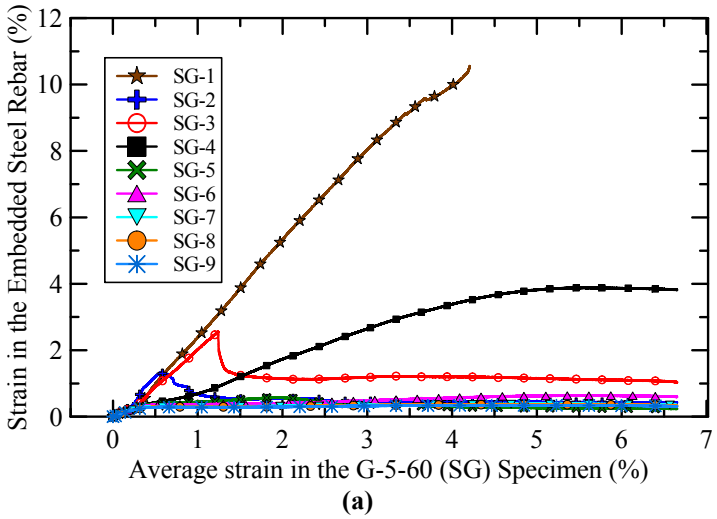

(a)

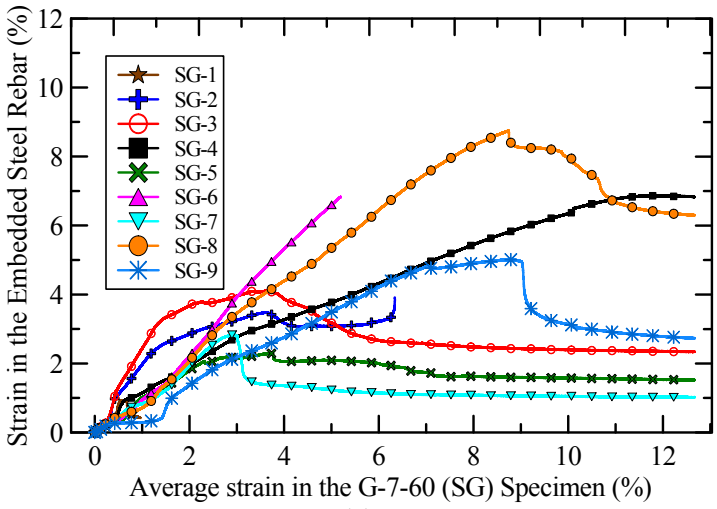

(b)

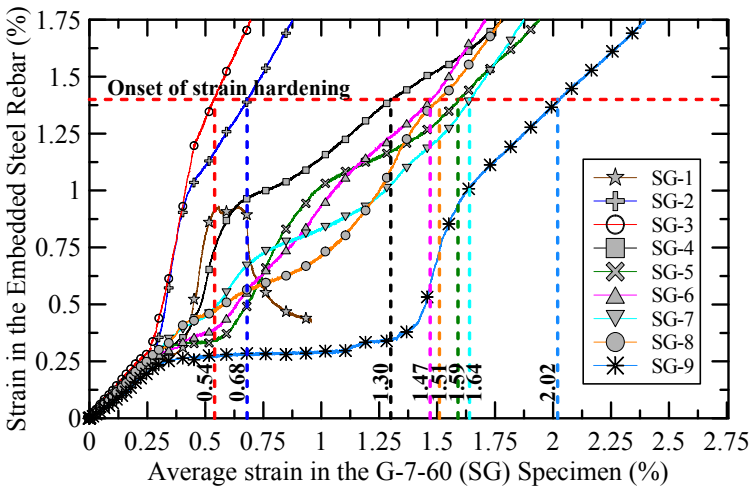

(c)

Figure 35 - Strain in the embedded steel rebar versus average strain in the tension-stiffening specimen for (a) G-5-60 (SG) and (b) G-7-60 (SG) up to fracture of the reinforcing steel bar and (c) for G-7-60 (SG) indicating the instant of strain-hardening initiation for each individual strain gauge.

4.3.3 Corrected tensile response of plain G-UHP-FRC based on the tension-stiffening specimens

For G-5-60 (SG) and G-7-60 (SG), the load carried by the embedded steel rebars at any time during testing could be estimated by using the strain values measured by their nine strain gauges and the corresponding load-strain curves of bare steel rebars in Figure 30d, namely those of ST-5-60 and ST-7-60. Then, by subtracting the average load, carried by the steel rebar, from the total load carried by the tension-stiffening specimen, the load carried by G-UHP-FRC can be estimated, from which a more realistic tensile response of plain G-UHP-FRC composites could be derived. This corrected tensile response could then be used to further estimate the nominal flexural strength of reinforced G-UHP-FRC beams with steel rebars as well as bond behavior analysis discussed in Section 4.3.4.

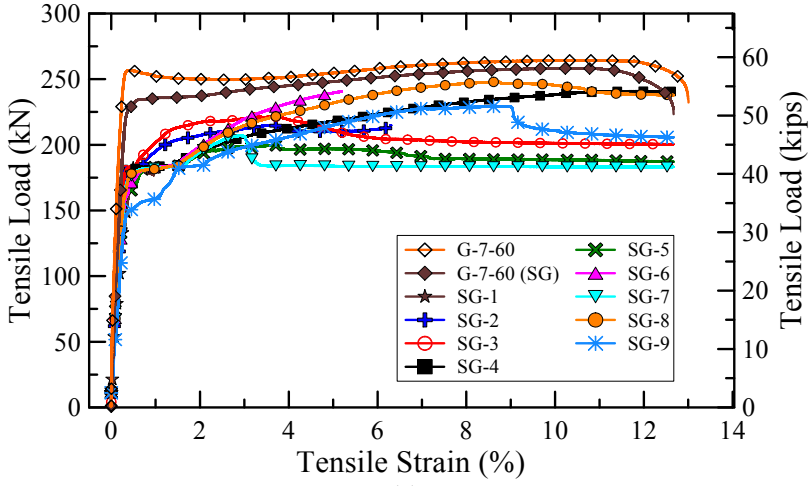

(a)

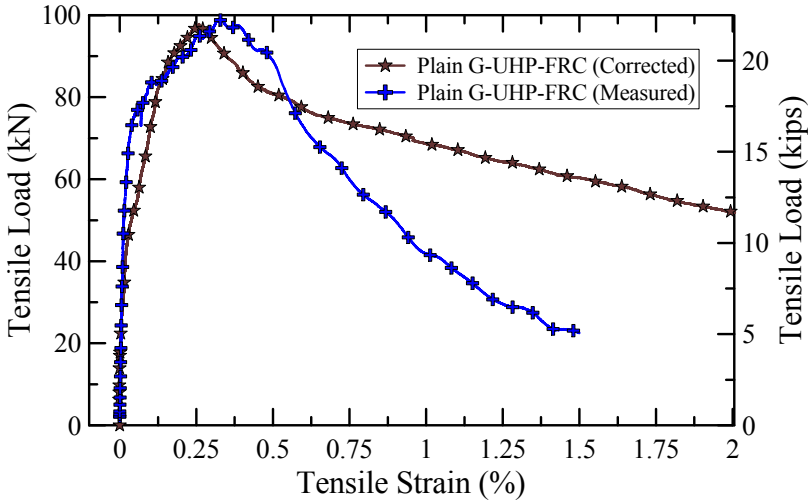

(b)

Figure 36 - (a) Tensile load-strain response of the embedded rebar in G-7-60 (SG) at the location of each of its strain gauges and (b) corrected tensile load-strain response of plain G-UHP-FRC based on tension-stiffening specimens.

Here, this approach was done based on the responses of G-7-60, G-7-60 (SG), and ST-7-60 specimens. Loads carried by the embedded rebar in G-7-60 (SG) were first estimated, using the response of ST-7-60, at every moment during testing at the location of each of its strain gauges, as illustrated in Figure 36a. The average load carried by the embedded rebar was then subtracted from the total load carried by the G-7-60 tension-stiffening specimen to calculate the average tensile load carried by plain G-UHP-FRC. The reason that the total load carried by the tension-stiffening specimen G-7-60 was selected instead of G-7-60 (SG) was that G-7-60 (SG), as could also be inferred from Figure 36a, slightly underperformed in regard to its stiffness and peak strength compared to G-7-60 (with no strain gauges on its embedded rebar). This is because the surface of the embedded rebar in G-7-60 (SG) had to be slightly grinded and prepared for strain gauges installation at nine locations along the rebar, which led to a slightly lower tensile capacity due to a reduced cross sectional rebar area. This, however, was not the case for the bare rebar specimen ST-7-60, which was tested using an extensometer instead of strain gauges, the response of which was used to estimate the load carried by the embedded rebar in G-7-60 (SG) at the location of its strain gauges. The corresponding corrected tensile response of G-UHP-FRC is plotted in Figure 36b, using the method described above, along with the tensile response of unreinforced G-UHP-FRC from Chapter 2 (Figure 5) for comparison purposes. According to Figure 36b, very similar initial stiffness, strain-hardening branch, and peak strength are observed for the corrected response of G-UHP-FRC compared to its response when unreinforced. However, the post-peak softening branch based on the corrected response is improved as G-UHP-FRC is able to continue carrying tensile loads up to higher strains and at a slower softening rate. This behavior is believed to be due to a more controlled crack opening as well as multiple transverse macro crack formation due to the presence of the steel reinforcing bar.

4.3.4 Tension-stiffening effect and bond behavior analysis

According to the explanations presented in Section 4.2.5, concrete surface strains, obtained from DIC, and the corresponding concrete and bond stresses at different stages of testing for G-7-60 are

illustrated in Figure 37. It should be noted that the scale for concrete surface strain changes (leftmost plot of each graph) as transverse macro cracks grow in size.

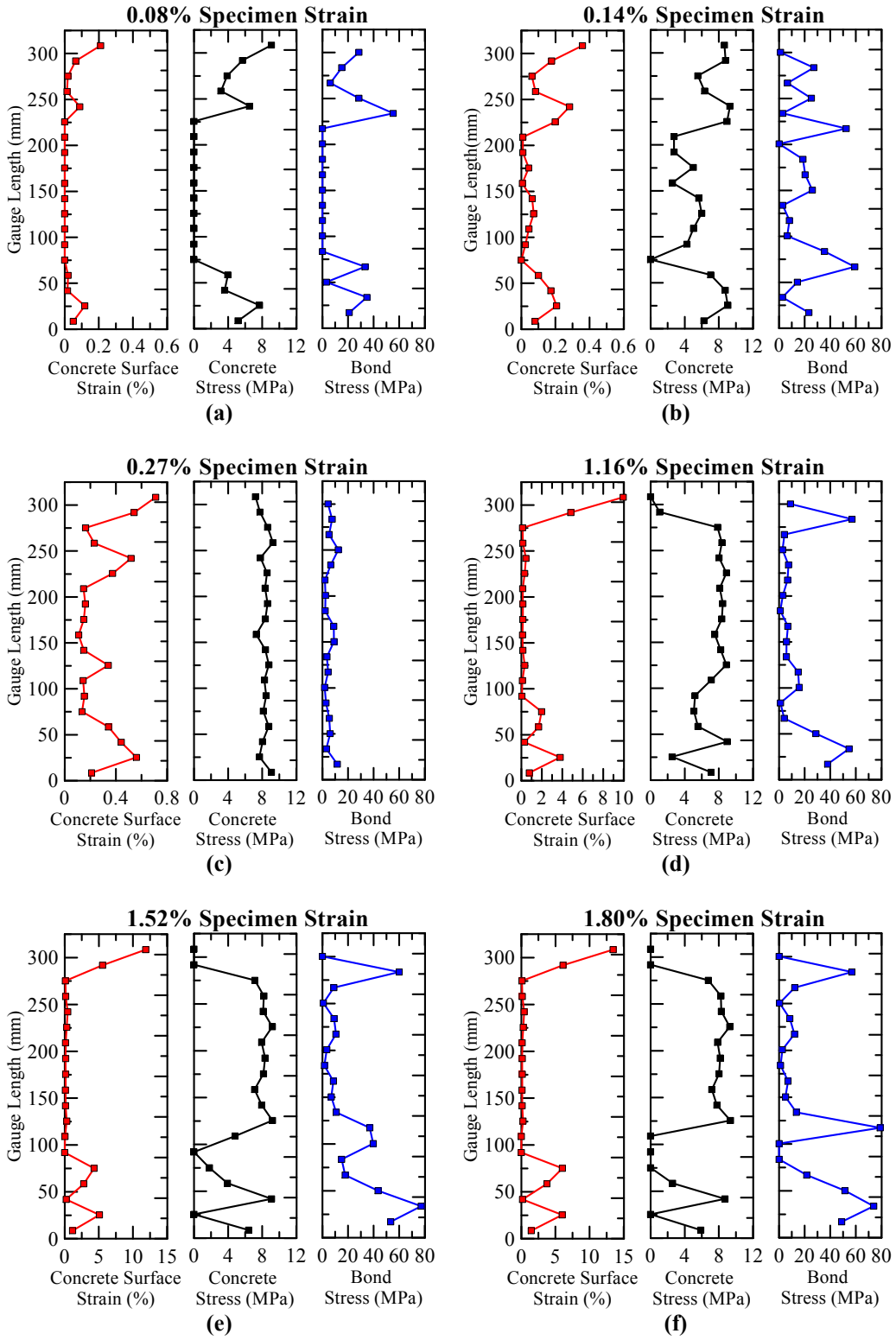

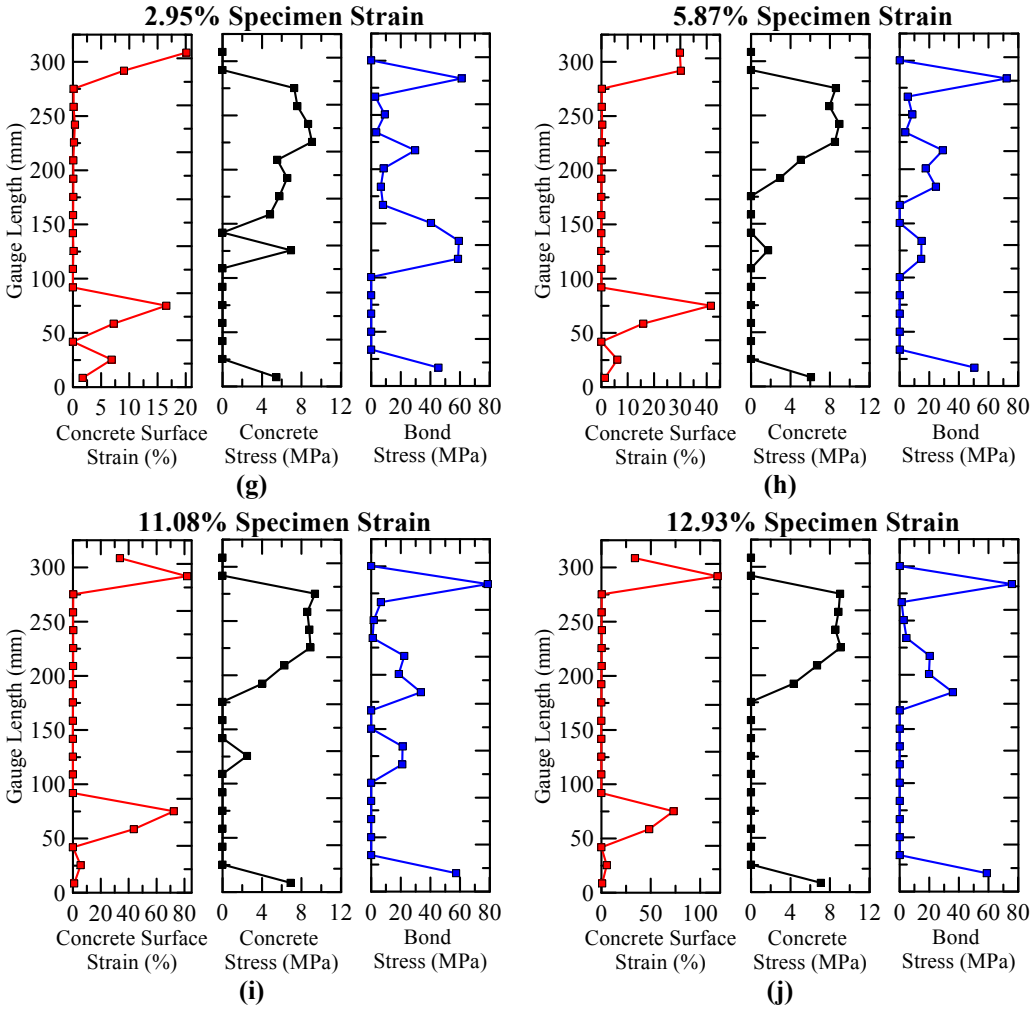

Figure 37 - Concrete strains and the corresponding concrete and bond stresses at (a) 0.08, (b) 0.14, (c) 0.27, (d) 1.16, (e) 1.52, (f) 1.80, (g) 2.95, (h) 5.87, (i) 11.08, and (j) 12.93% tensile specimen strains for G-7-60.

The steel rebar embedded in the tension-stiffening specimens along with the surrounding G-UHP-FRC could be simplified to constitute a parallel spring model. According to Figure 37a, it is observed that shortly after loading the G-7-60 specimen, the embedded steel rebar first attracts more loads because of its higher modulus of elasticity compared to G-UHP-FRC. The load carried by the rebar is then partially transferred into G-UHP-FRC through the development of bond stresses up to ~60 MPa towards the ends of the gauge length (Figure 37a [0.08% average specimen strain] and Figure 37b [0.14% average specimen strain]) until a more uniform concrete stress level is developed in G-UHP-FRC all along the gauge length, leading to a significant drop in bond stresses below ~12 MPa and a more compatible deformation of G-UHP-FRC and the embedded rebar (Figure 37c [0.27% specimen strain]) up to yielding of the rebar. Immediately after, strain localization leads to formation of two macro cracks towards the ends of the gauge length, where fibers are quickly exhausted and bond stresses up to ~60 MPa are again developed, due to local rebar slippage as explained before, to partially transfer the load carried by the steel rebar at the location of macro cracks back to G-UHP-FRC (Figure 37d [1.16% specimen strain]). This happens over a very short embedment length as could be inferred from Figure 37d, which, though not quantified, is believed to be due to high bond strength of G-UHP-FRC. From Figure 37d–f (1.16–1.80% specimen strain), it could also be inferred that the local deformation at the top macro crack

is more pronounced than the bottom macro crack. Therefore, the rebar at the location of the top macro crack undergoes strain-hardening earlier, thus slowing down the rate of deformations at this crack. Figure 37e–f (1.52–1.80% specimen strain) further show that bond stresses up to ~80 MPa towards the bottom of the gauge length result in the initiation and propagation of longitudinal splitting cracks along the rebar in this region, which in turn can lead to unloading of G-UHP-FRC and a more uniform distribution of plasticity over a longer distance along the rebar in this region. This is consistent with the appearance of hairline longitudinal splitting cracks on the side surfaces at a total specimen strain of ~1.19%. According to Figure 37g-h (2.95–5.87% strain) then, the bottom macro crack continues opening at a faster rate, surpassing the width of the top macro crack. Finally, Figure 37f–j show a gradual shift in the development of bond stresses from the bottom of the gauge length towards the middle and top of the specimen, leading to the propagation of the longitudinal splitting crack further up that initiated earlier and therefore, causing the concrete in these regions to unload. This further spread the plasticity in the rebar over a longer length, hence leading to an overall ductile behavior observed for G-7-60. According to Figure 37i–j, the top macro crack started opening again after the peak load (at 10.20% specimen strain) and exhaustion of its strain-hardening capacity and surpassed the width of the bottom macro crack, leading to the fracture of the steel rebar at its location at a specimen strain of 13.01%.

Maximum bond stresses of up to about 80 MPa, though seem to be high, are nonetheless consistent with bond stress-slip response of UHP-FRC composites based on direct rebar pullout tests presented in [60], where bond stresses just beyond 80 MPa were measured. These results, however, need to be further confirmed and should for now be considered with caution.

In addition, steel and bond stresses at different stages of testing for G-7-60 (SG) are illustrated in Figure 38.

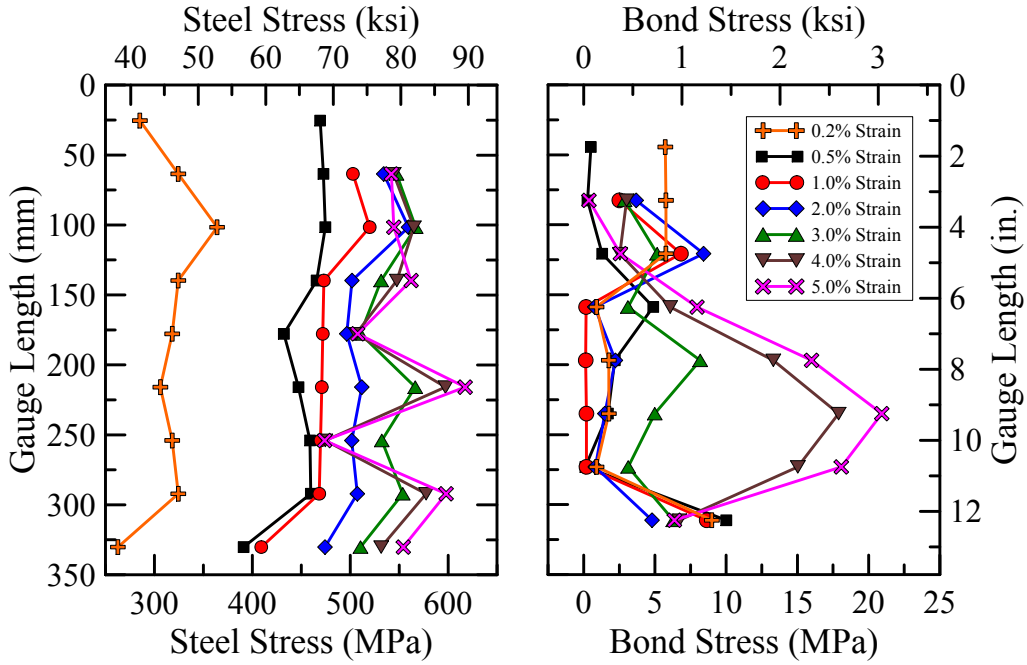

Figure 38 - Steel and bond stresses along the gauge length for G-7-60 (SG)

According to the results presented in Figure 38, bond stresses just over 10 MPa were developed up to an average specimen strain of about 3.0% after which higher bond stresses up to a maximum

value of 24.4 MPa were calculated as a result of a more significant stress gradient in the steel rebar between the cracked and uncracked regions due to partial unloading and relaxation of the rebar in the uncracked region.

It is noted that maximum bond stresses up to about 80 MPa for G-7-60 (calculated based on concrete stress gradient) and about 24 MPa based on G-7-60 (SG) (calculated from steel stress gradient) are significantly different. This may be due to two factors, 1) local distortions in concrete strain measurements based on DIC near macro cracks might have led to unusual concrete stress gradients and thus high bond stresses calculated here and 2) instalment of nine very closely located strain gauges on the embedded rebar in G-7-60 (SG) might have caused a significant drop in the bond strength, leading to much lower bond stresses with a maximum value of about 24 MPa. Therefore, further comprehensive experiments should be conducted to validate the results presented in this section.

4.4 Summary and conclusions

In this research, eleven G-UHP-FRC and one HyFRC dogbone-shaped tension-stiffening specimens reinforced with a single deformed steel reinforcing bar, extending the full length of the specimens in the middle, were tested under uniaxial tension up to fracture of the steel rebar. Through these tests, it was observed that initially, G-UHP-FRC (or HyFRC) and the reinforcing rebar deformed compatibly and carried the applied tensile force proportional to their modulus of elasticity and area with no major slippage until the yielding initiation of the steel rebar. Then, rebar yielding led to strain localization at one or two locations along the gauge length, where transverse macro cracks formed, and fiber pullout was observed. At these macro cracks, after the exhaustion of the fibers bridging the cracks, almost all the tensile load was carried by the steel rebar. This led to localized elongation in the rebar, resulting in the first peak load and thereafter initial softening, followed by early strain-hardening of the reinforcing bar at the locations of the transverse macro cracks. If the longitudinal reinforcing ratio is below ~4.0% and ~2.0% (A706 Grade 60 mild steel) for G-UHP-FRC and HyFRC, respectively, this results in a premature fracture of the steel rebar, leading to an overall brittle failure. However, if a minimum longitudinal reinforcing ratio of ~4.0% and ~2.0% is provided for G-UHP-FRC and HyFRC, respectively, the rebar can take greater loads after the first peak tensile load, leading to the formation of multiple transverse macro cracks and longitudinal splitting cracks, which in turn allows for the distribution of plasticity over a longer distance along the rebar, and therefore, an overall ductile behavior.

To summarize, the following general summaries and conclusions can be drawn from this research:

1. Hy-5-60 (HyFRC reinforced with a No. 5 A706 Grade 60 mild steel rebar), with a longitudinal reinforcing ratio of 1.98% showed an overall ductile behavior up to a maximum strain of 13.31%. This behavior was attributed to the formation of both multiple transverse macro cracks as well as longitudinal splitting cracks. Therefore, a minimum longitudinal reinforcing ratio of ~2.0% of A706 Grade 60 mild steel is recommended to observe an overall ductile behavior for reinforced HyFRC tension members.
2. An overall ductile response was recorded for G-7-60 (G-UHP-FRC reinforced with a No. 7 A706 Grade 60 mild steel rebar with a longitudinal reinforcing ratio of 3.90%), G-5-S75 (G-UHP-FRC reinforced with a No. 5 A276 Grade 75 stainless steel rebar with a longitudinal reinforcing ratio of 1.98%), and G-6-S75 (G-UHP-FRC reinforced with a No. 6 A276 Grade 75 stainless steel rebar with a longitudinal reinforcing ratio of 2.83%).

3. G-7-60 illustrated a ductile behavior up to a maximum strain of 13.01%, which is due to the formation of both multiple transverse macro cracks as well as longitudinal splitting cracks. Therefore, a minimum longitudinal reinforcing ratio of ~4.0% of A706 Grade 60 mild steel is suggested to achieve an overall ductile behavior for reinforced G-UHP-FRC tension members.
4. Although G-5-S75 exhibited a ductile behavior because of its highly ductile steel reinforcing bar (No. 5 A276 Grade 75 stainless steel rebar), its peak load was recorded at a low specimen strain of 0.43%. G-6-S75, however, reached an overall ductile behavior up to a maximum strain of 32.01% due to the formation of multiple transverse macro cracks and longitudinal splitting cracks. Therefore, a minimum reinforcing ratio of ~3.0% of A276 Grade 75 stainless steel rebar is also recommended as an alternative to obtain an overall ductile behavior for reinforced G-UHP-FRC tension members.
5. Based on the results of Hy-5-60, G-7-60, G-7-60 (SG), and G-6-S75 tension-stiffening specimens, spread of plasticity over a longer distance along the embedded rebar, due to initiation and propagation of longitudinal splitting cracks, significantly contributes to achieving an overall ductile behavior, due to partial loss of bond. This is because by using higher longitudinal reinforcing ratios for these specimens, the load taken by the steel rebar is larger and therefore, slippage between rebar and G-UHP-FRC is more likely to occur at the cracked region, leading to development of higher bond stresses that can cause longitudinal splitting cracks to initiate. Furthermore, when a higher longitudinal reinforcing ratio is used, effective confinement on the steel rebar is reduced due to the existence of less G-UHP-FRC matrix and fibers around the rebar, thus causing a lower bond strength, which in turn, makes the formation of longitudinal splitting cracks easier. Also, a higher reinforcing ratio, leads to a shorter crack length due to a smaller cover along the cross section of the specimen, and thus allowing longitudinal splitting cracks to propagate more easily and rapidly.
6. All other G-UHP-FRC tension-stiffening specimens, such as G-4-60, G-5-60, G-5-60 (SG), G-5-75, G-5-100, G-6-60, and G-6-75, with longitudinal reinforcing ratios less than 4.0% tested in this research showed a more brittle failure (with strain values at fracture of the steel rebar between ~3.7 to ~6.7%). This behavior was attributed to strain localization immediately after rebar yielding, early strain-hardening and finally, early fracture of the reinforcing rebar at the location of one transverse macro crack. No major longitudinal splitting cracks were observed for these samples, hence, not allowing for the spread of plasticity along the rebar.
7. For G-5-60, G-5-75, G-5-100, G-6-60, and G-6-75, their first peak load was bigger than the ultimate peak tensile load of their corresponding embedded bare steel rebar. This is believed to be the reason why these tension-stiffening specimens were not able to reach higher loads after their first peak load, and thus exhibited an overall brittle failure. On the other hand, for Hy-5-60, G-6-S75, and G-7-60, it was noticed that their first peak load is less than the ultimate peak tensile load of their corresponding embedded bare steel rebar. Therefore, Hy-5-60, G-6-S75, and G-7-60 were all able to achieve higher loads after their first peak load, leading to a more ductile performance up to the fracture of their steel reinforcement. It was further noted that increasing the longitudinal steel reinforcing ratio in tension-stiffening specimens, and thus increasing the ultimate peak tensile load that can be carried by the embedded steel rebar, leads to a higher first peak load for the tension-stiffening specimen as well. Therefore, a more ductile behavior is not guaranteed only by

increasing the longitudinal reinforcing ratio of the tension-stiffening specimens, which is, for example, the case when comparing G-6-60 and G-6-75 with G-5-60 and G-5-75, respectively. However, once by increasing the longitudinal reinforcing ratio, a higher ultimate peak tensile load for the embedded bare steel rebar is achieved compared to the first peak load of the tension-stiffening specimen, a more ductile behavior is more likely, as was the case for G-7-60 compared to G-6-60.

8. An equation is recommended for the minimum required longitudinal reinforcing ratio in reinforced G-UHP-FRC and UHP-FRC tension elements, which mainly depends on the ratio of the peak to yield tensile strength of the steel reinforcing bar as well as the tensile strength of the G-UHP-FRC or UHP-FRC composite.
9. Nonuniform strain distribution along the embedded rebar in the G-5-60 (SG) specimen was recorded, leading to the formation of a single dominant crack, early strain-hardening of the embedded rebar at its location, and thus early fracture of the steel rebar, resulting in a more brittle failure. In contrast, a more uniform strain distribution was measured along the embedded steel rebar in the G-7-60 (SG) specimen, and all of its nine strain gauges experienced strains well beyond the onset of strain-hardening (at 1.4% strain for the steel rebar) between specimen strain values of 0.54–2.02%. This again points to a better distributed plasticity that is attributed to the formation of multiple transverse macro cracks as well as longitudinal splitting cracks. For both G-5-60 (SG) and G-7-60 (SG) specimens, all strain gauges experienced equal strain values up to about 0.3% specimen strain, i.e. up until rebar yielding.
10. Using the strain values measured by the strain gauges installed on the embedded rebar in the G-7-60 (SG) specimen and the tensile response of bare No. 7 A706 Grade 60 mild steel rebar, the average load carried by the embedded steel rebar in G-7-60 (SG) was estimated at all times during testing. The load carried by G-UHP-FRC was then calculated by subtracting this average load carried by the steel rebar from the total load carried by the G-7-60 specimen. This resulted in a corrected tensile response for plain G-UHP-FRC that was later used for bond behavior analysis and is also necessary for estimating the nominal flexural strength of reinforced G-UHP-FRC. By comparing the corrected tensile response of plain G-UHP-FRC (when reinforced with steel reinforcing bars) with its previously recorded tensile response based on an unreinforced G-UHP-FRC specimen (Chapter 4), a similar stiffness, strain-hardening, and peak strength were observed for both responses. However, an improved post-peak softening branch with a shallower slope was observed based on the corrected response. Therefore, it is believed that reinforcing G-UHP-FRC with steel rebars will mostly affect and more specifically improve the post-peak properties of plain G-UHP-FRC composite materials, however, as discussed at length, if the longitudinal reinforcing ratio is less than ~4.0% for A706 Grade 60 mild steel and ~3.0% for A276 Grade 75 stainless steel rebars, an overall brittle failure is very likely to occur.
11. By using Digital Image Correlation (DIC) techniques in tension-stiffening experiments, concrete and bond stresses along the region of interest can be estimated from which the flow of stresses from the rebar to concrete and vice versa and hence, the composite behavior of concrete and steel reinforcing bar can be monitored and better understood. This further allows for a more accurate identification of transverse and longitudinal splitting crack formations. Based on such an analysis for the G-7-60 specimen, bond stresses of up to about 80 MPa were calculated, and flow of internal stresses and crack formations were investigated. In addition, based on strain values measured by nine strain gauges on the

embedded rebar in G-7-60 (SG) and the tensile response of it bare steel rebar (ST-7-60), steel and thus bond stresses were calculated along the gauge length. According to this set of results, bond stresses about 10 MPa were recorded up to an average specimen strain of about 3.0% after which higher bond stresses up to a maximum value of 24.4 MPa were calculated in G-7-60 (SG).

12. The results suggest that the formation of the first macro crack in reinforced HP-FRCC and UHP-FRC composite materials is controlled by the relatively low strain value of steel rebar at its yielding point (~0.3–0.4%), and therefore, developing concrete composites with tensile strain values far exceeding 0.3%, which has been the main focus of many researchers during the past few years, may not be of great advantage, at least for structural applications, unless other materials with no significant yielding or change in stiffness after initial yielding are used as reinforcement in HP-FRCC and UHP-FRC.

Chapter 5

Concluding Remarks

Ultra-High Performance Fiber-Reinforced Concrete (UHP-FRC) and green UHP-FRC (G-UHP-FRC) have ultra-high compressive, tensile, and shear strengths (four to five times that of conventional concrete and high performance concrete composites) as well as ductility, durability, and crack-resistant capability. However, UHP-FRC is typically made by using a very low water-to-cementitious materials ratio; hence, it is often extremely viscous and suffers from low flowability, especially when adding a high volume of fibers. Development of UHP-FRC composites without using any special materials or treatments has been made possible by employing the dense particle packing approach. Choosing slightly larger particle sizes than suggested by the particle packing density theory for some of the smaller particles can create instability and reduce interlocking between different particles and thus improve flowability. However, this alone, does not seem to be sufficient to achieve desirable flowability for UHP-FRC composites. This research as well as prior research [11,37,38] investigated other mechanisms which can significantly improve the flowability of UHP-FRC and G-UHP-FRC mixtures for large-scale applications. These mechanisms include but are not limited to reducing the inter-friction between different particles using constituent materials with spherical particles, such as fly ash, slowing down the stiffening and setting effects of cement through its partial replacement by industrial by-products, and reducing water demand by slightly increasing the size of filler particles, i.e. silica fume particles etc., to reduce the total particle surface area.

Almost all UHP-FRC mixes, including in prior research [11], use high volumes of Portland cement, about twice as much as conventional concrete. This leads to high heat of hydration, and hence thermal cracking, as well as high carbon dioxide emissions, contributing to climate change, all of which are of major concern. This research first focused on developing a more sustainable green UHP-FRC (G-UHP-FRC) of high workability while ensuring a minimum compressive strength of 125 MPa after 28 days of moist curing to make it more sustainable, environmentally friendly, and cost-efficient compared to UHP-FRC. After conducting a series of experiments, it was found that up to 50% of Portland cement in UHP-FRC mixes can be replaced by 25% fly ash (FA) class F and 25% ground granulated blast-furnace slag (GGBFS), both of which are industrial by-products, without compromising its maximum recorded compressive strength. Compressive strengths beyond 125 and 140 MPa were achieved for G-UHP-FRC mixtures after 28 and 56 days, respectively. Furthermore, the compressive strength of G-UHP-FRC was measured over an extended period of about two years according to which an ever-increasing strength with the highest

recorded value of about 170 MPa was recorded for G-UHP-FRC of this research. Based on these results, G-UHP-FRC achieves about 83% of its highest recorded compressive strength after 56 days. Therefore, the 56-day compressive strength of G-UHP-FRC could be considered for structural design purposes, instead of the 28-day compressive strength that is usually used for conventional concrete. In addition, the effects of fiber hybridization on both the compressive as well as tensile properties of G-UHP-FRC were investigated. High tensile strength (9.58 MPa) and high ductility (0.33% strain at peak tensile strength) were achieved for G-UHP-FRC based on a large-scale dogbone-shaped tension specimen (without embedded rebar) tested under uniaxial tensile forces. It was found that fiber hybridization, by using a combination of 3–4 different types of fibers (with a total amount of 2.5–3.0% by volume of concrete) does improve the tensile strength and ductility by about 15% and 95% compared to UHP-FRC of the prior research [11]. This was achieved by using a total fiber volume fraction of 2.5% (1.5% hooked-end, 0.5% long micro, and 0.5% short micro steel fibers), which is also slightly less than 3.0% of the prior research [11].

Furthermore, research to date on UHP-FRC composites has mainly been limited to experiments based on small-scale batches and specimens. The tensile behavior of UHP-FRC when reinforced with steel rebars though was very briefly investigated in the prior research [11], was in no wise comprehensive, and except very few and limited experiments by other researchers [31–33], cannot be found in the literature. Caution was raised by a few researchers about premature failure of high-performance concrete composites when reinforced according to design requirements and provisions of conventional reinforced concrete. Therefore, an extensive study of the tension-stiffening effect of the newly developed G-UHP-FRC was carried out in this research to investigate the tensile properties of reinforced UHP-FRC and G-UHP-FRC composites for structural design purposes and to provide structural design provisions and recommendations to avoid any probable premature fracture or failure when UHP-FRC and G-UHP-FRC composites are used in structural elements with steel rebars. A total of eleven large-scale dogbone-shaped tension-stiffening specimens with different steel rebar types and sizes were tested under uniaxial tension all the way to fracture of the embedded steel rebar. Based on the results of these experiments, yielding, hardening, and cracking mechanisms in reinforced G-UHP-FRC were better understood, and it was found that when A706 Grade 60 mild steel reinforcing bars are used to reinforce G-UHP-FRC tension members, if the longitudinal reinforcing ratio is below about 4.0%, a premature fracture of the steel reinforcement can lead to an overall brittle failure. However, if a minimum longitudinal reinforcing ratio of 4.0% is provided in G-UHP-FRC, the rebar can take greater loads after the first peak tensile load, leading to the formation of multiple transverse macro cracks and longitudinal splitting cracks, which in turn allows for distribution of plasticity over a longer distance along the rebar, and therefore, an overall ductile behavior is achieved. Furthermore, because other steel rebar types, such as stainless steel rebars are used in the industry for special applications, especially when high-performance concrete composites are used, a few tests were conducted using stainless steel. Accordingly, it was found that a minimum reinforcing ratio of about 3.0% of A276 Grade 75 stainless steel rebar could also be used as an alternative to obtain an overall ductile behavior for reinforced G-UHP-FRC tension members. It was further shown that reinforced G-UHP-FRC tension specimens with longitudinal reinforcing ratios less than 4% and 3% when A706 Grade 60 mild and A276 Grade 75 stainless steel are used, respectively, lead to a more brittle failure that is attributed to strain localization immediately after rebar yielding, early strain-hardening of the rebar at the cracked region, and finally, early fracture of the reinforcing bar at the location of one transverse macro crack. It was also concluded that for structural applications, developing G-UHP-

FRC composites with tensile strain capacities exceeding the yield strain of conventional steel rebars (i.e. 0.2–0.4%) may not in itself prevent brittle failure.

It was further shown that in order to observe an overall ductile behavior in reinforced G-UHP-FRC tension specimens, their first peak load should be smaller than the ultimate peak tensile load of their corresponding embedded bare steel rebar. It was further noted that increasing the longitudinal steel reinforcing ratio in tension-stiffening specimens (thus increasing the ultimate peak tensile load that can be taken by the embedded steel rebar) results in a higher first peak load for the tension-stiffening specimen as well. Thus, a ductile performance is not guaranteed only by increasing the longitudinal reinforcing ratio of the tension-stiffening specimens. Based on these observations, an equation was provided to estimate the minimum required longitudinal reinforcing ratio in reinforced G-UHP-FRC tension specimens to achieve a ductile behavior. This equation suggests that the ratio of peak to yield tensile strength is of great importance to achieve a ductile behavior, and the higher this ratio, the lower will be the minimum required longitudinal reinforcing ratio. In addition, the higher the tensile strength of the G-UHP-FRC or UHP-FRC composite, the higher will be the minimum required longitudinal reinforcing ratio.

In addition, a corrected tensile response was calculated for plain G-UHP-FRC of this research based on the response of the G-UHP-FRC tension-stiffening specimen reinforced with a No. 7 A706 Grade 60 mild steel rebar as well as the tensile response of its bare steel rebar. By comparing the corrected tensile response with that of an unreinforced G-UHP-FRC specimen, while a similar initial stiffness, strain-hardening, and peak strength were noted for both responses, an improved post-peak softening branch with a shallower slope was observed for the corrected response. This post-peak response improvement is due to reinforcing steel bar. By using Digital Image Correlation (DIC) techniques in tension-stiffening experiments, surface strain and concrete and bond stresses can be estimated from which the composite behavior of G-UHP-FRC or UHP-FRC mixtures with steel reinforcing bars could be better understood.

Because of the need to reduce the embodied and operational energy of the buildings, the application of UHP-FRC and G-UHP-FRC composites developed in this research was investigated to design a lightweight concrete metamaterial by engineering the void structure in concrete, implementing the familiar octet-truss lattices. In this research, UHP-FRC and G-UHP-FRC octet lattices were manufactured by infiltrating such concrete composites into 3D-printed octet lattice molds. These concrete octet lattices were called Octet-Truss Engineered Concrete (OTEC). The greater efficiency of the G-UHP-FRC and UHP-FRC OTEC unit cells (with 8, 10, and 11 mm-diameter elements resulting in 66.4, 53.6, and 47.5% porosity, respectively), in regard to peak strength, strain at peak, and toughness under uniaxial compression was verified compared to that of foam Green Ultra-High Performance Concrete (G-UHPC) cubes (45.3% porosity) with a geometrically disordered pore structure. A considerable increase in compressive strength and flexural capacity as well as higher stiffness and toughness was achieved for OTEC specimens cured in a fog room with more than 95% relative humidity at room temperature.

It was also found that octet lattice cells with higher porosity, and thus more slender elements, are much closer to the ideal stretching-dominated behavior compared to specimens with lower porosities. Because of the need for confirming the reproducibility of the results obtained for OTECs with other materials as well as creating confidence in the normalized results recorded for the UHP-FRC OTEC unit cells, the normalized performance of polylactic acid (PLA) octet lattice unit cells under compression was investigated, and it was found that very similar normalized

performances with increasing porosity are observed for both metamaterials, i.e. UHP-FRC OTEC and PLA octet lattice unit cells. Furthermore, the UHP-FRC OTEC unit cells were modeled in OpenSees. It was found that under pure axial compressive forces, even with a defect-free model for brittle materials, using pinned truss elements, it is not possible to reach the ideal linear strength-density relationship associated with pure stretching-dominated behavior. However, using beam-column elements in the model, allows for the development of bending moments in the elements, which results in a behavior due to both stretching and bending. The stretching effect, however, is more prominent as the elements become more slender as confirmed by both the OpenSees model, using beam-column elements, and experimental results for the 8 mm octet lattice cell with its most slender elements. In addition, a few tests under flexure were conducted, based on which G-UHP-FRC OTEC flexural beams achieved higher flexural toughness and ductility and comparable flexural strength as compared to that of solid conventional concrete with the same volume, only having a mass of about half of that of the solid conventional concrete beam. Such OTEC structures can be encased between skins to entrap air and potentially provide excellent thermal insulation for lightweight façade and flooring systems. Furthermore, the flexural performance of PLA octet-lattice reinforced Ultra-High Performance Concrete (UHPC) with three different UHPC volume fractions (37.5, 75, and 100%) was briefly investigated, based on which a stiffer and more ductile flexural response was observed for PLA octet-lattice reinforced UHPC with 37.5% and 75% infiltrations compared to plain PLA octet-lattices, however, at the expense of the peak flexural strength and toughness. The fully-infiltrated PLA octet-lattice (100% infiltration), however, reached higher stiffness and strength, but lower ductility compared to plain PLA octet-lattices.

Research on UHP-FRC and G-UHP-FRC composites could be extended to fully examine their behavior for different structural as well as non-structural applications in buildings, bridges, tunnels, and other infrastructure. Excellent properties of G-UHP-FRC offer enormous advantages as a modern construction material to build new infrastructure that is sustainable, durable, cost-efficient, earthquake-proof, and long-lasting so vital to a more systematic and sustainable development approach. Its adoption, however, has been slow in North America and suffers, on the one hand, from logistical and economic issues, and on the other, lack of sufficient expertise and multidisciplinary knowledge. Pushing the frontiers of science and technology in this field is, therefore, necessary and frankly inevitable. The following few avenues, if pursued by researchers in this field in near future, seem to lead to a new era for the immediate use of UHP-FRC and G-UHP-FRC composites in practice:

1: Development of structural design models and recommendations for UHP-FRC and G-UHP-FRC composites

As mentioned earlier, using high volumes of Portland cement in UHP-FRC composites leads to high carbon dioxide emissions, which is of major concern regarding global warming. Therefore, employing more sustainable approaches and techniques in the development of G-UHP-FRC composites is essential and need further investigation. In addition, to date, only a few large-scale structural testing of UHP-FRC reinforced with steel reinforcing bars have been performed. Hence, the synergy between the structural steel reinforcement and UHP-FRC composites is not well known, especially for structural elements loaded up to large deformations. This crucial information is not only essential to engineers for design purposes but is more importantly necessary to avoid any unexpected failure when used in structures. Therefore, a comprehensive study of the effects of steel reinforcement as well as other novel reinforcing materials in UHP-FRC and G-UHP-FRC

composites is needed by building upon the results presented in this research to develop and suggest models as well as design recommendations for ease of use by engineers in the field and industry.

2: Accelerated Bridge Construction (ABC) using UHP-FRC and G-UHP-FRC composites

Federal Highway Administration (FHWA) and Caltrans have shown great interest in utilizing UHP-FRC composites for Accelerated Bridge Construction (ABC). This is because UHP-FRC composites are mostly impermeable and therefore, very durable and when reinforced with mild steel rebars, are also corrosion resistant. They are four to five times stronger than conventional concrete and thus can provide the required strength and stiffness with smaller element dimensions and less materials. Improved tensile strength and hardening of UHP-FRC composites provide crack resistance, post-cracking ductility, and post-peak load-carrying capacity, all of which are essential for better long-term structural performance in seismic regions, especially under aggressive environmental conditions. Therefore, it is further needed to develop precast manufacturing techniques for accelerated construction and testing of prefabricated bridge piers made of UHP-FRC and G-UHP-FRC under strong seismic forces to further advance the knowledge of their performance. Some preliminary results also indicate very promising potentials of using UHP-FRC composites for retrofitting bridge approach slabs, pavements, and columns. UHP-FRC and G-UHP-FRC composites are also highly ductile under compression. This property could, through innovative reinforcing methods, such as lattice-reinforcing techniques briefly studied in this research, be further enhanced for use in special structural elements such as supports for deep tunnels as well as highly compressive columns in moment frames of high-rise buildings.

3: Development and design of lightweight energy-efficient building systems from UHP-FRC and G-UHP-FRC composites, using 3-D printing techniques

In this research, it was shown that by taking advantage of ultra-high strength and great flowability of UHP-FRC and G-UHP-FRC composites, it is possible to engineer UHP-FRC truss lattices that can be used for lightweight systems, not only to improve their mechanical properties while using less materials, but also to enhance their cost and energy efficiency by providing better insulation and acoustic properties. Other functionalities should then be incorporated into such systems to improve inner building air quality, for example through breathable façades. Extending these preliminary experiments and results in designing and manufacturing such systems for use in practice seems to be contingent upon integrating direct additive manufacturing techniques for 3D-printing UHP-FRC and G-UHP-FRC with current developments for more sophisticated and effective architectural and functional designs of building systems. Concrete negative mold 3D-printing, as implemented in this research for manufacturing OTECs through infiltration, though currently seems impractical due to its scaling limitations and slowness, is promising and believed to be beneficial for certain applications in practice.

Bibliography

[1] Aghdasi P, Ostertag CP. Green ultra-high performance fiber-reinforced concrete (G-UHP-FRC). Constr Build Mater 2018;190:246–54. doi:10.1016/J.CONBUILDMAT.2018.09.111.

[2] Aghdasi P, Williams ID, Salazar B, Panditi N, Taylor HK, Ostertag CP. An Octet-Truss Engineered Concrete (OTEC) for lightweight structures. Compos Struct 2019;207:373–84. doi:10.1016/J.COMPSTRUCT.2018.09.011.

[3] Yudenfreund M, Skalny J, Mikhail RS, Brunauer S. Hardened portland cement pastes of low porosity II. Exploratory studies. Dimensional changes. Cem Concr Res 1972;2:331–48. doi:10.1016/0008-8846(72)90074-9.

[4] Yudenfreund M, Odler I, Brunauer S. Hardened portland cement pastes of low porosity I. Materials and experimental methods. Cem Concr Res 1972;2:313–30. doi:10.1016/0008-8846(72)90073-7.

[5] Roy DM, Gouda GR, Bobrowsky A. Very high strength cement pastes prepared by hot pressing and other high pressure techniques. Cem Concr Res 1972;2:349–66. doi:10.1016/0008-8846(72)90075-0.

[6] de Larrard F, Sedran T. Optimization of ultra-high-performance concrete by the use of a packing model. Cem Concr Res 1994;24:997–1009. doi:10.1016/0008-8846(94)90022-1.

[7] Richard P, Cheyrezy M. Composition of reactive powder concretes. Cem Concr Res 1995;25:1501–11. doi:10.1016/0008-8846(95)00144-2.

[8] Naaman A, Wille K. Some correlation between high packing density, ultra-high performance, flow ability, and fiber reinforcement of a concrete matrix. BAC2010—2nd Iber Congr Self Compact 2010.

[9] Wille K, Naman AE, Parra-Montesinos GJ. Ultra - High Performance Concrete with Compressive Strength Exceeding 150 MPa (22ksi) : A Simpler Way. ACI Mater J 2011;108:46–53. doi:10.14359/51664215.

[10] Wille K, Naaman AE, El-Tawil S, Parra-Montesinos GJ. Ultra-high performance concrete and fiber reinforced concrete: achieving strength and ductility without heat curing. Mater Struct 2012;45:309–24. doi:10.1617/s11527-011-9767-0.

[11] Aghdasi P, Heid AE, Chao SH. Developing ultra-high-performance fiber-reinforced concrete for large-scale structural applications. ACI Mater J 2016;113:559–69. doi:10.14359/51689103.

[12] ASTM. Standard test methods for uncompacted void content of fine aggregate (as influenced by particle shape, surface texture, and grading). C1252-06 2006.

[13] ASTM C1437-07, Standard Test Method for Flow of Hydraulic Cement Mortar. West

Conshohocken, PA: ASTM International; 2007.
[14] ASTM C109/C109M-11a, Standard Test Method for Compressive Strength of Hydraulic Cement Mortars (Using 2-in. or [50-mm] Cube Specimens). West Conshohocken, PA: ASTM International; 2016.
[15] De Larrard F. Concrete mixture proportioning: a scientific approach. CRC Press; 2014.
[16] Markovic I. High-performance hybrid-fibre concrete: development and utilisation 2006.
[17] Sun W, Yan H, Zhan B. Analysis of mechanism on water-reducing effect of fine ground slag, high-calcium fly ash, and low-calcium fly ash. Cem Concr Res 2003;33:1119–25. doi:10.1016/S0008-8846(03)00022-X.
[18] Yahia A, Tanimura M, Shimoyama Y. Rheological properties of highly flowable mortar containing limestone filler-effect of powder content and W/C ratio. Cem Concr Res 2005;35:532–9. doi:10.1016/J.CEMCONRES.2004.05.008.
[19] Mehta P, Monteiro PJM. Concrete: Microstructure, Properties, and Materials. McGraw-Hill Education; 2006.
[20] Davis BG and M. Cylinder or Cube: Strength Testing of 80 to 200 MPa (11.6 to 29 ksi) Ultra-High-Performance Fiber-Reinforced Concrete. Mater J n.d.;105. doi:10.14359/20202.
[21] Wille K, Naaman AE, El-Tawil S. Optimizing ultra-high performance fiber-reinforced concrete. Concr Int 2011;33:35–41.
[22] Ranade R, Li VC, Stults MD, Heard WF, Rushing TS. Composite Properties of High-Strength, High-Ductility Concrete. ACI Mater J 2013;110.
[23] Kwon S, Nishiwaki T, Kikuta T, Mihashi H. Development of Ultra-High-Performance Hybrid Fiber-Reinforced Cement-Based Composites. ACI Mater J 2014;111.
[24] Park SH, Kim DJ, Ryu GS, Koh KT. Tensile behavior of Ultra High Performance Hybrid Fiber Reinforced Concrete. Cem Concr Compos 2012;34:172–84. doi:10.1016/J.CEMCONCOMP.2011.09.009.
[25] Palacios G. Performance of full-scale ultra-high performance fiber-reinforced concrete column subjected to extreme earthquake-type loading and effect of surface preparation on the cohesion and friction factors of the aashto interface shear equation. The University OF Texas at Arlington; 2015.
[26] Ashby MF. The properties of foams and lattices. Philos Trans A Math Phys Eng Sci 2006;364:15–30. doi:10.1098/rsta.2005.1678.
[27] Zheng X, Lee H, Weisgraber TH, Shusteff M, DeOtte J, Duoss EB, et al. Ultralight, Ultrastiff Mechanical Metamaterials. Science (80-) 2014;344:1373–7. doi:10.1126/science.1252291.
[28] Chao S-H, Liao W-C, Wongtanakitcharoen T, Naaman AE. Large scale tensile tests of high performance fiber reinforced cement composites. Proc., 5th Int. RILEM Work. High Perform. Fiber Reinf. Cem. Compos., 2007.
[29] Moreno DM, Trono W, Jen G, Ostertag C, Billington SL. Tension stiffening in reinforced high performance fiber reinforced cement-based composites. Cem Concr Compos 2014;50:36–46. doi:10.1016/j.cemconcomp.2014.03.004.
[30] Kang S-B, Tan KH, Zhou X-H, Yang B. Influence of reinforcement ratio on tension stiffening of reinforced engineered cementitious composites. Eng Struct 2017;141:251–62. doi:10.1016/J.ENGSTRUCT.2017.03.029.
[31] Hollmann CP. Tensile Behavior of Ultra-High Performance Fiber Reinforced Concrete and Reinforcement Bar 2014.

[32] Jungwirth J, Muttoni A. Structural Behavior of Tension Members in UHPC. École Polytechnique Fédérale de Lausanne, IS-Beton 2004.
[33] Redaelli D. Testing of reinforced high performance fibre concrete members in tension. Proc. 6th Int. Ph. D. Symp. Civ. Eng. Zurich 2006, Proceedings of the 6th Int. Ph. D. Symposium in Civil Engineering, Zurich 2006; 2006, p. 8.
[34] Graybeal B. Flexural Behavior of an Ultrahigh-Performance Concrete I-Girder. J Bridg Eng 2008;13:602–10. doi:10.1061/(ASCE)1084-0702(2008)13:6(602).
[35] Graybeal B. Ultra-High Performance Concrete. Res Dev Technol Turner-Fairbank Highw Res Center 2011;FHWA Publi:8.
[36] Resplendino J, Toutlemonde F. The UHPFRC revolution in structural design and construction. RILEM-fib-AFGC Int. Symp. Ultra-High Perform. Fibre-Reinforced Concr. UHPFRC 2013, vol. October 1-, Marseille, France: 2013, p. 791–804.
[37] Aghdasi P, Palacios G, Heid AE, Chao SH. Mechanical properties of a highly flowable ultra-high-performance fiber-reinforced concrete mixture considering large-size effects. Proc High Perform Fiber Reinf Cem Compos (HPFRCC 7) 2015.
[38] Aghdasi P. Development of ultra-high performance fiber-reinforced concrete (UHP-FRC) for large-scale casting 2015.
[39] Test CC, Drilled T, Concrete C. Standard Test Method for Flexural Strength of Concrete (Using Simple Beam with Third-Point Loading) 1. vol. C78-02. ASTM International; 2010. doi:10.1520/C0078.
[40] Dudziak L, Mechtcherine V. Mitigation of volume changes of ultra-high performance concrete (UHPC) by using super absorbent polymers. 2nd Int. Symp. Ultra High Perform. Concr., Kassel: 2008.
[41] Blunt JD, Ostertag CP. Deflection Hardening and Workability of Hybrid Fiber Composites. ACI Mater J 2009;106:265–72.
[42] Videla CC, Carreira DJ, Garner NJ. Guide for modeling and calculating shrinkage and creep in hardened concrete. ACI Rep 2008;209.
[43] Sung D. A New Look at Building Facades as Infrastructure. Engineering 2016;2:63–8.
[44] Melo JP, Aguilar AS, Olivares francisco H. Cement Paste Foamed by the Addition of Aluminum Powder with Metakaolin and Sepiolite. Constr. Build. Res., 2014, p. 443–51. doi:10.1007/978-94-007-7790-3_54.
[45] Ramamurthy K, Kunhanandan Nambiar EK, Indu Siva Ranjani G. A classification of studies on properties of foam concrete. Cem Concr Compos 2009;31:388–96. doi:10.1016/j.cemconcomp.2009.04.006.
[46] Tonyan TD, Gibson LJ. Strengthening of cement foams. J Mater Sci 1992;27:6379–86. doi:10.1007/BF00576288.
[47] Nambiar EKK, Ramamurthy K. Models for strength prediction of foam concrete. Mater Struct 2008;41:247–54. doi:10.1617/s11527-007-9234-0.
[48] Deshpande VS, Ashby MF, Fleck NA. Foam topology: bending versus stretching dominated architectures. Acta Mater 2001;49:1035–40. doi:10.1016/S1359-6454(00)00379-7.
[49] Deshpande VS, Fleck NA, Ashby MF. Effective properties of the octet-truss lattice material. J Mech Phys Solids 2001;49:1747–69. doi:10.1016/S0022-5096(01)00010-2.
[50] Bauer J, Hengsbach S, Tesari I, Schwaiger R, Kraft O. High-strength cellular ceramic composites with 3D microarchitecture. Proc Natl Acad Sci U S A 2014;111:2453–8. doi:10.1073/pnas.1315147111.

[51] Bückmann T, Stenger N, Kadic M, Kaschke J, Frölich A, Kennerknecht T, et al. Tailored 3D mechanical metamaterials made by dip-in direct-laser-writing optical lithography. Adv Mater 2012;24:2710–4. doi:10.1002/adma.201200584.
[52] McKenna F, Fenves G, Scott M, Jeremic B. Open system for earthquake engineering simulation (OpenSees) 2000.
[53] Ashby M. Materials Selection in Mechanical Design. 3rd ed. Butterworth-Heinemann; 2005.
[54] Graybeal BA. Structural Behavior of Ultra High Performance Concrete Prestressed I-Girders 2006.
[55] Carreira DJ, Chu KH. Stress-strain Relationship for Reinforced Concrete in Tension. Am Soc Civ Eng 1986;83:21–8. doi:10.1017/CBO9781107415324.004.
[56] Goto Y. Cracks formed in concrete around deformed tension bars. J. Proc., vol. 68, 1971, p. 244–51.
[57] Moehle JP. Seismic design of reinforced concrete buildings. McGraw-Hill Education New York; 2015.
[58] Chao S-H. Bond characterization of reinforcing bars and prestressing strands in high performance fiber reinforced cementitious composites under monotonic and cyclic loading. 2005.
[59] Li GF and VC. Influence of Matrix Ductility on Tension-Stiffening Behavior of Steel Reinforced Engineered Cementitious Composites (ECC). Struct J n.d.;99. doi:10.14359/11041.
[60] Yoo D-Y, Shin H-O, Yang J-M, Yoon Y-S. Material and bond properties of ultra high performance fiber reinforced concrete with micro steel fibers. Compos Part B Eng 2014;58:122–33. doi:10.1016/J.COMPOSITESB.2013.10.081.